TU/e EINDHOVEN UNIVERSITY OF TECHNOLOGY

Expanding thermal plasma deposition of microcrystalline silicon for solar cells

Citation for published version (APA):
Smit, C. (2005). *Expanding thermal plasma deposition of microcrystalline silicon for solar cells*. [Phd Thesis 1 (Research TU/e / Graduation TU/e), Applied Physics and Science Education]. Technische Universiteit Eindhoven. https://doi.org/10.6100/IR584433

DOI:
10.6100/IR584433

Document status and date:
Published: 01/01/2005

Document Version:
Publisher's PDF, also known as Version of Record (includes final page, issue and volume numbers)

Please check the document version of this publication:

• A submitted manuscript is the version of the article upon submission and before peer-review. There can be important differences between the submitted version and the official published version of record. People interested in the research are advised to contact the author for the final version of the publication, or visit the DOI to the publisher's website.
• The final author version and the galley proof are versions of the publication after peer review.
• The final published version features the final layout of the paper including the volume, issue and page numbers.

Link to publication

General rights
Copyright and moral rights for the publications made accessible in the public portal are retained by the authors and/or other copyright owners and it is a condition of accessing publications that users recognise and abide by the legal requirements associated with these rights.

• Users may download and print one copy of any publication from the public portal for the purpose of private study or research.
• You may not further distribute the material or use it for any profit-making activity or commercial gain
• You may freely distribute the URL identifying the publication in the public portal.

If the publication is distributed under the terms of Article 25fa of the Dutch Copyright Act, indicated by the "Taverne" license above, please follow below link for the End User Agreement:

www.tue.nl/taverne

Take down policy
If you believe that this document breaches copyright please contact us at:

openaccess@tue.nl

providing details and we will investigate your claim.

Download date: 16. Nov. 2023

EXPANDING THERMAL PLASMA DEPOSITION OF MICROCRYSTALLINE SILICON FOR SOLAR CELLS

CHIEL SMIT

Expanding Thermal Plasma Deposition of Microcrystalline Silicon for Solar Cells

PROEFSCHRIFT

ter verkrijging van de graad van doctor aan de
Technische Universiteit Eindhoven, op gezag van
de Rector Magnificus, prof.dr. R.A. van Santen, voor
een commissie aangewezen door het College voor
Promoties in het openbaar te verdedigen op
vrijdag 4 maart 2005 om 16.00 uur

door

Chiel Smit

geboren te Vlissingen

Dit proefschrift is goedgekeurd door de promotoren:

prof.dr.ir. M.C.M. van de Sanden
en
prof.dr. C.I.M. Beenakker

Copromotor:
dr. R.A.C.M.M. van Swaaij

Printed and bounded by Universiteitsdrukkerij Technische Universiteit Eindhoven

Cover: high-resolution transmission electron microscope image of microcrystalline silicon that is deposited with expanding thermal plasma enhanced chemical vapour deposition

Cover design: Mark de Graaf and Patrick Meijers

CIP-DATA LIBRARY TECHNISCHE UNIVERSITEIT EINDHOVEN

Smit, Chiel

Expanding thermal plasma deposition of microcrystalline silicon for solar cells / door Chiel Smit. – Eindhoven : Technische Universiteit Eindhoven, 2005. –
Proefschrift.
ISBN 90-386-2121-3
NUR 926
Trefw.: plasmadepositie / plasmafysica / silicium / dunnelaaghalfgeleiders / zonnecellen
Subject headings: plasma CVD / expanding thermal plasma / microcrystalline silicon / solar cells

Contents

Chapter 1. Introduction **1**

Chapter 2. Experimental set-up **7**

1. The CASCADE deposition system 7
2. Plasma analysis 9
   2.1. Mass spectrometry 9
   2.2. Electron beam induced fluorescence (EBIF) 10
3. Thin film analysis techniques 10
   3.1. The samples 10
   3.2. Reflection-transmission spectroscopy 11
   3.3. Photoconductivity 12
   3.4. Activation energy and dark conductivity 12
   3.5. Fourier-transform infrared absorption (FTIR) 13
   3.6. Raman spectroscopy 14
   3.7. X-ray analysis (XRD, SAXS) 14
   3.8. Electron microscopy 15
4. Solar cell layout and analysis 17
   4.1. Preparation 17
   4.2. Analysis 17

References 18

Chapter 3. Electron beam induced fluorescence measurements of the degree of hydrogen dissociation in hydrogen plasmas **19**

1. Introduction 20
2. Theory 21
   2.1. The principle of electron beam induced fluorescence 21
   2.2. The optical thickness of the plasma: re-absorption correction 24
3. Experiment 25
   3.1. The plasma 25
   3.2. The EBIF set-up 26
   3.3. The plasma and gas temperatures 27
   3.4. Measurements 28
   3.5. Applicability and detection limit 28
4. Results and discussion 30
5. Conclusions 31

Acknowledgements 32

Appendix A. Vector and matrix definitions 32

Appendix B. Numerical values of the decay rates and excitation cross-sections 33

Appendix C. The degree of dissociation 35

Appendix D. Re-absorption correction 37

References 38

Chapter 4. Determining the material structure of microcrystalline silicon from Raman spectra **39**

1. Introduction 40
2. The Raman spectrum of microcrystalline silicon 41
   2.1. The Raman spectrum 41
   2.2. Ways to get the material structure from Raman spectroscopy 42
3. Experiment 44
4. Results and discussion 45
   4.1. Splitting a Raman spectrum into a crystalline and an amorphous contribution 45
   4.2. Raman spectrum of the crystalline fraction 46
   4.3. Determining the crystalline fraction 47
   4.4. Comparison with other techniques 49
   4.5. Conclusion 51

Acknowledgements 51
References 52

Chapter 5. Minimizing the incubation layer thickness of microcrystalline silicon films by adjusting the processing pressure to the electrode separation in RF PECVD **55**

1. Introduction 56
2. Experiment 57
3. Results and discussion 59
   3.1. Electrode separation 59
   3.2. Bias voltage versus electrode separation 61
   3.3. Induction time versus thickness of the incubation layer 63
   3.4. Application in solar cells 64
4. Conclusions 66

Acknowledgements 66
References 66

Chapter 6. High-rate deposition of microcrystalline silicon with an expanding thermal plasma **69**

1. Introduction 70
2. Experiment 70
   2.1. The experimental set-up 70
   2.2. Film analysis 72
   2.3. Solar cell preparation and analysis 73
3. Results and discussion 74
   3.1. Varying the deposition parameters 74
   3.2. The material properties 79
   3.3. Comparison of μc-Si:H deposited with ETP and with other techniques 85
   3.4. Solar cells 86
4. Conclusions 89

Acknowledgements 90

References 90

Chapter 7. The role of the silyl radical in plasma deposition of microcrystalline silicon 93

1. Introduction 94
2. Experimental set-up and procedures 96
3. Results and discussion 99
   3.1. SiH_4 variation 99
   3.2. Ring position variation 101
4. Conclusions 105

Acknowledgements 105
References 105

Summary 109

Samenvatting 111

List of publications related to this work 113

Dankwoord 115

Curriculum vitae 117

Chapter 1

Introduction

At the time, the contribution of solar energy to the world's energy consumption is negligible. This is mainly a matter of cost effectiveness: the production of solar cells is just too expensive. The commercially dominant type of solar cell is the mono-crystalline or *c*-Si type cell. The production process is well known and the produced cells are stable and have high-energy conversion efficiencies (typically 20%). A disadvantage of this technology is that the production is so expensive that it cannot compete as an energy source with conventional sources. A practical disadvantage concerns the form factor: *c*-Si cells have a limited diameter, are flat and rigid. This puts limits on the applicability: large surfaces are more elaborate to produce and integration with flexible or curved surfaces is impossible.

Important alternatives to *c*-Si solar cells are based on thin silicon films. Thin silicon films overcome the main drawbacks of *c*-Si: they can be prepared at lower cost, they are in principle flexible, and their production process (plasma deposition) can be scaled up much easier than the size of crystalline silicon wafers, even to sizes of about 1 m^2 or more. An aspect that is not important in existing applications, but can become essential in the future is the freedom in form factor: thin layers can be deposited on flexible and curved surfaces, allowing much more freedom in use. It is for these perspectives that much effort is put in the research on thin film silicon layers.

The history of thin film silicon starts with the development of hydrogenated amorphous silicon (*a*-Si:H) by Sterling and Swann [1] and by Chittick et al. [2]. They were the first to deposit *a*-Si:H from a silane (SiH_4) radio frequent glow discharge.

With the discovery that *a*-Si:H can be doped and the further development of doped *a*-Si:H films by Spear and LeComber [3] electronic devices prepared from thin silicon films came within reach. Carlson and Wronski are the first to report *a*-Si:H solar cells in 1976 [4]. The electronic properties of pure amorphous silicon (*a*-Si), however, are inferior to those of mono-crystalline silicon. In contrast to *c*-Si, where the atoms are ordered in a periodic lattice, in *a*-Si the atoms are more randomly ordered, with a distribution of bonding angles and bonding lengths. Strained atomic bonds and dangling electronic bonds act as traps for electrons and holes, affecting the electronic properties negatively for device applications. These traps can be partly neutralised by the addition of hydrogen in the material, making *a*-Si:H. Still the electronic properties are inferior to those of *c*-Si. Furthermore, *a*-Si:H is subject to degradation under illumination (Staebler-Wronski effect [5]). In solar-cell technology, this implicates a strongly hindered transport of the charge carriers to the contacts of the solar cell and the regular n-p diode-type solar cell architecture does not suffice any more. Therefore, in thin film silicon solar cell technology a negatively doped (n) and a positively doped (p) layer sandwich an intrinsic (i) layer in which most of the sunlight is absorbed. This way an electrical field is created in the i-layer that enhances the transport of the charge carriers.

A material that combines the good electronic properties of *c*-Si with the advantage of low temperature thin-film processing would be very attractive. In 1968, Vepřek and Mareček reported the preparation of another type of thin silicon film: hydrogenated microcrystalline silicon (μc-Si:H) [6]. They used a hydrogen plasma transport technique. In 1979, Usui and Kikuchi demonstrated that μc-Si:H could also be prepared using radio-frequent plasma enhanced chemical vapour deposition (RF PECVD) [7], but it took until the early 90s for the first preparation of μc-Si:H solar cells (e.g. [8], [9]). This material consists of a mixture of crystalline and amorphous phase and grain boundaries between adjacent crystallites. It can be prepared by applying relatively cheap, low temperature deposition technology, similar to *a*-Si:H. At the same time, if the crystalline fraction is large enough, the electronic properties are dominated by the crystalline phase in the material [10]. Therefore, charge carrier transport properties are considerably better than those of *a*-Si:H. Furthermore, μc-Si:H hardly suffers from light induced degradation. Due to the large amount of grain boundaries, however, the electronic properties are still inferior to those of mono-crystalline silicon. In solar cell technology, for example, this results in lower energy conversion efficiencies.

The consequence of lower energy conversion efficiency is lower cost effectiveness. There are two ways to overcome this drawback. The first one is to increase the conversion efficiency of thin film solar cells. Several approaches are explored: (i) improvement of the electronic quality of the films, (ii) implementing light-trapping techniques by improvement of the back reflector or by applying texturing of the transparent conducting window layer. These improvements allow further reduction of the layer thickness and consequently lower electrical transport losses. A promising concept to improve efficiency is the so-called micromorph tandem cell [11], which consists of an *a*-Si:H top cell and a μc-Si:H bottom cell. The top cell absorbs the blue part of the solar spectrum, whereas the bottom cell absorbs the red

part of the spectrum. The combination of the two cells makes more efficient use of the solar spectrum, thereby increasing the overall energy conversion efficiency.

The second approach to a better cost-effectiveness is to decrease the production costs enough in order to obtain a technology that can commercially compete with existing energy sources. In order to decrease production costs the growth rate of the silicon films should be increased. Especially microcrystalline films should be prepared at elevated growth rates, because these films should be 1-3 μm thick when applied in solar cells. Conventional RF PECVD gives growth rates of about 0.2 nm/s, although recently rates up to 2.5 nm/s have been obtained for high-pressure process conditions [12] and solar cells with conversion efficiencies of about 8% and 6.6% have been prepared at growth rates of 0.5 nm/s and 1 nm/s respectively [13]. Several other techniques have been used to obtain high growth rates. Very High Frequency (VHF) PECVD (reported solar cell efficiency of 7.8% at 0.74 nm/s [14]), Hot Wire (HW) CVD (4.4% at 0.5 nm/s [15]), and Electron Cyclotron Resonance (ECR) CVD [16,17] are some examples. Expanding thermal plasma enhanced chemical vapour deposition (ETP CVD) has been used for the preparation of *a*-Si:H films in solar cells with a deposition rates of 0.8 nm/s and 1.4 nm/s resulting in energy conversion efficiencies of 6.7% and 5.4%, respectively [18]. This technique has turned out to be suitable for the fast deposition of a variety of other thin film materials, as well. Some examples are diamond-like carbon (DLC) [19,20] for protective coatings, zinc oxide for transparent conductive contacts, $SiO_xC_yH_z$ [21], and silicon nitride films as an anti-reflection and passivating coating of (multi) crystalline silicon solar cells [22].

Aim and outline of the thesis

The aim of the research described in this thesis is to investigate the potential of ETP CVD for the high-rate deposition of *μc*-Si:H films for application in solar cells. Therefore, first of all a laboratory set-up has been developed for the preparation of solar cells using ETP CVD. This set-up is shortly described in chapter 2 as well as the sample preparation and analysis techniques.

The atomic hydrogen density at the substrate surface is considered to be a crucial factor in the deposition process of *μc*-Si:H films. ETP CVD allows a wide range of operational parameter settings. In order to be able to explore this parameter space efficiently, a diagnostic tool was developed to measure the atomic hydrogen density in the plasma that expands towards the substrate. This tool, electron beam induced fluorescence (EBIF) is introduced in chapter 3. It is shown that EBIF is a relatively easy to apply experimental technique compared to other techniques for the detection of atomic hydrogen.

To determine the influence of the process parameters on the film quality a reliable set of film analysis techniques is necessary. Raman spectroscopy plays an important role in this field. However, in microcrystalline materials, finite size effects can influence the measured spectrum. Though this complicates the interpretation, it also provides extra information. Chapter 4 describes a new approach to derive the crystalline fraction and the average crystal size from a measured Raman spectrum of a *μc*-Si:H film.

For the preparation of fully *μc*-Si:H solar cells also doped *μc*-Si:H films are necessary. These doped films, especially the p-type films, which are used as a window

layer, should be very thin (typically 20 nm) to minimise light absorption since only light absorption in the intrinsic film results in effective conversion from light to electrical energy. The growth of μc-Si:H films starts with an amorphous incubation layer. This complicates the preparation of the very thin, doped films that are required in solar cells. This problem is addressed in chapter 5.

In chapter 6 the process parameters of ETP CVD are varied and the influence on the material quality is investigated. For optimised conditions a more extended characterisation of the deposited μc-Si:H films is carried out. Furthermore, in this chapter the results of the first solar cells with ETP CVD are presented.

In chapter 7 we discuss some aspects of the plasma chemistry that is involved in the deposition process of μc-Si:H. It is tried to relate the SiH_4 depletion, the sticking probability of the film-forming radicals, and the film density.

References

[1] H.F. Sterling and R.C.G. Swann, Solid State Electron. **8**, 653 (1965).

[2] R.C. Chittick, J.H. Alexander, and H.F. Sterling, J. Electrochem. Soc. **116**, 77 (1969).

[3] W. Spear and P. Lecomber, Solid State Comm. **17**, 1193 (1975).

[4] D.E. Carlson and C.R. Wronski, Appl. Phys. Lett. **28**, 671 (1976).

[5] D.L. Staebler and C.R. Wronski, Appl. Phys. Lett. **31**, 292 (1977).

[6] S. Vepřek and V. Mareček, Solid State Electr. **11**, 683 (1968).

[7] S. Usui and M. Kikuchi, J. Non-Cryst. Solids **34**, 1 (1979).

[8] M.J. Williams et al., AIP conf. Proc, **234**, 211 (1991).

[9] M. Faradji et al., Appl. Phys Lett. **60**, 3289 (1992).

[10] K. Shimakawa, J. Non-Cryst. Solids **266-**269, 223 (2000).

[11] J. Meier, S. Dubail, D. Fischer, J.A. Anna Selvan, N. Pellaton Vaucher, R. Platz, Ch. Hof, R. Flückiger, U. Kroll, N. Wyrsch, P. Torres, H. Keppner, A. Shah, and K.-D. Ufert, proc. of the 13th European Photovoltaic Solar Energy Conference, 1995.

[12] U. Graf, J. Meier, U. Kroll, J. Bailat, C. Droz, E. Vaillat-Sauvain, A. Shah, Thin Solid Films **427**, 37 (2003).

[13] T. Roschek, T. Repmann, J. Müller, B. Rech, and H. Wagner, Proc. of the 27th IEEE P.V. Spec. Conf., 2000, p. 150.

[14] L. Feitknecht, O. Kluth, Y. Ziegler, X. Niquille, P. Torres, J. Meier, N. Wyrsch, and A. Shah, Solar En. Mat. and solar cells **66**, 397 (2001).

[15] R.E.I. Schropp, Thin Solid Films **403-404**, 17 (2002).

[16] V.L. Dalal, S. Kaushal, E.X. Ping, J. Xu, R. Knox, and K. Han, Proc. of Mat. Res. Soc. **377**, 137 (1995).

[17] M. Mars, M. Fathallah, E. Tresso, and S. Ferrero, J. Non-Cryst. Sol. **299-302**, 133 (2002).

[18] B.A. Korevaar, C. Smit, A.M.H.N. Petit, R.A.C.M.M. van Swaaij, and M.C.M. van de Sanden, Mat. Res. Soc. Proc. 715, 595 (2002).

[19] J.W.A.M. Gielen, P.R.M. Kleuskens, M.C.M. van de Sanden, L.J. van IJzendoorn, D.C. Schram, E.H.A.Dekempeneer, J. Meneve, J.Appl. Phys. **80**, 5986 (1996).

[20] J. Benedikt, R.V. Woen, S.L.M. van Mensfoort, V. Perina, J. Hong, M.C.M. van de Sanden, Diamond and related materials **12**, 90 (2003).

[21] M. Creatore, M. Kilic, K. O'Brien, R. Groenen, M.C.M. van de Sanden, Thin Solid Films **427**, 137 (2003).

[22] W.M.M. Kessels, J. Hong, F.J.H. van Assche, J.D. Moschner, T. Lauinger, W.J. Soppe, A.W. Weeber, D.C. Schram, and M.C.M. van de Sanden, J. Vac. Sc. Techn. A **20**, 1704 (2002).

Chapter 2

Experimental set-up

1. The CASCADE deposition system

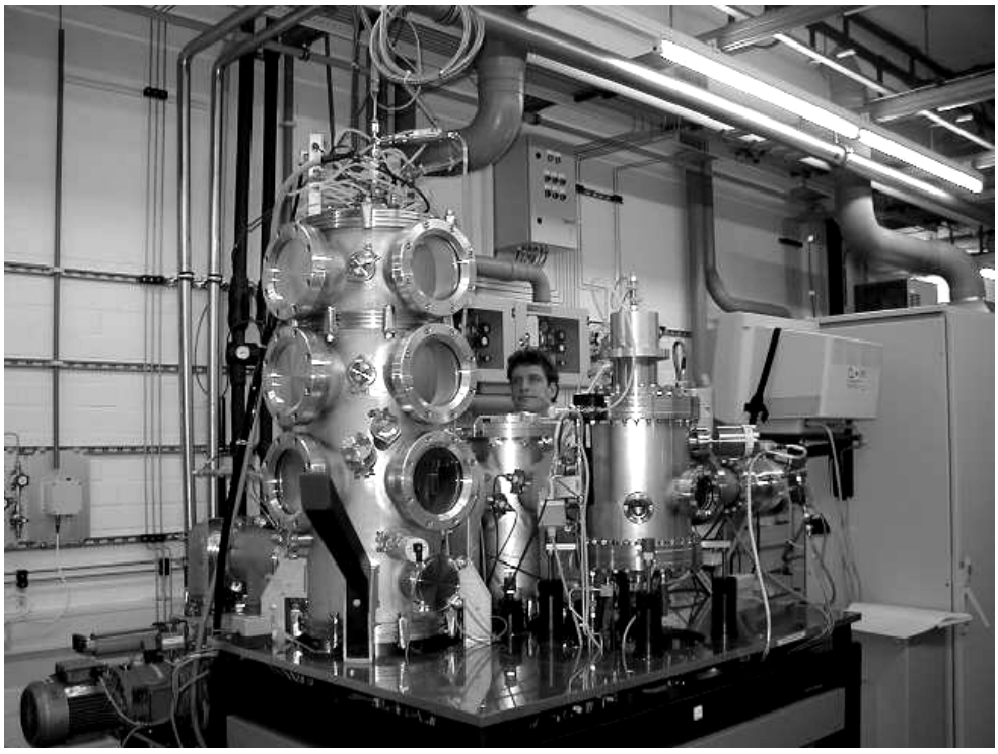

Figure 1. The CASCADE system.

To employ expanding thermal plasma enhanced chemical vapour deposition (ETP CVD) in the production of thin silicon films in solar cells a new deposition set-up has been build: the CASCADE (Cascaded Arc Solar Cell Apparatus Delft Eindhoven). A photograph of the set-up is shown in figure 1. The deposition system consists of a central load lock, from which samples can be transported into two reaction chambers, one for radio-frequent plasma enhanced chemical vapour deposition (RF PECVD) and one for ETP CVD. In the RF PECVD chamber a RF power supply (13.56 MHz) is connected to the lower, circular electrode, which is adjustable in height from the outside. The grounded upper electrode is the substrate holder, and can carry substrates up to 100 mm by 100 mm. The substrate is clamped onto a copper yoke, which can be heated up to 400°C. Thermal contact between the yoke and the substrate is improved by a helium flow of 50 sccm, which is switched off during deposition. The set temperature is reached within 10°C in about 15 minutes. During deposition the gas pressure is controlled by a butterfly valve, which in turn is controlled by a feed back loop with the pressure sensor. This chamber is pumped down by a turbo molecular pump backed by a mechanical fore line pump.

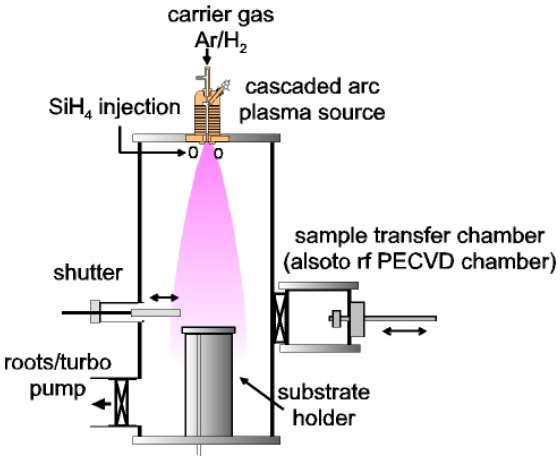

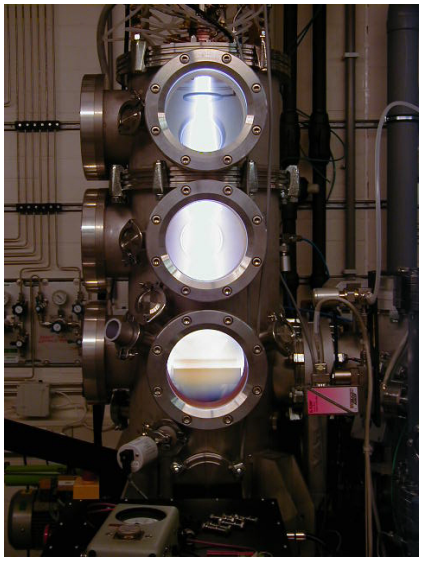

Figure 2. Schematic (left) and photograph (right) of the ETP chamber of the CASCADE system.

The ETP CVD chamber is shown in figure 2. The cascaded arc plasma source (figure 3) is placed on top. A separate gas inlet in the top flange of the reaction chamber is connected to the injection ring inside. At the bottom of the reaction chamber the substrate holder is mounted, which is a copy of the one in the RF PECVD chamber. The helium flow is 100-200 sccm and is maintained during deposition. Besides a turbo molecular pump (with a mechanical fore line pump) a roots blower (backed by a mechanical fore line pump, later replaced with a dry pump) is connected to pump the high process gas flows. A shutter shields the substrates from the expanding plasma during the start-up procedure. An infrared laser and a detector are mounted to enable interferometry during deposition in order to monitor the film thickness. At

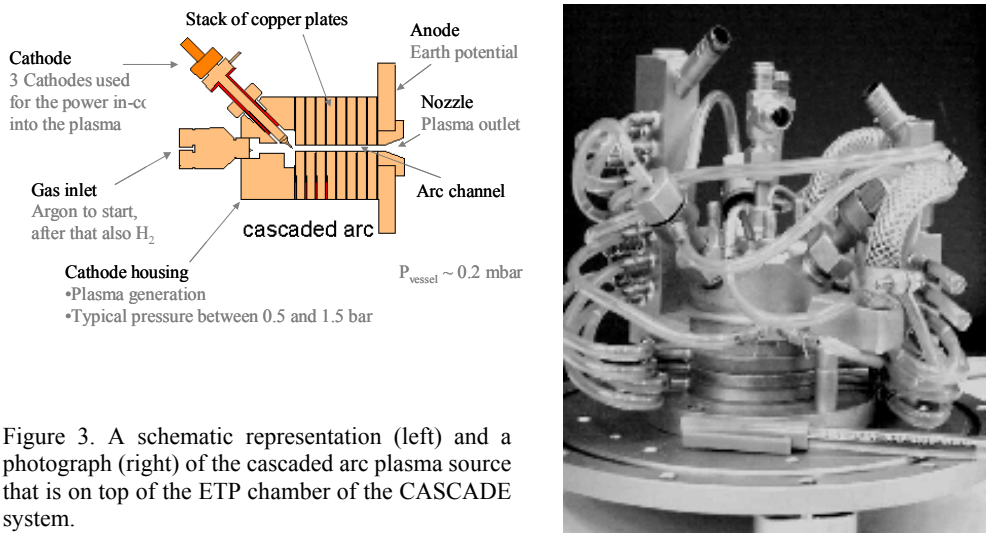

Figure 3. A schematic representation (left) and a photograph (right) of the cascaded arc plasma source that is on top of the ETP chamber of the CASCADE system.

substrate level a separately pumped mass spectrometer is attached to monitor the species present in the reaction chamber, especially silane (SiH_4). A pinhole can separate the reaction chamber from the mass spectrometer vacuum. This is necessary because the mass spectrometer operates below 10^{-5} mbar.

The entire set-up is operated through a graphical user interface. A more elaborate description of the CASCADE set-up can be found in reference [1]. All depositions described in this thesis are carried out on the CASCADE set-up.

2. Plasma analysis

Two plasma diagnostics are used in this thesis. Mass spectrometry is used to monitor the depletion of SiH_4 and electron beam induced fluorescence (EBIF) is used to determine the atomic hydrogen density.

2.1. Mass spectrometry

Apart from residual gas analysis of the background vacuum and leak detection with He, mass spectrometry is used to monitor the SiH_4 density in the plasma. Since the mass of SiH_4 (32 u) equals the mass of O_2, and oxygen is likely to be present in some amounts in the background gas of the vacuum system, the signal at mass 32 u cannot directly be used to monitor the silane density in the plasma. Instead, the silane density is monitored indirectly. The electron gun in the mass spectrometer not only ionises the SiH_4, but also cracks the SiH_4 into SiH_x with $x < 4$ and ionises these species. As a consequence, the masses 28 u, 29 u, 30 u, and 31 u are suitable to use for residual gas analysis. Mass 28 u is not used because at this mass also N_2 is measured. In this work mass 31 u is used because it gives the highest signal-to-noise ratio. It is assumed that the SiH_x radicals with $x < 4$ that are created in the deposition plasma will deposit on the

walls of the narrow entrance from the reaction chamber to the mass spectrometer and do not enter the mass spectrometer. The depletion of the SiH_4 can be calculated by measuring the mass spectrometer signal at mass 31 u with the plasma on and the plasma off, while the same gas flows are running. The depletion is the difference between the two signals relative to the signal with plasma off, and indicates the fraction of the injected SiH_4 that is decomposed in the plasma. At deposition conditions for microcrystalline silicon (μc-Si:H) it is essential that the background signal is subtracted correctly, because low SiH_4 densities are used. The background signal should be measured separately by turning off the SiH_4 flow for the plasma on and plasma off conditions. The depletion D then can be expressed as

$$D = \frac{\left(I(31)_{gas+SiH_4} - I(31)_{gas}\right) - \left(I(31)_{plasma+SiH_4} - I(31)_{plasma}\right)}{I(31)_{gas+SiH_4} - I(31)_{gas}} \quad (1)$$

in which I(31) denotes the signal from the mass spectrometer at mass 31, the subscript *plasma* denotes plasma with the Ar/H_2 mixture at which the deposition is carried out, the subscript *gas* denotes gas without plasma ignited with the same gas mixture fed into the plasma source, and the subscript *SiH_4* denotes that SiH_4 is injected into the reactor.

2.2. Electron beam induced fluorescence (EBIF)

For the measurement of the atomic hydrogen density a recently developed method has been improved as an easy alternative to existing laser diagnostic techniques: electron beam induced fluorescence (EBIF). This technique is described in detail in Chapter 3 or reference [2].

3. Thin film analysis techniques

For successful implementation in a solar cell the individual microcrystalline film should fulfil some minimum requirements [3]: the light conductivity should be larger than $1.5 \cdot 10^{-5}$ S/cm, the dark conductivity should be smaller than $1.5 \cdot 10^{-7}$ S/cm, the refractive index should be as high as possible (about 3.5 or higher for the refractive index at 2 eV), and the crystalline fraction should be above 30% [4]. However, these properties do not guarantee good device properties; the only way to judge the material quality is to apply them in a device. Below, the film analysis techniques and procedures that are used in this thesis are treated.

3.1. The samples

For the investigation of the material properties, thin silicon films have been deposited on Corning 1737 glass substrates of 30 mm by 100 mm and simultaneously on a piece (20 mm by 40 mm) of (100) c-Si wafer. The c-Si substrates were used as delivered, and the glass substrates first were cleaned in an ultrasonic acetone bath for at least 10

minutes and subsequently in an isopropanol bath for at least 10 minutes. After deposition the glass substrate is cut into four pieces of which, for film uniformity reasons, mostly only the middle two are used for analysis. A couple of pairs of coplanar aluminium contacts of about 300 nm thick are evaporated (electron-beam evaporation) on one of the two pieces. The spacing between the contacts of each pair is 0.5 mm. For DBP measurements (see next section) 5-mm long contact are used, while the conductivity is measured using 20-mm long contacts.

3.2. Reflection-transmission spectroscopy

For the measurement of the absorption spectrum a home-build reflection-transmission spectrometer is used. For wavelength selection the light from a halogen lamp is focussed onto a computer-controlled monochromator followed by a filter wheel (for first and second order selection). In front of the sample a beam splitter is mounted. The transmitted light (amplitude T) through the sample is detected by a silicon photo diode and the reflected light (amplitude R) enters a second silicon photo diode after reflection on the beam splitter. The absorption equals $1-R-T$. With this system an energy range from 1.1 to 3 eV can be covered.

In order to measure the light absorption in the band gap (0.7-1.8 eV) the set-up can be modified to allow dual-beam photoconductivity measurements (DBP). In that case the light is redirected using a mirror, a lens, and an optical fibre into a spot with a diameter of about 3 mm on the sample between the contacts. From the backside the sample is illuminated with red light. The current is measured by applying a voltage of 100 V over two 5-mm long Al contacts having a spacing of 0.5 mm. In order to increase the signal-to-noise ratio a lock in technique is applied using a chopper in front of the halogen lamp and a lock in amplifier.

Typical absorption curves that have been obtained are shown in figure 4. From

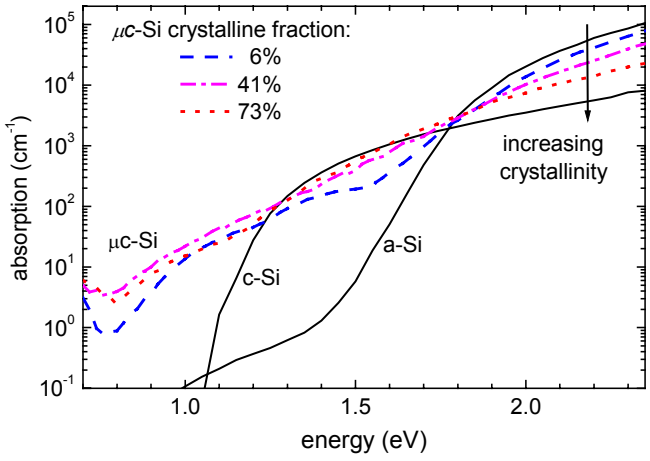

Figure 4. Light absorption spectra of μc-Si:H films containing different crystalline fractions. For comparison, spectra of a-Si:H and c-Si are included.

these curves the Tauc optical band gap is calculated or, more appropriate for μc-Si:H, the energy at an absorption of 10^4 cm^{-1} is deduced, the so-called E_{04} gap. From the interference fringes the refractive index at 2 eV is deduced together with the film thickness. The latter is used to calculate the growth rate. The refractive index is used as an indicator for film density: the higher the refractive index, the higher the density.

3.3. Photoconductivity

The photoconductivity is a measure for the excess charge carrier density under illumination. This density is dependent on the generation and recombination rate in the material. In turn, the recombination rate is determined by the defect density in the material. The interpretation of photoconductivity data measured using a co-planar structure on μc-Si:H is difficult. Firstly, it should be realised that μc-Si:H is not homogeneous and often grows in a column-like structure, parallel to the growth direction. Therefore the conductivity parallel to the substrate might very well be different from the conductivity perpendicular to the substrate [5]. In a solar cell the latter is important, but the conductivity in this direction is difficult to measure on a single film. On our samples with the co-planar electrode geometry the photoconductivity parallel to the substrate is measured. Secondly, μc-Si:H tends to contain pores. When the sample is exposed to air, the air will fill the pores and oxidise the silicon, not only at the sample surface, but also internally. This effects the conductivity, and, as a matter of fact, all electrical properties.

In order to measure the photoconductivity the sample is illuminated from the glass side with AM1.5 light from an Oriel solar simulator. The current is measured while varying the voltage on the 20-mm long contacts from 0 to 100 V in steps of 0.1 V (figure 5). The scan takes about 1 minute.

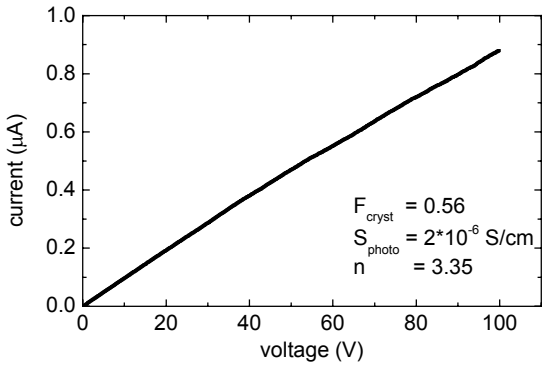

Figure 5. I-V curve of a illuminated μc-Si:H film.

3.4. Activation energy and dark conductivity

The activation energy (E_{act}) is retrieved from the slope of the Arrhenius plot of the dark conductivity, σ_d, as shown in figure 6 In order to measure the temperature dependence of the dark conductivity a temperature scan from 130°C to 60°C is applied to the

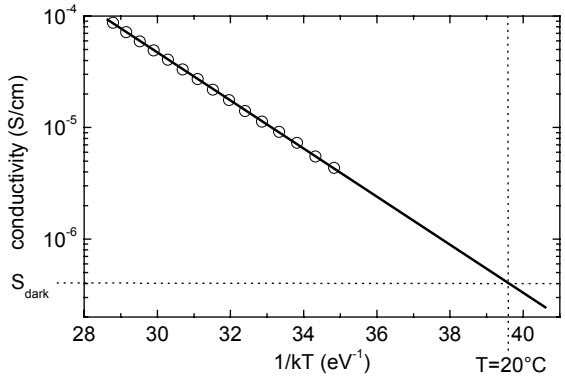

Figure 6. Arrhenius plot of the dark conductivity of a μc-Si:H film.

sample. The temperature is changed in steps of 5°C and the total scan takes about 30 minutes. The scan starts with annealing the sample at 130°C for 30 minutes. A voltage of 100 V is applied on the 20-mm long contacts and the current is measured. The measured curve is extrapolated to obtain the dark conductivity at 20°C. The measurements are carried out under atmospheric conditions in air. For this characterisation method the same remarks hold as for the photoconductivity measurements. The activation energy characterises the temperature dependence of the dark conductivity and thus, when assuming that the carrier mobility is temperature independent, of the free charge carrier density. It is therefore a good measure for the energy difference between the Fermi level and the conduction band for n-type material or between the Fermi level and the valence band for p-type material. The relationship between the dark conductivity and the activation energy is described by:

$$\sigma_d(T) = \sigma_0 \cdot e^{-\frac{E_{act}}{kT}}, \tag{2}$$

in which T is the temperature and k is Boltzmann's constant. It is very important to know the Fermi level position of the p-type and n-type doped layers used in thin-film silicon solar cells, because these layers determine the internal electric field strength that is responsible for the separation of the electron-hole pairs that are generated by the absorption of light in the solar cell. For truly intrinsic material the Fermi level should be positioned in the middle of the band gap, but due to the asymmetrical distribution of gap states (defects in *a*-Si:H or at the grain boundaries between the crystallites) this is not the case. For μc-Si:H the Fermi level sometimes is shifted towards the conduction band due to oxygen impurities in the material that originate in small amounts from the process gas and out gassing of the vacuum system.

3.5. Fourier-transform infrared absorption (FTIR)

Infrared absorption spectra are measured with a Bruker Vector 22 Fourier-transform infrared absorption spectrometer (FTIR). An example of such a measurement is shown

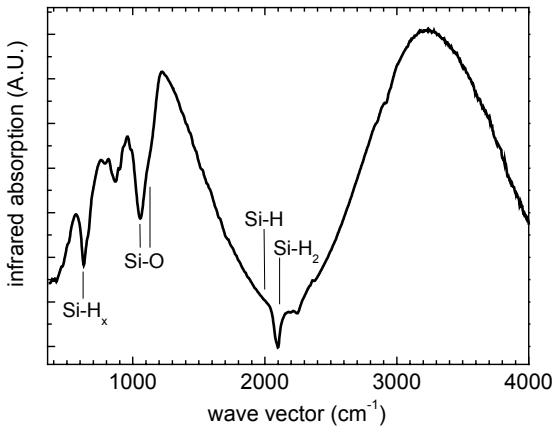

Figure 7. Typical FTIR measurement of a μc-Si:H film.

in figure 7. From the interference fringes the thickness and the refractive index for infrared light is deduced. Furthermore, the presence of oxygen in the films can be observed, the hydrogen content can be derived from the absorption at 640 cm^{-1} by calculating the integrated absorption, and the hydrogen bonding configuration can be seen from the stretching modes around 2000 and 2100 cm^{-1}, although there is some dispute about the interpretation of these latter absorption energies. Generally, the absorption at 2000 cm^{-1} is attributed to Si-H bonds in the bulk material and the absorption at 2100 cm^{-1} to Si-H_2 bonds in the bulk material and to Si-H bonds at (void) surfaces.

3.6. Raman spectroscopy

With Raman spectroscopy the crystallinity of the films can be examined. The technique relies on the excitation of phonons. Since phonon energies in crystalline silicon differ from the phonon energies in amorphous silicon clear fingerprints of both materials appear in the spectra. The Raman spectra are collected with a Renishaw Ramascope system 2000 in backscattering geometry, which is used from the Department of Chemical Technology, section R&CE, of the Delft University of Technology. The excitation wavelength is 514.5 nm and the illumination is 2 mW in a spot of about 1-μm diameter. The monochromator has a grating with 1800 lines per mm. The measurement time is 5 minutes per film, unless stated otherwise (for example for the thin microcrystalline p layers in Chapter 4). The interpretation of the spectra and the extraction of the crystalline fractions are discussed in chapter 4 or reference [6].

3.7. X-ray analysis (XRD, SAXS)

Information on the crystalline fraction and the crystal orientation can be obtained with XRD. Incoming x-rays are scattered on the lattice planes of crystalline material. A typical XRD spectrum is shown in figure 8 for μc-Si:H as well as for a-Si:H. The

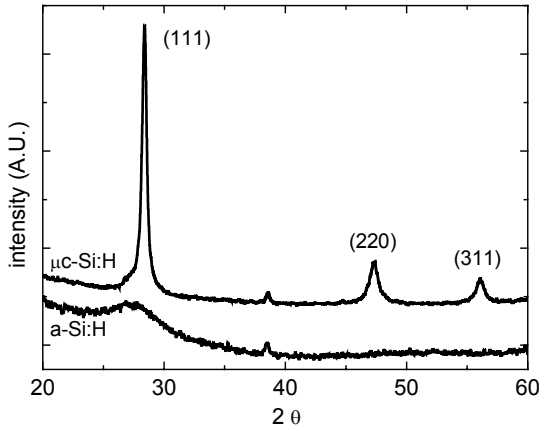

Figure 8. XRD data of a *μc*-Si:H film and an *a*-Si:H film.

incident angle (and the detection angle) is varied and the scattering intensity peaks if the incident angle and the lattice plane distance satisfy the diffraction conditions. Finite size effects result in peak broadening and therefore from the peak width the crystallite size can be determined. Even amorphous silicon shows a smooth profile because inter-atomic distances deviate only slightly from the fixed crystalline values. Therefore it is possible also to extract the amorphous and crystalline fractions from XRD profiles.

When the X-rays enter the substrate under a very small angle with the substrate surface, then by looking at the scattered X-rays information on inhomogeneities like voids in the material can be examined. This is used in Chapter 6. Special samples have been prepared for this technique consisting of a Al foil of 10 micron thick as a substrate with a 5 micron thick *μc*-Si:H film on top. Before analysis this sample is folded five times, to increase the signal strength.

Except for the work carried out at the Colorado School of Mines, all XRD analyses are carried out at the materials science department of the Delft University of Technology on a Bruker-Nonius D5005 θ/θ diffractometer with diffracted beam graphite monochromator, using Cu-α radiation. Crystalline (100) silicon substrates are used and the samples are tilted by 2° to prevent the diffracted beams from the substrate to enter the detector.

3.8. Electron microscopy

To investigate the material structure also electron microscopy has been used on some samples. Scanning electron microscopy (SEM: Philips XL30SFEG) has been carried out on the cutting edge of cut samples. To avoid charging of the samples by the electron beam samples on *c*-Si substrates were used. An example of these pictures is shown in figure 9.

High-resolution transmission electron microscopy (HRTEM: Philips CM30) has been carried out at the materials science department of the Delft University of Technology. In the bright field images the voids are very well visible (figure 10). The

high-resolution images reveal the individual atoms in the crystalline parts of the material (see the cover of this book).

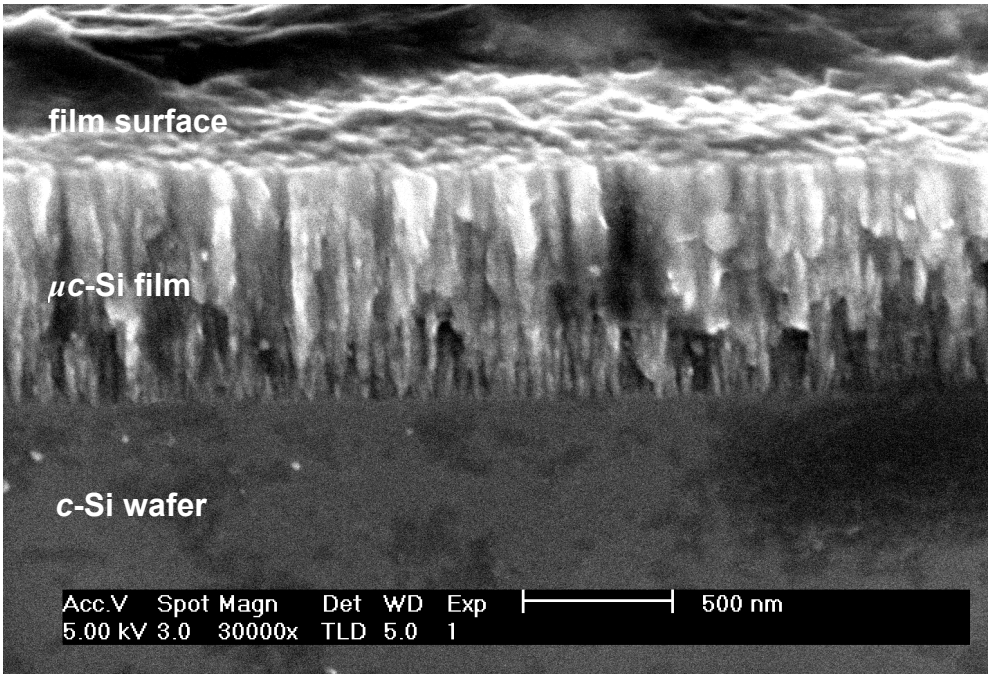

Figure 9. Scanning electron microscope picture of the cutting edge of a *μc*-Si:H film.

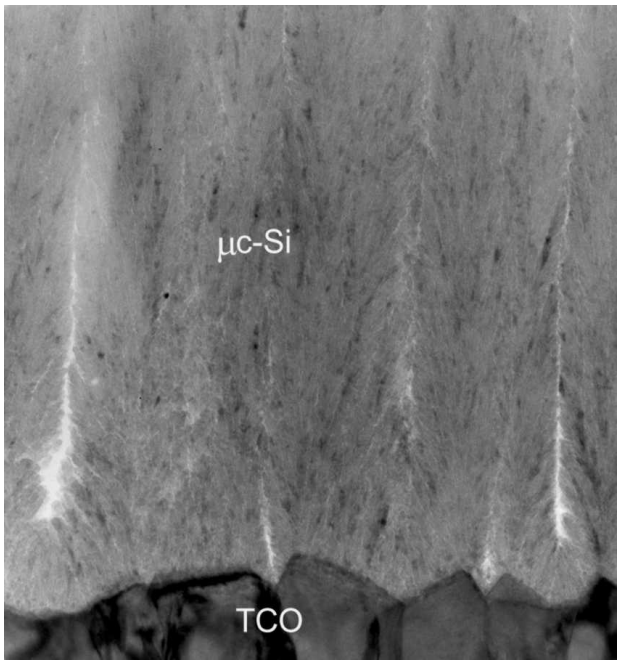

Figure 10. Transmission electron microscope bright field picture of a *μc*-Si:H solar cell. The entire picture is 1 μm high.

4. Solar cell layout and analysis

4.1. Preparation

The p-i-n deposited solar cells are deposited on Asahi U-type TCO covered glass substrates. Some substrates are covered with ZnO:Al to prevent the SnO_2 from reduction by the hydrogen in the plasma. For characterisation purposes an Al bus bar is deposited on the side of the substrates in order to reduce the series resistance of the TCO. Then a microcrystalline p-type layer is deposited following the recipe as developed in Chapter 4. The substrate is moved to the ETP reaction chamber of the set-up and the intrinsic layer is deposited. The substrate is moved back to the RF PECVD chamber and the microcrystalline n type layer is deposited. To prevent air to enter the porous material a 5 nm thin amorphous silicon n-type layer is deposited. The solar cell is put in the load lock for 30 minutes to cool down. When the cell is taken out of the load-lock an Al mask is attached and it is immediately put into the metal evaporation machine. A silver back contact (100 nm) covered by Al (200 nm) finishes the solar cell. The mask is designed to give solar cells of different sizes, of which there are four with the size of 0.1 cm^2.

4.2. Analysis

The conversion efficiency, the short-circuit current density, J_{sc}, the open-circuit voltage, V_{oc}, and the fill factor, *FF*, of the solar cells are calculated from *J-V* curves measured during AM1.5 illumination. Figure 11 shows an example of such a measurement on a typical *a*-Si:H solar cell. Furthermore, the spectral response is measured using bias voltages of –0.5, 0.0, 0.4, and 0.6 V (figure 12 shows an example of such a measurement on an *a*-Si:H solar cell) with a home built set-up. It consists of a halogen lamp followed by a filter wheel containing 35 band transmission filters covering an energy range from 1.30 to 3.25 eV. A chopper allows the use of a lock in technique to enhance the signal-to-noise ratio. The light is focussed on the solar cell.

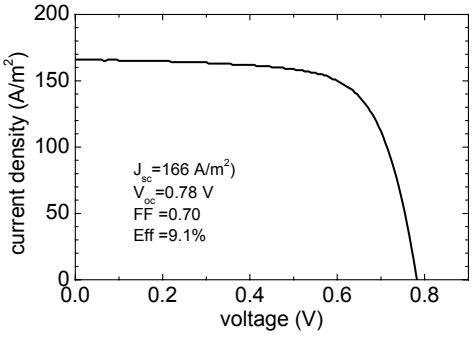

Figure 11. Typical J-V curve of an *a*-Si:H solar cell. Sample preparation by Ben Girwar.

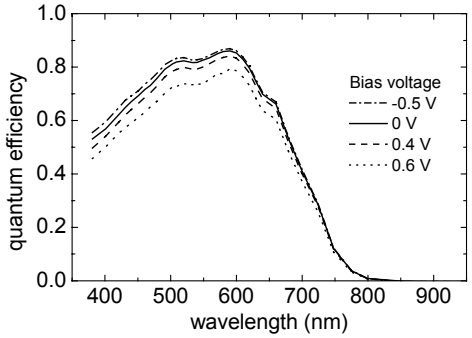

Figure 12. Typical spectral response measurement using different bias voltages of an *a*-Si:H solar cell.

The contacts are connected to the power supply that generates the bias voltage and to the lock in amplifier. A red bias illumination is applied to make sure the quantum efficiency is measured under conditions close to operating conditions. This bias light originates from a second halogen lamp with a red filter and is not chopped. The set-up is calibrated with a calibrated photo diode.

References

[1] B.A. Korevaar, C. Smit, R.A.C.M.M. van Swaaij, A.H.M. Smets, W.M.M. Kessels, J.W. Metselaar, D.C. Schram, and M.C.M. van de Sanden, Proc. of 16th European Photovoltaic Solar Energy Conference, 2000, B119.

[2] C. Smit, G.J.H. Brussaard, E.C.M. de Beer, D.C. Schram, and M.C.M. van de Sanden, Plasma Sources Sci. and Technol. **13**, 1 (2004).

[3] R.E.I. Schropp and M. Zeman, Amorphous and microcrystalline silicon solar cells (1998, Kluwer academic publishers, Dordrecht, the Netherlands)

[4] K. Shimakawa, J. Non-Cryst. Solids **266-269**, 223 (2000).

[5] K. Hattori, Y. Musa, N. Murakami, N. Deguchi, and H. Okamoto, J. Appl. Phys. **94**, 5071 (2003).

[6] C. Smit, R.A.C.M.M. van Swaaij, H. Donker, A.M.H.N. Petit, W.M.M. Kessels, and M.C.M. van de Sanden, J. Appl. Phys. **94**, 3582 (2003).

Chapter 3

Electron beam induced fluorescence measurements
of the degree of hydrogen dissociation in hydrogen plasmas

C. Smit[1,2], G.J.H. Brussaard[1], E.C.M. de Beer[1], D.C. Schram[1],
and M.C.M. van de Sanden[1]

[1] *Eindhoven University of Technology, Department of Applied Physics, P.O. Box 513, NL-5600 MB Eindhoven, the Netherlands*
[2] *Delft University of Technology, DIMES, P.O. Box 5053, 2600 GB Delft, the Netherlands*

Plasma Sources Sci. Technol. **13**, 1 (2004)

Abstract

The degree of dissociation of hydrogen in a hydrogen plasma has been measured using electron beam induced fluorescence. A 20 kV, 1 mA electron beam excites both the ground state H atom and H_2 molecule into atomic hydrogen in an excited state. From the resulting fluorescence the degree of dissociation of hydrogen is determined. In addition, the absolute atomic hydrogen density can be determined if the gas temperature and pressure are known without any additional calibration. To check the consistency of the method the fluorescence from the first four Balmer transitions is measured. It is demonstrated that this technique can be applied in hydrogen and argon-hydrogen plasmas with a pressure of up to 1 mbar and 0.2 mbar, respectively.

1. Introduction

In many reactive plasmas used for plasma deposition or etching atomic radicals play an important role. For example, silane-containing plasmas can be used for deposition of amorphous silicon [1]. In many cases, to improve the quality of film deposition the silane is diluted in hydrogen. In this case atomic hydrogen is believed to play an important role in the decomposition of the precursor gas, as well as have beneficial effects on the surface chemistry. Another example is diamond deposition in which case atomic hydrogen is involved in the decomposition of the hydrocarbon gas in addition to the preferential etching of graphitic sites at the film surface. Similarly, during the deposition of microcrystalline silicon, atomic hydrogen is known to have a significant influence on the crystallisation of the growing film [2]. Therefore to understand the growth process it is of paramount importance to have a reliable measurement of the atomic hydrogen density in the plasma. Yet other examples where atomic radicals play a role are fluorine etching of crystalline silicon, nitridation of steel, and the stripping of photo resist by oxygen plasma. In this paper we present a relatively easy to apply technique, electron beam induced fluorescence (EBIF), for determining the density of atomic hydrogen.

A plasma can be studied just by analysing the radiation that comes from the decay of ionised and excited atoms and molecules that are naturally present. But if the particles that need to be investigated are in the ground state, then an external source is needed for the excitation. High excitation energies are required for overcoming the energy difference between the ground state and the excited states (e.g. atomic hydrogen: 10.2 eV or 121.6 nm). For this a deep UV lamp can be used and the light absorption in the plasma can be measured, as shown by Takashima et al. [3]. The difficulty is that, depending on the hydrogen density, the mean free path of the high-energy photons is small (several mm in our case) because the plasma is optically thick for these transitions. A laser could also be used as a light source. The aforementioned drawbacks remain, but now the photon energy can be tuned to a resonant transition. Only the particles under investigation are excited, and the excited state can also be chosen. However, deep UV lasers are expensive, the optical path to the plasma has to be evacuated and special optical elements are required [4].

To avoid these problems in measurement of the atomic hydrogen density in plasmas several solutions have been proposed. Two-photon absorption laser induced fluorescence (TALIF) is now most common [5, 6]. In this technique the photon energy is half the transition energy, which relieves the demands on the optical system. Quite some laser intensity or measurement time is needed because of the small cross-section for the two-photon absorption process. Also a complicated calibration is necessary for obtaining absolute values [5]. A second technique for detecting atomic hydrogen is four wave mixing [7]. As in TALIF, a laser beam is used for the two-photon absorption process, but now together with a laser that is slightly detuned from the Balmer α line at 656 nm. The signal wave frequency is close to the Lyman α transition. Since four-wave mixing is a two-photon process the cross-section is small, as in the TALIF process. However, the signal wave is emitted within a very small solid angle, which increases the signal-to-noise ratio. Another technique was introduced by the De Graaf [8]. He inserted an RF probe in the plasma to excite the ground state hydrogen atoms locally

with a radio frequency electro-magnetic field. Although this method is relatively simple, the probe itself of course will disturb the plasma to some extend.

Electron beam excitation spectroscopy has been used in the past for the investigation of supersonic gas jet expansions [9]. Recently it has been used for the measurement of the temperature in a low-temperature plasma. In this paper we wish to use this technique as a plasma diagnostic tool. In this technique an electron beam is used to excite ground state hydrogen atoms. The electron energy is in the kiloelectronvolt range so it easily exceeds the excitation energy. The cross-sections for electron-induced excitation are reasonable, and the experimental set-up is relatively straightforward. The optical axis of the detection branch and the electron beam are crossed, giving good spatial resolution. As we will show, the measured quantity is in fact the degree of dissociation of hydrogen, i.e. the ratio of the atomic hydrogen to molecular hydrogen. The absolute atomic hydrogen density can be determined if the hydrogen molecule density is known, e.g. using the reactor pressure. No additional calibration is needed, which is one of the most important advantages of the proposed technique. In principle, the technique discussed is not limited to atomic hydrogen, but can be applied to determine the density of other atomic species, such as atomic fluorine and chlorine, using a similar approach.

The determination of the degree of dissociation of hydrogen from the measured fluorescence is not straightforward even in a pure hydrogen plasma. The high-energy electrons from the electron gun not only excite the hydrogen atoms, but also dissociate the hydrogen molecules. This is a mechanism of production of excited hydrogen atoms that must be corrected for. Furthermore all possible excited states will be populated, which will contribute via several cascade decay processes to the population of the lower excited state from which the fluorescence is detected. But in the case of hydrogen, where most of the cross-sections and radiative decay constants are well studied [10], these effects can all be included in the analysis and determination of the final degree of dissociation. In the next section we will discuss the relevant theory, which is needed to determine the degree of dissociation of hydrogen from electron beam fluorescence measurements. The complications due to re-absorption processes and the corrections necessary are discussed as well. In section 3 and 4 we will discuss the application of the technique to a hydrogen and hydrogen containing expanding thermal plasma (ETP) [11]. The accuracy, applicability, and sensitivity of the technique are addressed. Section 5 contains our conclusions.

2. Theory

2.1. The principle of electron beam induced fluorescence

High-energy electrons (20 keV) from an electron gun excite the hydrogen atoms in a hydrogen plasma ($e + H \rightarrow e + H^*$ (excited state $p \geq 2$)). In a purely atomic hydrogen plasma the fluorescence signal will be proportional to the atomic hydrogen density. Excitations to all possible states will occur, so the fluorescence of several decay transitions is available. In practice, only the Balmer series (decay to the $p = 2$ state: $H^*(p \geq 3) \rightarrow H^*(p = 2) + h\nu$) will be used, because the radiation from these transitions is

easy to detect. To determine the atomic hydrogen density, the excitation cross-section and the radiative decay rate must be known. The excited state from which the fluorescence is measured will not only be populated by direct excitation, but also by cascaded decay processes from higher excited states. This must also be taken into account.

However, no pure atomic hydrogen plasmas exist. Therefore, a second important process is that electrons from the gun dissociate hydrogen molecules into excited hydrogen atoms (dissociative excitation). This is also an important source of fluorescence from atomic hydrogen, but it is proportional to the H_2 density. To correct for this, the fluorescence caused by the electron beam interacting with the H_2 gas must be measured separately, with the plasma switched off. This signal from molecular hydrogen can be used as a reference signal in the calculation of the degree of dissociation from the measurements. This makes further calibration unnecessary, which is a big advantage of the EBIF technique.

To derive a closed expression for the degree of dissociation in a hydrogen plasma we have to make some additional assumptions. First of all we will assume that the plasma is optically thin for all optical transitions. This means that no re-absorption of generated fluorescence has to be considered. Since the fluorescence is induced by fast electrons from the e-beam we will restrict ourselves to a description within the so-called corona regime [12]. In this regime the population of excited states is dominated by electron impact excitation of ground state atoms and the destruction processes of excited states is by radiative decay. To determine the degree of dissociation three fluorescence measurements need to be considered: 1) a measurement with plasma on and electron beam on, 2) a measurement with only plasma on to measure the plasma emission, and 3) a measurement with only the electron beam on. The measured fluorescence signals are, respectively, $S_{pq,beam}^{plasma}$, S_{pq}^{plasma}, and $S_{pq,beam}$ [1]. In table 1 the measurements are related to expressions derived in Appendix C. As can be seen, the signal $S_{pq,beam}^{plasma}$, the number of photons that is detected per unit time from the transition from state p to q and which is proportional to the density of the state p (given by n_p), is due to spontaneous emission (including cascade processes), the excitation from the hydrogen ground state (density n_1) by the electron beam, and the dissociative excitation of H_2 present in the plasma (density $n_{H_2}^{plasma}$). On the other hand the signal $S_{pq,beam}$ is

Table 1. Expressions that apply to the three different measurements to obtain the atomic hydrogen density.

Plasma on/e-beam on	$\underline{n} \approx -\underline{\underline{A}}^{-1} \cdot \left(\underline{P} + \underline{k}^{diss} n_{e-beam} n_{H_2}^{plasma} + n_1 n_{e-beam} \underline{k}^{exc} \right)$	$S_{pq,beam}^{plasma}$
Plasma on/e-beam off	$\underline{n} \approx -\underline{\underline{A}}^{-1} \cdot \underline{P}$	S_{pq}^{plasma}
Plasma off/e-beam on	$\underline{n} \approx -\underline{\underline{A}}^{-1} \cdot \underline{k}^{diss} n_{e-beam} n_{H_2}^{gas}$	$S_{pq,beam}^{gas}$

[1] These signals are not corrected for background signals. It is discussed later on that by using a modulated e-beam only the AC component is considered.

proportional to the gas density, $n_{H_2}^{gas}$, which is not necessarily equal to the H_2 density under plasma conditions because the plasma could have a different gas temperature. In table 1, Matrix $\underline{\underline{A}}$ contains the radiative decay, $\underline{k}^{diss}$ and $\underline{k}^{exc}$ contain the excitation rates for dissociative excitation of H_2 and excitation of ground state atomic hydrogen, respectively, $\underline{P}$ contains all other plasma chemistry that is not related to the electron beam, and $n_{e\text{-}beam}$ is the electron density in the electron beam. Using the expression given in table 1 the following expression for n_1 can be derived:

$$n_1 = n_{H_2}^{plasma}\left(\tau\left(\frac{n_{H_2}^{gas}}{n_{H_2}^{plasma}}\right)-1\right)\alpha_p \,. \tag{1}$$

The quantity

$$\tau = \frac{S_{pq,beam}^{plasma} - S_{pq}^{plasma}}{S_{pq,beam}^{gas}} \tag{2}$$

only contains experimental values, and

$$\alpha_p = \frac{\left(-\underline{\underline{A}}^{-1}\underline{k}^{diss,beam}\right)_p}{\left(-\underline{\underline{A}}^{-1}\underline{k}^{exc,beam}\right)_p} \tag{3}$$

contains only transition probabilities and excitation rates, which are defined in Appendix A and of which the values are given in Appendix B. The excitation rates depend on the electron energy in the electron beam (the suffix "beam" denotes excitations by electrons from the electron gun). In fact, α_p is equal to the ratio between the density of excited atomic hydrogen that originates from excitation from the ground

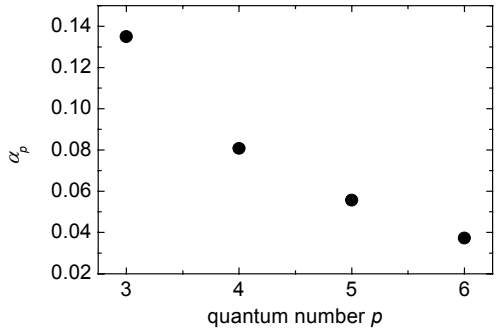

Figure 1. Relation between α_p and the quantum number p of the excited state when the incident electron energy is 20 keV.

state to the H density from dissociation of H_2. As can be seen in figure 1, highly excited states are predominantly produced from ground state atomic hydrogen. Because it is the ground state atomic hydrogen that we are interested in and the fluorescence coming from dissociative excitation is the unwanted side effect, detection of higher Balmer lines like Balmer β, γ, or even δ seems favourable. On the other hand, the total fluorescence signal from these lines is smaller. This is due to a lower production rate for the higher states and because higher states have a higher probability of decaying through other states which does not result in Balmer radiation.

Equation 1 relates the measurement of the ground state density, n_1, to the relative measurement, τ, and the H_2 molecular density, both in the plasma-on situation as well as in the plasma-off situation. If the degree of dissociation is small and the H_2 density is not affected by the plasma, the degree of dissociation,

$$\beta = \frac{n_1}{n_{H_2}^{plasma} + n_1}, \tag{4}$$

can be determined directly, without any calibration if the detection optics are identical during the three fluorescence measurements of table 1.

2.2. The optical thickness of the plasma: re-absorption correction

When the atomic hydrogen density is relatively high, re-absorption of emitted photons within a certain detection volume can become important. This can affect the measured quantities $S_{pq,beam}^{plasma}$ and $S_{pq,beam}$. This will be the case for higher pressures or higher degrees of dissociation. If we look, for example, at the decay of the $p = 3$ state of the hydrogen atom, it can decay to $p = 2$ or to the ground state ($p = 1$). The photon from the $p = 3$ to $p = 2$ transition (Balmer α line) is the photon that we want to detect, and the mean free path will be long enough (since most atoms are in the ground state) to escape the plasma. On the other hand, the photon from the $p = 3$ to $p = 1$ transition can be re-absorbed, exciting a ground state atom to the $p= 3$ state. This state will again have a probability of decaying to the $p = 2$ state or to the ground state. This results in more Balmer α decay compared with the case without re-absorption. If the re-absorption is 100%, then effectively the decay to the ground state does not exist, and the corresponding radiative decay matrix element in matrix $\underline{\underline{A}}$ should be corrected to zero. In general, the radiative decay matrix can be corrected for re-absorption by means of an escape factor [10]. This will influence the balance between radiation and the occupation of all excited states in the entire plasma. In order to detect the extra Balmer α radiation that is caused by re-absorption, the generation of the Lyman β photon as well as the re-absorption event must take place within the volume that is imaged onto the detector. Therefore only re-absorption in the detection volume is relevant in the correction.

We can account for the re-absorption by correcting the radiative decay matrix, $\underline{\underline{A}}$, to $\underline{\underline{A}}_{corr}$. This changes the expression for α_p to $\alpha_{p,corr}$. We have to realize that the re-absorption will not be significant in the case where the plasma is not on, because then

the atomic hydrogen density is very low. This introduces an additional factor, Π_p, in the expression for n_1 in equation 1. In Appendix D we have calculated the escape factor and the corrected radiative decay matrix $\underline{\underline{A}}_{corr}$. We get

$$n_1 = n_{H_2}^{plasma}\left(\tau\Pi_p\left(\frac{n_{H_2}^{gas}}{n_{H_2}^{plasma}}\right)-1\right)\alpha_{p,corr}\,, \tag{5}$$

where

$$\Pi_p = \frac{\underline{\underline{A}}^{-1}\,\underline{k}^{diss,beam}\Big|_p}{\underline{\underline{A}}_{corr}^{-1}\,\underline{k}^{diss,beam}\Big|_p} \tag{6}$$

and

$$\alpha_{p,corr} = \frac{\underline{\underline{A}}_{corr}^{-1}\,\underline{k}^{diss,beam}\Big|_p}{\underline{\underline{A}}_{corr}^{-1}\,\underline{k}^{exc,beam}\Big|_p}\,. \tag{7}$$

Note that the value of $\alpha_{p,corr}$ is not very different from the value of α_p because the corrected decay matrix is in the numerator as well as in the denominator. So the correction is mainly in the term Π_p. The structure of equations 5 to 7 is such that the determination of the degree of dissociation is less straightforward and is done using a numerical algorithm.

3. Experiment

3.1. The plasma

The plasma under investigation expands from a cascaded arc plasma source [13] at a pressure of 0.2-1.0 bar into the reactor at a pressure of 0.2-1.0 mbar. This plasma source can be operated in pure hydrogen as well as argon/hydrogen mixtures. The plasma is created by a dc discharge (current 55 A) in a 4 mm wide channel between three cathode tips and an anode plate. The ETP, a remote plasma, is described in detail in reference 1. The reactor pressure can be varied by adjusting the gate valve between the reactor and the pump. The measurements are performed at 500 mm from the plasma source, on the axis of the reactor. To calculate the absolute density of atomic hydrogen from the degree of dissociation, we must know the density of molecular hydrogen under plasma conditions. The molecular hydrogen density under plasma off conditions can be determined from the ideal gas law and the pressure.

3.2. The EBIF set-up

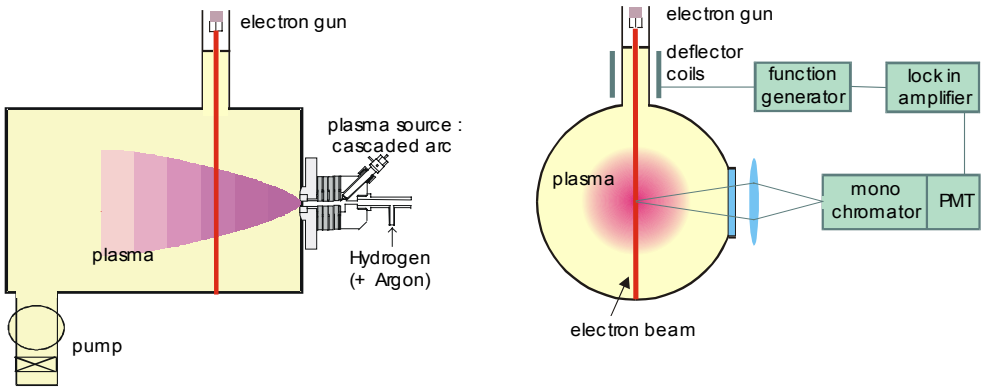

Figure 2. Experimental set-up.

The experimental EBIF set-up is shown in figure 2. The electron beam and the detection branch cross with a 45° angle in a plane perpendicular to the plasma expansion. The electron gun is a homemade triode gun from the charged particle optics group of the Delft University of Technology. It is differentially pumped and a 2 mm aperture in the anode separates the gun vacuum from the reactor. This results in a gun pressure of about 10^{-4} mbar at a reactor pressure of 1 mbar. It is operated at 20 kV and 1 mA. A magnetic lens is installed to focus the beam at the centre of the reactor. At the focus the beam diameter is about 2 mm. A deflector set is mounted to align the beam properly.

It is important to note that the numerator as well as the denominator of the measured quantity τ (equation 2) contains a subtraction of a measurement with the electron beam on and with the electron beam off. This makes the experiment extremely suitable for a lock-in technique with a chopped electron beam and phase-sensitive detection. This will increase the accuracy of the measurement and will also minimise the influence of stray light and other sources of noise like dark current. Therefore a function generator is connected to the deflection coils to deflect the beam periodically out of the detection volume to simulate chopping. It is set at a triangular-shaped output voltage as function of time with a frequency of about 13 Hz. Since the beam will cross the detection volume twice in one period of the function generator output, the lock-in amplifier (EG&G 7260) is set to lock at twice the modulation frequency, i.e. at 26 Hz. The integration time of the lock-in amplifier is varied between 5 and 20 seconds, depending on the signal strength.

The detection branch consists of a set of two plano-convex lenses, each with a focal length of 40 cm, imaging the centre of the reactor one-to-one on the 3 mm diameter entrance of an optical fibre. The exit of the fibre is rectangular (width is 2 mm) for efficient coupling of the light into a Bentham M300 monochromator. The exit slit is set at 2 mm and is directly followed by a Hamamatsu R928 photo multiplier (at

1240V) mounted on the exit slit. This gives a spectral resolution of about 0.5 nm. The photo multiplier output current is converted to a voltage by a sensitive current-to-voltage amplifier (1 nA results in about 1 mV) and then connected to the voltage input of the lock-in amplifier.

3.3. The plasma and gas temperatures

A complication in the determination of the degree of dissociation arises in the ETP set-up because the molecular hydrogen density changes when the plasma is turned on due to an increase in the heavy particle temperature. In the case where the pressure is constant during the plasma-on and plasma-off fluorescence measurements, the degree of dissociation is given by:

$$\beta = \left(\tau \Pi_p \left(\frac{T_{plasma}}{T_{gas}} \right) - 1 \right) \frac{\alpha_{p,corr}}{1 - \alpha_{p,corr}} . \tag{8}$$

It should be stressed that equation 8 is different if the fluorescence measurements are carried out under constant pumping speed conditions. The parameters in equation 8 that need to be determined are τ and the ratio between the plasma and gas temperatures. The gas temperature during the plasma off measurement is equal to room temperature, leaving the plasma temperature to be determined. In principle one can obtain the plasma temperature from the Doppler width of a spectral line of spontaneous emission. Another possibility is to determine the gas temperature from the rotational temperature utilizing e-beam-induced H_2 Fulcher band emission. In this work we employed the electron beam to determine the ratio T_{plasma}/T_{gas} by measuring the EBIF of helium that we added in small amounts (0.35 slm) for this purpose in the background gas. We assume that the helium will perfectly mix with the hydrogen (and Argon); i.e. the helium gas will acquire the same gas temperature as the plasma particles. Moreover, since we are dealing with a remote plasma, the helium does not influence the plasma chemistry. The detected EBIF from the 1s3p $\rightarrow$ 1s2s He transition is proportional to the helium density, and is measured in the plasma-on and plasma-off situations. The expression for the degree of dissociation changes to

$$\beta = \left(\tau \Pi_p \left(\frac{n_{He}^{gas}}{n_{He}^{plasma}} \right) - 1 \right) \frac{\alpha_{p,corr}}{1 - \alpha_{p,corr}} , \tag{9}$$

where the gas density ratio can be calculated from the fluorescence measurements in the presence of helium as follows,

$$\frac{\hat{S}_{He,beam}^{gas}}{\hat{S}_{He,beam}^{plasma}} = \frac{n_{He}^{gas}}{n_{He}^{plasma}} = \frac{T_{plasma}}{T_{gas}} , \tag{10}$$

where $\hat{S}^{gas}_{He,beam}$ and $\hat{S}^{plasma}_{He,beam}$ refer to the ac measurements using the lock-in amplifier. The amount of helium gas injected is chosen such that the inaccuracy in the temperature is small in comparison with other errors.

3.4. Measurements

A measurement of the degree of dissociation consists of a lock-in amplifier read-out while the plasma is on, $\hat{S}^{plasma}_{pq,beam}$ (cf. equation 2, but now using the modulated e-beam technique and the lock-in amplifier) and a read-out while the plasma is off, $\hat{S}^{gas}_{pq,beam}$. In the plasma-off case the same gas flows are running and the reactor pressure is kept equal. If we set the integration time of the lock-in amplifier to 10 seconds, then the inaccuracy of these measurements is 1-2% in the case of a pure hydrogen plasma when detecting the Balmer α line. The inaccuracy is 2% for detection of the Balmer β line and 5% for the Balmer γ and δ lines. When Ar is added to the plasma the inaccuracy increases to 10% at 1.5 slm Ar and 2.0 slm H_2 (Balmer α line). With these numbers the degree of dissociation of hydrogen can be calculated using equation 1. The actual number of emitted photons per unit volume cannot be determined, because the detection efficiency is not known. The error in the calculated degree of dissociation is very sensitive to the measurement inaccuracy in τ. This number is close to 1 (the degree of dissociation β is about 1-10%), so after subtracting 1 (cf. equation 1) the relative error is increased. It is clear from equation 1 that this effect is reduced when α_p decreases (i.e. for higher quantum numbers) because then the measured values of τ are higher.

We measured the atomic hydrogen density of the plasma for an Ar/H_2 plasma ([Ar](slm)/[H_2](slm)=1.5/2.0) and in a pure hydrogen plasma for reactor pressures ranging from 0.2 to 1.0 mbar. For the pure hydrogen plasma we measured the fluorescence of the first four Balmer lines (transitions from p = 3, 4, 5, and 6 to p = 2 at wavelengths of 656 nm, 486 nm, 434 nm, and 410 nm respectively). When argon is admixed, the argon gives too much background radiation on electron excitation to be able to measure the hydrogen Balmer β, γ, and δ lines, unless a better spectral resolution is obtained for resolving the hydrogen lines from the argon lines.

3.5. Applicability and detection limit

EBIF is a relatively easy technique for measuring the atomic hydrogen in hydrogen plasmas. There are a few limitations though. We can estimate the detection limit for the degree of dissociation, realizing that the number of counts coming from directly excited atomic hydrogen must be higher than the noise in the number of counts coming from dissociated H_2:

$$\sqrt{c_{H_2}} < c_H \Rightarrow \sqrt{n_{H_2} n_e k_p^{diss} \eta t V_{\det}} < n_H n_e k_{1p} \eta t V_{\det} \ , \qquad (11)$$

where c_{H_2} and c_H are the number of counts coming from directly excited atomic hydrogen and the number of counts coming from dissociated H_2, respectively, n_{H_2} is the molecular hydrogen density, n_H is the atomic hydrogen density, n_e is the electron density in the electron beam (all densities have unit m^{-3}), η is the detection efficiency, t is the measurement time in seconds, and V_{det} is the detection volume that is imaged on the detection system in cubic metres. For low degrees of dissociation, n_H is equal to βn_{H_2}. Now the detection limit can be calculated:

$$\beta > \frac{1}{k_{1p}} \sqrt{\frac{k_p^{diss}}{n_e n_{H_2} \eta t V_{\det}}} . \tag{12}$$

The reaction rates are given in Appendix B. We can estimate the numbers in equation 12 that are applicable in the experiment described in this paper: $n_e = 3 \cdot 10^{13}$ m^{-3} (1 mA and 20 kV in a 2-mm diameter beam), $n_{H_2} = 0.5 \cdot 10^{22}$ m^{-3} at 0.2 mbar at 293 K, V_{det} = 15 mm^3. We can estimate the efficiency of detection from the opening angle of the detection system, considering that other effects on the efficiency like the quantum efficiency of the photo multiplier tube, etc. are negligible. With a focal length of 0.4 m and an aperture diameter of 6 cm, about 0.1% of the total radiation is detected. If we consider detection of the Balmer α line, then the detection limit is

$$\beta > \frac{5 \cdot 10^{-6}}{\sqrt{t}} . \tag{13}$$

Detection on the other Balmer spectral lines used in the experiments in this paper leads to a slightly higher detection limit, up to a factor of 2.5 higher for detection on the Balmer δ line.

Another limitation in the applicability of the technique is that the electron beam scatters too much and diffuses to a wide beam at too high particle densities. For a pure hydrogen plasma the limit is just above 1 mbar. For plasmas of hydrogen mixed with other gasses the limit on the pressure and plasma contents depends strongly on the cross-sections of the particles in the plasma for scattering with electrons from the electron gun. In the case of an Ar/H_2 plasma of 0.2 mbar the measurement error in the degree of dissociation is 35% when the Ar/H_2 ratio is 4/3. Extrapolation of the cross-section data for scattering of electrons with Ar atoms in [14] gives a cross-section for 20 keV electrons of about $4 \cdot 10^{-22}$ m^2, which with a partial Ar pressure of 0.1 mbar leads to a mean free path of 1 m. The distance between the electron gun and the centre of the plasma chamber is 0.4 m.

4. Results and discussion

In the case of 0.20 mbar H_2 and detection of the Balmer α line, the read-out from the lock-in amplifier is $\hat{S}^{plasma}_{\alpha,beam}$ = 168±2 mV when the plasma is on and $\hat{S}^{gas}_{\alpha,beam}$ = 224±3 mV when the plasma is switched off. Note that the signal with the plasma on is lower than with the plasma off, while in the latter case there is no atomic hydrogen that can be excited. However, this is more than compensated for by an increase in dissociative excitation because the molecular hydrogen density is higher due to the lower temperature when the plasma is off. This provides an example for the fact that the difference in particle density really should be corrected for. With 0.35 slm He added in the reactor, the read-out from the lock-in amplifier is $\hat{S}^{plasma}_{He,beam}$ = 140±1 mV when the plasma is on and $\hat{S}^{gas}_{He,beam}$ = 336±2 mV when the plasma is switched off. This leads to a particle density ratio n^{gas}/n^{plasma} of 2.40±0.01. If we assume a gas temperature of 293 K when the plasma is switched off, then with the ideal gas law the heavy particle temperature in the plasma following from this density is equal to 701±10 K. With equation 8 the dissociation degree equals (7±1)%, from which it follows that the atomic hydrogen density equals $(1.3\pm0.2)\cdot10^{20}$ m^{-3}. Without a correction for re-absorption the degree of dissociation becomes (12±1)% and the H density $(2.6\pm0.2)\cdot10^{20}$ m^{-3}.

Figure 3 shows the measured degree of dissociation. The degree of dissociation varies from (1±0.2)% (H density $(2.0\pm0.4)\cdot10^{20}$ m^{-3}) to (7±1)% (H density $(1.3\pm0.2)\cdot10^{20}$ m^{-3}) as the reactor pressure is varied from 1.0 mbar to 0.2 mbar. On the x-axis we have the degree of dissociation as measured using the Balmer β line. On the y-axis we have the degree of dissociation as measured on the Balmer α, γ, and δ lines, not corrected for optical thickness. Also the degree of dissociation as measured from the Balmer α and β lines, corrected for optical thickness, is shown in figure 3. The x=y line symbolizes perfect agreement of the degree of dissociation as determined using the different spectral lines with the measurement of the degree of dissociation measured using the uncorrected Balmer β line fluorescence. Four observations can be made. First, the coincidence of the measurements using the Balmer β line with correction for optical thickness with the line x = y suggests that the correction for optical thickness does not affect the values for the degree of dissociation as determined from the uncorrected Balmer β line fluorescence. Apparently the plasma is optically thin for photons in the Lyman γ line (p = 4 to 1 transition). Degrees of dissociation measured on higher excited states (Balmer γ and δ) will therefore not need a correction either. Second, the correction for optical thickness turns out to be necessary for the measurements with the Balmer α line. The degrees of dissociation measured with the Balmer α line that are corrected for optical thickness also agree reasonably well with the measurements using the Balmer β line fluorescence. If the re-absorption correction is not carried out, the degrees of dissociation deviate substantially, showing that the Lyman β radiation has a mean free path shorter than the size of the detection volume. A third observation is that the degrees of dissociation as measured using the Balmer γ line also agrees with the Balmer β method. Fourth, the degrees of dissociation as

determined from the measurement using the Balmer δ line fluorescence is about a factor of 5 lower. This deviation can be explained by considering the optical decay rate. The thermal velocity (about 3 km/s at 500 K) multiplied by the lifetime of the p = 6 excited state (0.6 μs) is equal to about 2 mm, not too different from the size of the detection volume. In other words, the decay rate of this state prohibits a complete capture of all the radiation of this state, i.e. the radiative decay occurs partly outside the detection volume.

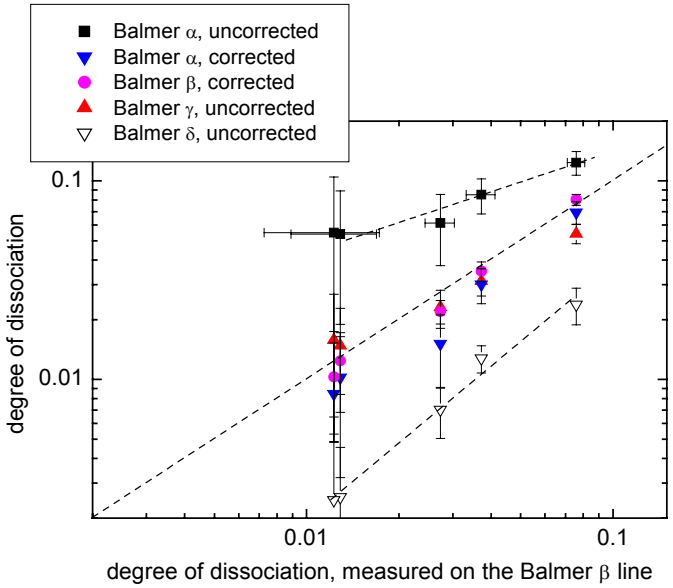

Figure 3. The degree of dissociation measured on different Balmer lines vs. the degree of dissociation measured on the Balmer β line. The line x=y denotes agreement between the measurements.

In addition to the pure hydrogen measurements the degree of dissociation for an Ar-H_2 mixture was measured too, to demonstrate the feasibility (2 slm Ar and 1.5 slm H_2): (17±6)% (H density $(8\pm3)\cdot10^{19}$ m^{-3}). Here the measurement accuracy is not very high because heavy atoms are added, leading to a blowing up of the radius of the beam as discussed above.

5. Conclusions

In this paper we have introduced EBIF as a new technique for the measurement of the degree of dissociation of hydrogen. The feasibility of an absolute measurement of the atomic hydrogen density in hydrogen containing plasmas is demonstrated. No additional calibration is needed. However, there are limitations on the plasma pressure for keeping the scattering of the electron beam within acceptable limits. Detection of

different lines of the fluorescence spectrum of the atomic hydrogen gives similar results, if the appropriate corrections are taken into account. This demonstrates the feasibility of the EBIF measurements.

Acknowledgements

The authors acknowledge the Charged Particle Optics group of the Delft University of Technology for supplying the electron gun. Ries van de Sande, Jo Jansen, Bertus Hüsken, and Herman de Jong are acknowledged for their technical support. The discussions in an initial phase of the project with Prof. Dr. H.F. Döbele (Univ. Essen) are gratefully acknowledged. This research was financially supported by NOVEM and STW.

Appendix A. Vector and matrix definitions

$\underline{n} = \begin{pmatrix} n_2 \\ n_3 \\ n_4 \\ \vdots \end{pmatrix}$ describes the occupation of the excited states.

$\underline{\underline{A}} = \begin{pmatrix} -A_{21} & A_{32} & A_{42} & \cdots \\ 0 & -\sum_{i=1}^{2} A_{3i} & A_{43} & \cdots \\ 0 & 0 & -\sum_{i=1}^{3} A_{4i} & \cdots \\ \vdots & \vdots & \vdots & \ddots \end{pmatrix}$ is the radiative decay matrix.

$$\underline{\underline{K}} = \begin{pmatrix} -\sum_{j=3}^{\infty} k_{2j} - k_{21} & k_{32} & k_{42} & \cdots \\ k_{23} & -\sum_{j=4}^{\infty} k_{3j} - \sum_{l=1}^{2} k_{3l} & k_{43} & \cdots \\ k_{24} & k_{34} & -\sum_{j=5}^{\infty} k_{4j} - \sum_{l=1}^{3} k_{4l} & \cdots \\ \vdots & \vdots & \vdots & \ddots \end{pmatrix}$$

is the collision (de-) excitation matrix. The cross-sections for de-excitation are above the diagonal and the cross-sections for excitations are below the diagonal.

$$\underline{\underline{K}}^{ion} = \begin{pmatrix} k_{2+} & 0 & 0 & \cdots \\ 0 & k_{3+} & 0 & \cdots \\ 0 & 0 & k_{4+} & \cdots \\ \vdots & \vdots & \vdots & \ddots \end{pmatrix}$$ is the matrix for ionisation by electron impact.

$$\underline{k}^{exc} = \begin{pmatrix} k_{12}^{exc} \\ k_{13}^{exc} \\ k_{14}^{exc} \\ \vdots \end{pmatrix}$$ are the coefficients for electron impact excitation from the ground state.

$$\underline{k}^{diss} = \begin{pmatrix} k_{2}^{diss} \\ k_{3}^{diss} \\ k_{4}^{diss} \\ \vdots \end{pmatrix}$$ is the vector for dissociative excitation by electron impact.

Appendix B. Numerical values of the decay rates and excitation cross-sections

The numbers for the radiative decay probabilities are calculated as described by van der Mullen in [12].

$$\underline{\underline{A}} = 10^8 \begin{pmatrix} -4.6990 & 0.4410 & 0.0842 & 0.0253 & 0.0097 & 0.0044 & 0.0022 & 0.0012 & 0.0007 & \cdots \\ 0 & -0.9986 & 0.0899 & 0.0220 & 0.0078 & 0.0034 & 0.0017 & 0.0009 & 0.0005 & \cdots \\ 0 & 0 & -0.3019 & 0.0270 & 0.0077 & 0.0030 & 0.0014 & 0.0007 & 0.0004 & \cdots \\ 0 & 0 & 0 & -0.1155 & 0.0102 & 0.0033 & 0.0014 & 0.0007 & 0.0004 & \cdots \\ 0 & 0 & 0 & 0 & -0.0519 & 0.0046 & 0.0016 & 0.0007 & 0.0004 & \cdots \\ 0 & 0 & 0 & 0 & 0 & -0.0262 & 0.0023 & 0.0008 & 0.0004 & \cdots \\ 0 & 0 & 0 & 0 & 0 & 0 & -0.0144 & 0.0012 & 0.0005 & \cdots \\ 0 & 0 & 0 & 0 & 0 & 0 & 0 & -0.0085 & 0.0007 & \cdots \\ 0 & 0 & 0 & 0 & 0 & 0 & 0 & 0 & -0.0052 & \cdots \\ \vdots & \vdots & \vdots & \vdots & \vdots & \vdots & \vdots & \vdots & \vdots & \ddots \end{pmatrix} [s^{-1}]$$

The coefficients for electron impact excitation/ionisation/dissociation given below are all calculated by multiplying the cross-section with the electron velocity (between round brackets). Two electron velocities should be accounted for: $8.4 \cdot 10^6$ m/s for the 20 keV electrons from the electron gun and $0.3 \cdot 10^6$ m/s for the electron energy in the plasma of about 0.2 eV.

Below are the coefficients for electron impact (de-)excitation: $\underline{\underline{K}}$ for collisions with plasma electrons and $\underline{\underline{K}}^{beam}$ for collisions with electrons from the electron gun. The excitation rate coefficients are calculated using the Born approximation, as, for example, explained by R.K. Janev et. al. [10]. The cross-sections for electron impact

de-excitation are satisfactory approximated by the area of a circle with a radius that is twice the excited electron orbital radius [12]. You can see that in the case of electrons in the plasma de-excitation is an important process, whereas for the high-energy electrons only excitation is important.

$$\underline{\underline{K}} = 10^{-15} \begin{pmatrix} -0.0006 & 0.0029 & 0.0090 & 0.0220 & 0.0456 & 0.0845 & 0.1441 & 0.2309 & 0.3519 & \cdots \\ 0 & -0.0058 & 0.0090 & 0.0220 & 0.0456 & 0.0845 & 0.1441 & 0.2309 & 0.3519 & \cdots \\ 0 & 0 & -0.2700 & 0.0220 & 0.0456 & 0.0845 & 0.1441 & 0.2309 & 0.3519 & \cdots \\ 0 & 0 & 0 & -0.1195 & 0.0456 & 0.0845 & 0.1441 & 0.2309 & 0.3519 & \cdots \\ 0 & 0 & 0 & 0.0315 & -0.3139 & 0.0845 & 0.1441 & 0.2309 & 0.3519 & \cdots \\ 0 & 0 & 0 & 0 & 0.0715 & -0.6800 & 0.1441 & 0.2309 & 0.3519 & \cdots \\ 0 & 0 & 0 & 0 & 0.0144 & 0.1430 & -1.3256 & 0.2309 & 0.3519 & \cdots \\ 0 & 0 & 0 & 0 & 0 & 0.0300 & 0.2604 & -2.2829 & 0.3519 & \cdots \\ 0 & 0 & 0 & 0 & 0 & 0.0121 & 0.0564 & 0.4389 & -3.1671 & \cdots \\ \vdots & \vdots & \vdots & \vdots & \vdots & \vdots & \vdots & \vdots & \vdots & \ddots \end{pmatrix} \cdot \left(0.3 \cdot 10^{6}\right) \left[m^{3} s^{-1}\right]$$

$$\underline{\underline{K}}^{beam} = 10^{-18} \begin{pmatrix} -0.0015 & 0.0000 & 0.0000 & 0.0000 & 0.0000 & 0.0000 & 0.0000 & 0.0000 & 0.0000 & \cdots \\ 0.0011 & -0.0066 & 0.0000 & 0.0000 & 0.0000 & 0.0000 & 0.0000 & 0.0000 & 0.0000 & \cdots \\ 0.0002 & 0.0044 & -0.0198 & 0.0000 & 0.0000 & 0.0000 & 0.0000 & 0.0000 & 0.0000 & \cdots \\ 0.0001 & 0.0006 & 0.0126 & -0.0472 & 0.0000 & 0.0000 & 0.0000 & 0.0000 & 0.0000 & \cdots \\ 0.0000 & 0.0002 & 0.0016 & 0.0286 & -0.0967 & 0.0000 & 0.0000 & 0.0000 & 0.0000 & \cdots \\ 0.0000 & 0.0001 & 0.0005 & 0.0035 & 0.0567 & -0.1773 & 0.0000 & 0.0000 & 0.0000 & \cdots \\ 0.0000 & 0.0001 & 0.0002 & 0.0011 & 0.0066 & 0.1017 & -0.2975 & 0.0000 & 0.0000 & \cdots \\ 0.0000 & 0.0000 & 0.0001 & 0.0005 & 0.0021 & 0.0114 & 0.1695 & -0.4504 & 0.0000 & \cdots \\ 0.0000 & 0.0000 & 0.0001 & 0.0003 & 0.0009 & 0.0035 & 0.0184 & 0.2668 & -0.2900 & \cdots \\ \vdots & \vdots & \vdots & \vdots & \vdots & \vdots & \vdots & \vdots & \vdots & \ddots \end{pmatrix} \cdot \left(8.4 \cdot 10^{7}\right) \left[m^{3} s^{-1}\right]$$

The electron impact ionisation cross-sections are calculated in [10]:

$$\underline{\underline{K}}^{ion} = 10^{-16} \begin{pmatrix} 0 & 0 & 0 & 0 & 0 & 0 & 0 & 0 & 0 & \cdots \\ 0 & 0 & 0 & 0 & 0 & 0 & 0 & 0 & 0 & \cdots \\ 0 & 0 & 0 & 0 & 0 & 0 & 0 & 0 & 0 & \cdots \\ 0 & 0 & 0 & 0 & 0 & 0 & 0 & 0 & 0 & \cdots \\ 0 & 0 & 0 & 0 & 0 & 0 & 0 & 0 & 0 & \cdots \\ 0 & 0 & 0 & 0 & 0 & 0 & 0 & 0 & 0 & \cdots \\ 0 & 0 & 0 & 0 & 0 & 0 & 0 & 0 & 0 & \cdots \\ 0 & 0 & 0 & 0 & 0 & 0 & 0 & 0.1858 & 0 & \cdots \\ 0 & 0 & 0 & 0 & 0 & 0 & 0 & 0 & 0.5058 & \cdots \\ \vdots & \vdots & \vdots & \vdots & \vdots & \vdots & \vdots & \vdots & \vdots & \ddots \end{pmatrix} \cdot \left(0.3 \cdot 10^{6}\right) \left[m^{3} s^{-1}\right]$$

$$\underline{\underline{K}}^{ion,beam} = 10^{-19} \begin{pmatrix} 0.0018 & 0 & 0 & 0 & 0 & 0 & 0 & 0 & 0 & \cdots \\ 0 & 0.0143 & 0 & 0 & 0 & 0 & 0 & 0 & 0 & \cdots \\ 0 & 0 & 0.0255 & 0 & 0 & 0 & 0 & 0 & 0 & \cdots \\ 0 & 0 & 0 & 0.0399 & 0 & 0 & 0 & 0 & 0 & \cdots \\ 0 & 0 & 0 & 0 & 0.0574 & 0 & 0 & 0 & 0 & \cdots \\ 0 & 0 & 0 & 0 & 0 & 0.0782 & 0 & 0 & 0 & \cdots \\ 0 & 0 & 0 & 0 & 0 & 0 & 0.1021 & 0 & 0 & \cdots \\ 0 & 0 & 0 & 0 & 0 & 0 & 0 & 0.1292 & 0 & \cdots \\ 0 & 0 & 0 & 0 & 0 & 0 & 0 & 0 & 0.1595 & \cdots \\ \vdots & \vdots & \vdots & \vdots & \vdots & \vdots & \vdots & \vdots & \vdots & \ddots \end{pmatrix} \cdot \left(8.4 \cdot 10^{7}\right) \left[m^{3} s^{-1}\right]$$

From [10] we took the formula for the calculation of the electron impact excitation from ground state. Möhlmann et al. [15] present an empirical formula for the

calculation of the cross-section for dissociative excitation by electron impact, which is used here to calculate the dissociative excitation coefficient:

$$\underline{k}^{exc,beam} = 10^{-21}\begin{pmatrix} 0.1033 \\ 0.0179 \\ 0.0063 \\ 0.0030 \\ 0.0017 \\ 0.0010 \\ 0.0007 \\ 0.0005 \\ 0.0003 \\ \vdots \end{pmatrix} \cdot \left(8.4 \cdot 10^7\right)\left[m^3 s^{-1}\right]; \quad \underline{k}^{diss,beam} = 10^{-21}\begin{pmatrix} 0.0326 \\ 0.0027 \\ 0.0006 \\ 0.0002 \\ 0.0001 \\ 0.0000 \\ 0.0000 \\ 0.0000 \\ 0.0000 \\ \vdots \end{pmatrix} \cdot \left(8.4 \cdot 10^7\right)\left[m^3 s^{-1}\right]$$

Appendix C. The degree of dissociation

We start with the mass balance for all excited states:

$$\frac{\partial n_p}{\partial t} + \nabla \cdot n_p \overline{w_p} = \left(\frac{\partial n_p}{\partial t}\right)_{CR}. \tag{C.1}$$

The first term of the left hand side represents the change in time of the density of particles in state p. The second term represents the transport of particles. The right hand side represents the production and loss of the excited state p due to electron-particle collisions and radiation. n_p is the occupation of the excited state p and $\overline{w_p}$ is the average velocity of an excited atom in state p. For the ground state atoms transport is important, especially in the case of a plasma that expands in a low-pressure reaction chamber. But these transport phenomena occur on a much larger time scale than the nanosecond time scale of the excitation and de-excitation processes in the plasma. Therefore we can neglect the transport of excited atoms. This results in the Quasi-Steady State Solution (QSSS):

$$\left(\frac{\partial n_p}{\partial t}\right)_{CR} = \left(\frac{\partial n_p}{\partial t}\right)_{population} - \left(\frac{\partial n_p}{\partial t}\right)_{depopulation} = 0. \tag{C.2}$$

Now we apply this balance to the hydrogen atom and we fill in the possible processes in a hydrogen plasma:

$$\underset{A}{n_1 n_e k_{1p}} + \underset{B}{\sum_{q\neq p} n_q n_e k_{qp}} - \underset{C}{\sum_{q\neq p} n_p n_e k_{pq}} + \underset{D}{\sum_{q>p} n_q A_{qp}} - \underset{E}{\sum_{q<p} n_p A_{pq}} \underset{F}{- n_p n_e k_p^{ion}} + \underset{G}{n_{H_2} n_e k_p^{diss}} + \underset{H}{P(p)} = 0 \tag{C.3}$$

where n_1 denotes ground state density, n_e is the electron density in the plasma, k is the (de-)excitation reaction coefficient for electron collision, and A_{qp} is the radiative decay

constant for the decay from state q to p. The physical processes that are represented by the expressions in equation C.3 are:

A: population of state p by electron impact excitation from the ground state
B: population of state p by (de-)excitation by electron impact from state q
C: depopulation of state p by (de-)excitation by electron impact to state q
D: population of state p by radiative decay from a higher state q (cascade radiation)
E: depopulation of state p by radiative decay to a lower state q (spontaneous emission)
F: depopulation of state p by electron impact ionisation
G: population of state p by H_2 dissociation by electron impact
H: population of state p by recombination processes, like three-particle recombination and dissociative recombination

Equation C.3 can also be written in matrix format:

$$\frac{d\underline{n}}{dt} = \left(\underline{\underline{A}} + n_e \underline{\underline{K}}\right)\cdot \underline{n} - n_e \underline{\underline{K}}^{ion} \cdot \underline{n} + n_1 n_e \underline{k}^{exc} + n_{H_2} n_e \underline{k}^{diss} + \underline{P} = 0 \qquad \text{(C.4)}$$

Now $\underline{\underline{A}}$ is the radiative decay matrix. Note that the indices in the previous variables A_{qp} (equation C.4) denote states and do not correspond with the index in the matrix $\underline{\underline{A}}$ (cf. Appendix A for the matrix definitions).
We can rewrite equation C.4 into

$$\underline{n} = -inv\left(\underline{\underline{A}} + \underline{\underline{K}} n_e + \underline{\underline{K}}^{beam} n_{e-beam} - \underline{\underline{K}}^{ion} n_e - \underline{\underline{K}}^{ion,beam} n_{e-beam}\right)\cdot \qquad \text{(C.5)}$$
$$\left(\underline{P} + \underline{k}^{diss} n_e n_{H_2}^{plasma} + \underline{k}^{diss,beam} n_{e-beam} n_{H_2}^{plasma} + n_1 n_e \underline{k}^{exc} + n_1 n_{e-beam} \underline{k}^{exc,beam}\right)$$

Some parts of this expression can be neglected. To compare the magnitude of the expressions that make up equation C.1 we use the numbers in Appendix B and we estimate that the electron density in the plasma n_e will be about 10^{17} m^{-3}, and the electron density in the 1 mA, 20 keV, 2 mm diameter electron beam $n_{e,beam}$ is $1.9 \cdot 10^{13}$ m^{-3}.

Case plasma on and electron beam on
First we compare the matrices that are written between the first brackets. If we multiply the value for $n_{e,beam}$ given above with the matrix $\underline{\underline{K}}^{beam}$ we see that all values are at least a factor 1000 smaller than the values in matrix $\underline{\underline{A}}$. So this can be neglected. This also counts for $n_{e,beam}\underline{\underline{K}}^{ion,beam}$. Also $n_e\underline{\underline{K}}^{ion}$ can be neglected except for $p = 9$ and $p = 10$. $n_e\underline{\underline{K}}$ can be neglected for the states up to $p = 5$, for $p = 6$ the contributions are about equal and for the higher states de-excitation by electron impact is more important than radiative decay. Still we will neglect this expression, because we will only consider the lower states in this research. The only part left in the expression between the first brackets in equation C.1 is $\underline{\underline{A}}$. The energy of the electrons in the plasma is too low (± 0.2 eV) to dissociate H_2 (19 eV) or to excite ground state H atoms (10.2 eV), so in the

expression between the second brackets the parts $\underline{k}^{diss} n_e n_{H_2}^{plasma}$ and $n_1 n_e \underline{k}^{exc}$ disappear.

Case plasma off and/or electron beam off
For the case plasma off $n_1=0$ in equation C.5 because no atomic hydrogen is generated by the plasma, and for the case electron beam off of course $n_{e\text{-}beam}=0$ in equation C.5.

Three-particle recombination
Now we only have to prove that the electron beam does not influence $\underline{P}$, because that would simplify the subtraction in the numerator of τ in equation 2. Three-particle recombination with an electron from the electron beam would be one of the candidates.
The reaction rate is $n_+ n_e n_{e,beam} \underline{k}^{3particle}$ with $\underline{k}^{3particle} = 1.7 \cdot 10^{-39} E_e^{-\frac{9}{2}} \left[m^6 / s\right]$ and with E_e=20 keV. The second candidate is radiative recombination for which the rate is given by $n_+ n_{e\text{-}beam} k_{rad.rec.}$ with $k_{rad.rec.} \approx 10^{-19} E_e^{-0.2}$[m^3/s].
Filling in the appropriate numbers (for the ion density n_+ we fill in the plasma electron density) shows that these rates are negligible in comparison with $\underline{k}^{diss,beam} n_{e-beam} n_{H_2}^{plasma}$ and $n_1 n_{e\text{-}beam} k^{exc,beam}$.
Starting with equation C.5 all considerations above lead to the formulas as described in table 1.

Appendix D. Re-absorption correction

In general, the radiative decay matrix can be corrected for re-absorption by means of an escape factor. Imagine a volume of size R from which the radiation escapes. The escape factor then is given by

$$\Lambda_{p,q=1} = 0.65 \left(\frac{g(p)}{g(1)} \frac{n_1 \lambda^2 A(p,1) R}{8\pi^{3/2} \Delta\nu_D} \right)^{-\frac{1}{2}} \tag{D.1}$$

with $g(p)=2p^2$ is the statistical weight of state p,
n_1 is the ground state density,
c is the speed of light,
λ is the wavelength of the detected transition, and
$\Delta\nu_D = \frac{c}{\lambda_0} \sqrt{\frac{8kT_h}{m_h c^2}}$ is the Doppler broadening with T_h and m_h being the temperature and the mass, respectively, of the atomic hydrogen.
Now the radiative decay matrix is corrected for re-absorption with the escape factor in the following way:

$$\underline{\underline{A}}_{corr} = \begin{pmatrix} -\Lambda_{21}A_{21} & A_{32} & A_{42} & \cdots \\ 0 & -\Lambda_{31}A_{31} - A_{32} & A_{43} & \cdots \\ 0 & 0 & -\Lambda_{41}A_{41} - \sum_{i=2}^{3} A_{4i} & \cdots \\ \vdots & \vdots & \vdots & \ddots \end{pmatrix}$$

References

[1] M.C.M. van de Sanden, R.J. Severens, W.M.M. Kessels, R.F.G. Meulenbroeks, and D.C. Schram, J. Appl. Phys. **84**, 2426 (1998).

[2] M. Heintze, R. Zedlitz, and W. Westlake, Mat. Res. Soc. Proc. **358**, 733 (1995).

[3] S. Takashima, M. Hori, T. Goto, A. Kono, M. Ito, and K. Yoneda, Appl. Phys. Lett. **75**, 3929 (1999).

[4] P. Vankan, S.B.S. Heil, S. Mazouffre, R. Engeln, D.C. Schram, H.F. Döbele, Rev. Sci. Instrum. **75**, 996 (2004).

[5] M.G.H. Boogaarts, S. Mazouffre, G.J. Brinkman, H.W.P. van der Heijden, P. Vankan, J.A.M. van der Mullen, D.C. Schram, and H.F. Döbele, Rev. Sci. Instr. **73**, 73 (2002).

[6] B.L. Preppernau and T.A. Miller, J. Vac. Sci. Technol. A **8**, 1673 (1990)

[7] V.N. Ochkin, S.Y. Savinov, S.N. Tskhai, U. Czarnetzki, V. Schulz-von der Gathen, and H.F. Döbele, IEEE Trans. Plasma Sci. **26** (1998).

[8] M.J. De Graaf, PhD thesis, Eindhoven, 1994.

[9] S.Ya. Khmel' and R.G. Sharafutdinov, Techn. Phys. **42**, 291 (1997).

[10] R.K. Janev, W.D. Langer, Jr, and D.E. Post, Jr., "Elementary processes in Hydrogen-Helium Plasmas", Springer Verlag (1985).

[11] S. Mazouffre, M.G.H. Boogaarts, J.A.M. van de Mullen, and D.C. Schram, Phys. Rev. Lett. **84**, 2622 (2000).

[12] J.A.M. van der Mullen, Phys. Rep. **191**, 109 (1990).

[13] G.M.W. Kroesen. D.C. Schram, and J.C.M. de Haas, Plasma Chem. Plasma Process. **10**, 551 (1990).

[14] http://www.siglo-kinema.com/database/xsect/ar_xsect.gif

[15] G.R. Möhlmann, F.J. de Heer, and J. Los, Chem. Phys. **25**, 103 (1977).

Chapter 4

Determining the material structure of microcrystalline silicon from Raman spectra

C. Smit[1,2], R.A.C.M.M. van Swaaij[2], H. Donker[3], A.M.H.N. Petit[2], W.M.M. Kessels[1], and M.C.M. van de Sanden[1]

[1] *Eindhoven University of Technology, Department of Applied Physics, P.O. Box 513, 5600 MB Eindhoven, the Netherlands*
[2] *Delft University of Technology, DIMES-ECTM, P.O. Box 5053, 2600 GB Delft, the Netherlands*
[3] *Delft University of Technology, Laboratory for Inorganic Chemistry, Julianalaan 136, 2628 BL Delft, the Netherlands*

J. Appl. Phys. **94**, 3582 (2003)

Abstract

An easy and reliable method to extract the crystalline fractions in microcrystalline films is proposed. The method is shown to overcome in a natural way the inconsistencies that arise from the regular peak fitting routines. We subtract a scaled Raman spectrum that was obtained of an amorphous silicon film from the Raman spectrum of the microcrystalline silicon film. This subtraction leaves us with the Raman spectrum of the crystalline part of the microcrystalline film and the crystalline fraction can be determined. We apply this method to a series of samples covering the transition regime from amorphous to microcrystalline silicon. The crystalline fractions show good agreement with x-ray diffraction (XRD) results, in contrast to crystalline fractions obtained by the fitting of Gaussian line profiles applied to the same Raman spectra. The spectral line shape of the crystalline contribution to the Raman spectrum shows a clear asymmetry, an observation in agreement with model calculations reported previously. The varying width of this asymmetrical peak is shown to correlate with the mean crystallite size as determined from XRD spectra.

1. Introduction

Hydrogenated amorphous silicon (*a*-Si:H) has been studied for application in solar cells for several decades. Nowadays, microcrystalline silicon (*μc*-Si:H) also receives much attention because it is a suitable material for application as the intrinsic layer in the bottom cell of thin-film tandem solar cells. To study the material properties, the complete set of analysis techniques used in *a*-Si:H research (reflection/transmission spectroscopy, sub gap absorption, dark and photoconductivity, etc) can be copied, although carefully [1]. In addition, the study of this material should also include the determination of the crystalline fraction, because *μc*-Si:H is a heterogeneous material and consists of crystalline and amorphous regions. The fraction of crystalline material, the crystallite size, and the grain boundaries have an important influence on the optical and electrical properties that are relevant for application in solar cells. Void and grain boundaries, for example, could contain a high density of recombination centres, whereas a high crystalline fraction is likely to increase the mobility of the charge carriers.

Four techniques are commonly used to analyse the structural properties of *μc*-Si:H: high-resolution transmission electron microscopy (HRTEM), x-ray diffraction (XRD), spectroscopic ellipsometry (SE), and Raman spectroscopy. However, none of these techniques leads to an unambiguous determination of the crystalline fraction in *μc*-Si:H films. First, HRTEM is a complicated technique and its respective images have a poor contrast on amorphous material, so regions where amorphous and crystalline material overlap in the sample will appear to be fully crystalline in the two dimensional image. Therefore it is difficult to determine the crystalline fraction in microcrystalline material from these images, unless the crystalline fraction is so small (smaller than a few percent) that the crystals do not overlap in the image. Particle sizes, though, can be extracted. Second, XRD is an easier technique, but a reasonable scan takes at least two hours for films of about 500 nm thick. Also it is not straightforward to extract the crystalline fraction, although some researchers reported doing so [2,3]. The average particle size can be extracted from the XRD peak widths. Third, SE is a simple and easy measurement technique. It gives the dielectrical constant as a function of energy, which is fitted with a model containing parameters like film thickness and crystalline and void fractions [4]. However, it is not unambiguous as to which model is accurate and realistic.

A fourth technique to analyse the structural properties is Raman spectroscopy. Most methods used in literature to obtain crystalline fractions from Raman spectra are based on peak fitting and suffer from interpretation problems. For example, often three peaks instead of two (one for the crystalline and one for amorphous part) are necessary to fit the experimental data. The need for three peaks is often explained by introducing an extra phase in the material. Furthermore, the crystalline fractions that result from peak fitting are very sensitive to the choice of input parameters like whether peak positions are allowed to vary and the range of data points that is included in the fitting procedure.

In this article we will first review reported methods to obtain information on the material structure from Raman spectra. Then we propose an alternative approach to

separate the amorphous and the crystalline contributions to the Raman spectrum of the microcrystalline silicon film that is to be examined. This method is applied to a series of silicon films that covers the transition from amorphous to microcrystalline. We will show that this technique automatically resolves several problems related to the methods used in literature. Finally, we shall compare crystalline fractions obtained with this method with results form XRD analysis and Gaussian line profile fitting procedures on the same samples and present our conclusions.

2. The Raman spectrum of microcrystalline silicon

2.1. The Raman spectrum

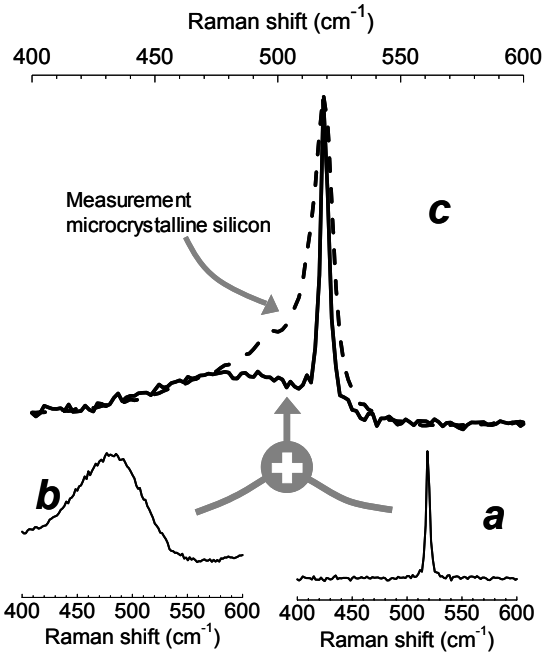

Figure 1. (a) Raman spectrum of monocrystalline silicon. (b) Raman spectrum of *a*-Si:H. (c) Summation of (a) and (b) (solid line), scaled before summation by the eye so that the peak and the 'bump' in (c) fit the peak and the 'tail' of the Raman spectrum of μc-Si:H (dahed line).

In a solid a small part of the energy of an incoming photon can be used to excite a lattice vibration (phonon). The remaining energy escapes as a photon with a slightly smaller energy compared to the incoming photon. This energy shift is denoted as Raman shift. In a crystalline solid the momentum conservation law selects only phonons with zero momentum, because the momentum of the photon is negligibly small. In monocrystalline silicon only the optical phonon with energy 64 meV has zero

momentum and this leads to the sharp peak at a Raman shift of 520 cm^{-1} (figure 1a). In *a*-Si:H the momentum selection rule is relaxed and a variety of phonon modes and energies are allowed [5]. A broad peak centred at 480 cm^{-1} now dominates the Raman spectrum (figure 1b). *μc*-Si:H can be considered as a mix of crystalline Si (*c*-Si) and *a*-Si:H. The Raman spectrum, however, is not simply the sum of a monocrystalline silicon and an amorphous silicon spectrum, as can be seen in figure 1c. This is due to the fact that the Raman spectrum of a small crystallite is different from a Raman spectrum of monocrystalline silicon. It is not straightforward how to determine which part of the spectrum is due to the crystalline fraction and which part can be attributed to the amorphous fraction in *μc*-Si:H. This determination is necessary, though, in order to extract the crystalline fraction from Raman spectra.

2.2. Ways to get the material structure from Raman spectroscopy

We will first shortly review several techniques that have been reported to separate the Raman spectra into a crystalline and an amorphous contribution. The simplest way is just to compare the peak height at 520 cm^{-1} to the peak height at 480 cm^{-1} (e.g., see reference 6). This comparison gives only a very rough estimate of the crystallinity of the material. Peak fitting is more frequently used to unravel the spectrum. For example, two peaks (Gaussian or Lorentzian line profiles) can be used, one to describe the crystalline part and one for the amorphous part, but this procedure does not lead to a good fit to the measured Raman spectrum. Furthermore, the low energy peak, which is attributed to the amorphous fraction, tends to shift to higher energies then the expected 480 cm^{-1}. As we will show later, this shift is not due to a shift of the amorphous transverse optical (TO) phonon energy, but to the change in the Raman peak shape of the crystalline fraction. In order to obtain a good fit to the measured spectra at least three peaks are necessary [2,7]. The third peak is then attributed to surface modes [7] or to hexagonal ordered silicon [2].

The peak fitting routines described herein require this extra peak because the peak shape of the crystalline part is asymmetric and varies for different samples. As calculated by Richter *et al.* [5] and Campbell *et al.* [8] the crystalline peak width and position is influenced by the crystallite size and shape. For example, calculations show that this peak becomes more and more asymmetric for smaller crystallite sizes. Touir *et al.* [9] account for this by using two asymmetrical Lorentzian line profiles to obtain a good fit to their spectra. They find peaks around 500 cm^{-1} and 520 cm^{-1} (and so do we with our samples as we will show in Sec. 4.4), which they attribute to two distinct crystallite sizes. However, the idea of two crystallite sizes is not attractive, because a continuous distribution of sizes seems more likely. Furthermore, only the TO phonon mode of *a*-Si:H is included in the fitting procedures mentioned herein, while the amorphous longitudinal optical (LO) phonon mode, and maybe even the Si-H wagging mode at 660 cm^{-1} and the transverse acoustic (TA) phonon mode of the amorphous fraction, have an influence on the microcrystalline Raman spectrum in the energy region of the crystalline feature (around 520 cm^{-1}). In addition, the amorphous peak in the Raman spectrum of *μc*-Si:H has been reported to shift to higher energy with increasing crystalline fraction. This shift is attributed to an extra TO band at about 490

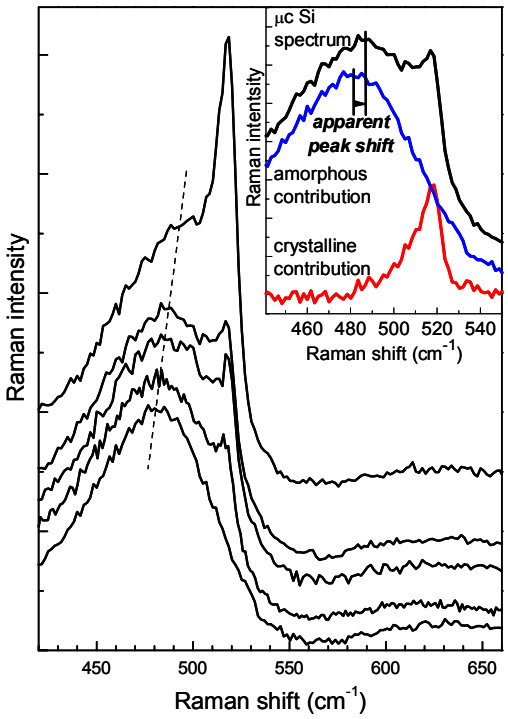

Figure 2. The amorphous peak of the Raman spectrum of *μc*-Si:H seems to shift to higher energies with increasing crystalline fraction. Inset: the amorphous contribution plus the crystalline contribution make the microcrystalline spectrum. The addition of the sloped shoulder of the crystalline contribution seems to shift the maximum in the spectrum of the amorphous sample to a higher energy in the spectrum of the microcrystalline sample. This shift could abusively be interpreted as a shift of the amorphous TO phonon energy.

cm^{-1}, indicating a secondary phase in the amorphous material [10]. We also observe this apparent peak shift (figure 2).

In contrast to the Raman signal of the small crystallites in *μc*-Si:H, the Raman signal of *a*-Si:H is shown to vary only slightly between different samples. Spectra taken from some of our own amorphous samples deposited under different processing conditions show no significant differences for the range investigated (figure 3). In line with this result Ishidate *et al.* [11] found TO phonon energy shifts of only a few cm^{-1} and peak width variations of a few percent at most when the hydrogen content is varied from 6 to 18 at. %. This strongly suggests that the Raman spectrum of the amorphous fraction in *μc*-Si:H can be represented by the Raman spectrum of *a*-Si:H. Therefore it must be possible just to subtract the amorphous contribution to the Raman spectrum of *μc*-Si:H with the help of a Raman spectrum of an amorphous film. The advantage is that in the unravelling of the Raman spectrum of *μc*-Si:H not only the TO phonon mode of the amorphous component is taken into account but also the other phonon modes. After the subtraction, changes in the peak shape of the crystalline contribution

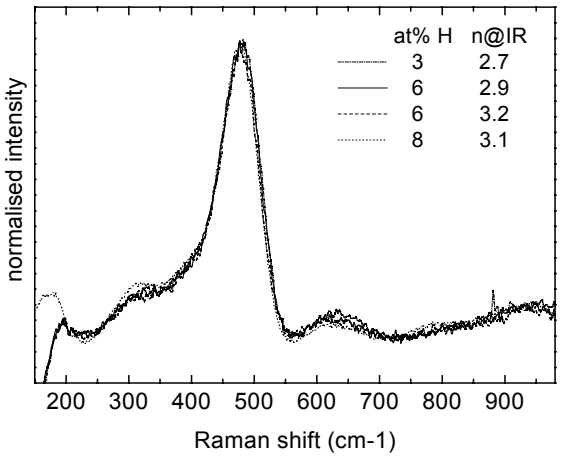

Figure 3. Raman spectra of four a-Si:H films with varying refractive index and hydrogen content.

to the Raman spectrum of *μc*-Si:H become clearly visible. The apparent peak shift shown in figure 2 can now be explained in a natural way as illustrated in the inset of figure 2: when the TO phonon peak in the Raman spectrum of an *a*-Si:H film is added to the asymmetrical, sloped shoulder of the Raman peak of the crystalline fraction in *μc*-Si:H, then the position of the peak in the resulting line shape is expected to shift.

3. Experiment

We deposited two series of silicon films of about 600 nm thick on Corning glass C1737 and [111] oriented, slightly *n*-type *c*-Si substrates simultaneously, using expanding thermal plasma chemical vapour deposition [12]. Details on the deposition set-up are reported elsewhere [13]. The first series of samples is deposited using an Ar flow of 1200 sccm, a H_2 flow of 600 sccm, and a varying SiH_4 flow from 0.5 to 10 sccm. The second series is deposited using a constant SiH_4 flow of 5 sccm and a varying hydrogen flow. The argon flow was set at twice the hydrogen flow. A third series of samples is deposited using a pure H_2 plasma with a H_2 flow of 2000 sccm and a varying SiH_4 flow on glass and Al foil and the films are about 5000 nm thick.

The Raman spectra of the silicon films on the glass substrates are measured using a Raman microscope (Renishaw (Gloucestershire, UK) Ramascope system 2000, grating 1800 lines/mm) in a backscattering geometry with a 2 mW Ar laser at a wavelength of 514.5 nm focussed in a spot of about 1 μm. On the samples on *c*-Si substrates of the first sample series XRD measurements are carried out (Bruker-Nonius (Delft, The Netherlands) D5005 θ/θ diffractometer with diffracted beam graphite monochromator, wavelength Cu α). On the third sample series with Al substrates also XRD measurements are carried out to determine the crystalline fraction.

4. Results and discussion

4.1. Splitting a Raman spectrum into a crystalline and an amorphous contribution

In order to split the Raman spectrum of a *μc*-Si:H film into a crystalline and an amorphous contribution we subtract a scaled Raman spectrum of an *a*-Si:H film (figure 4). The result is denoted as μc-Si – A × a-Si:H – B, where B is a flat background to correct for the dark counts and background light. Because of differences in signal strength (caused by differences in sample alignment and film composition) the amorphous spectrum is scaled by a factor A before subtraction. The values for this constant and background are obtained in a least squares routine, realizing that the crystalline contribution to the spectrum of *μc*-Si:H cannot contain peaks at the amorphous acoustical phonon energies. That means that the residue in the regions in the spectrum outside the TO phonon peak (we take the region 200 cm^{-1} to 440 cm^{-1} and 560 cm^{-1} to 850 cm^{-1}) should be minimised.

The resulting crystalline part of the spectrum shows a flat background, as can be seen in figure 4. The features at the low-energy side of the TO crystalline peak at 520 cm^{-1} in the amorphous and in the microcrystalline spectra (in the energy range of 150 cm^{-1} to 480 cm^{-1}) that are attributed to the LA, TA, and LO amorphous phonon modes are absent. Moreover, the broad features at the high-energy side in the amorphous and microcrystalline spectra at about 650 cm^{-1} and 950 cm^{-1}, which are attributed to two-phonon excitations in *a*-Si:H and to the Si-H wagging mode, are also subtracted correctly. The only feature that remains is a bump at 960 cm^{-1}. This feature is due to

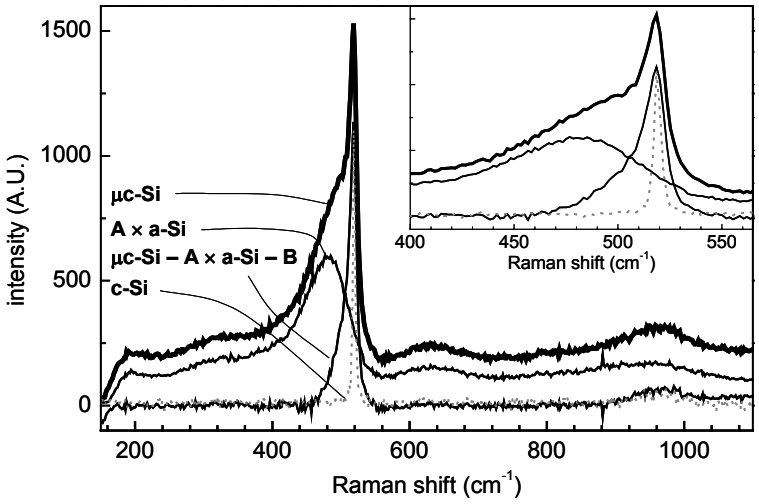

Figure 4. From a Raman spectrum of mc-Si:H (thick line) a Raman spectrum of *a*-Si:H (thin line) is subtracted to obtain the contribution of the crystalline fraction. The scaling factor for the amorphous contribution and the flat background are obtained in a least-squares procedure. For comparison the Raman spectrum of monocrystalline silicon is shown also (dashed line). The inset contains a magnification of the TO phonon peak region.

the two-phonon excitation process in *c*-Si (it can also be noticed in the Raman spectrum of monocrystalline silicon in figure 4) and should therefore be present in the Raman spectrum of the crystalline fraction. These observations strongly suggest that the procedure followed splits the Raman spectrum of μc-Si:H into the amorphous and the crystalline contributions. The small, uncorrelated residue that is obtained after the subtraction is strong evidence for the assumption that the shape of the Raman spectrum of *a*-Si:H used in this procedure is the same as the shape of the Raman spectrum of the amorphous fraction in μc-Si:H.

4.2. Raman spectrum of the crystalline fraction

In figure 5 the XRD measurements of the first sample series (see Sec. **3**) are presented and it can be concluded that the samples deposited with SiH_4 flows from 0.5 to 5 sccm contain a crystalline fraction and the sample deposited with a SiH_4 flow of 10 sccm does not. The Raman spectra of the silicon films are split into an amorphous and a crystalline contribution following the procedure just described. The crystalline part of the Raman spectra is shown in figure 6. The spectra are normalised to the maximum of the Raman peak. For comparison the Raman spectrum of *c*-Si is also shown in figure 6. Clearly, the peak of the crystalline fraction in μc-Si:H is broader than the monocrystalline peak. It also clearly shows an asymmetry. Richter *et al.* [5] calculated the Raman spectrum of a finite sized spherical silicon crystal and found a similar asymmetry. With smaller particle size, the momentum selection rule of the Raman process is more relaxed. With increasing momentum the TO phonon energy becomes lower, so when a momentum greater then zero is allowed, lower-energy phonons will be excited. This leads to a broadening of the Raman peak towards the low-energy side, resulting in an asymmetrical peak shape.

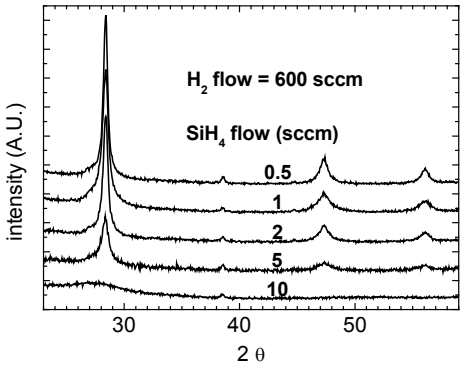

Figure 5. XRD measurements of a series of samples deposited using a varying SiH_4 flow. Samples deposited using a SiH_4 flow up to 5 sccm show crystallinity.

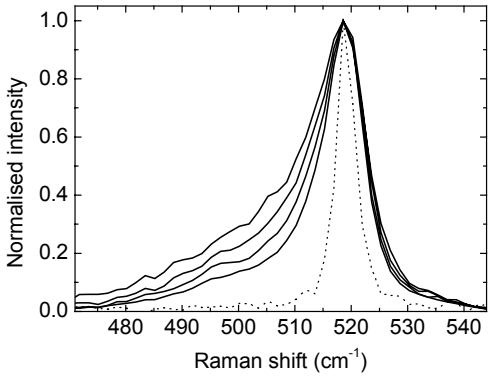

Figure 6. The contributions of the crystalline fraction to the microcrystalline Raman spectrum normalised to one. Going from the narrow to the wide peak the corresponding films are deposited using a SiH_4 flow of 0.5, 1, 2, and 5 sccm. The dashed line is the Raman spectrum of monocrystalline silicon.

The calculations of Richter *et al*. [5] explain the asymmetry, and revealed that the broadening depends on crystallite size. Figure 6 shows that the broadening increases with increasing silane flow. The average particle size is determined from the XRD measurements by applying the Scherrer equation to the integral width of the peak that corresponds to the reflection on the [220] lattice planes [14]. In figure 7 the average particle size is plotted against the full width of the Raman peak at half maximum, which shows a clear correlation. These data are in close agreement with measurements by Iqbal *et al.* [7, 15], although they use the full width half maximum (FWHM) of a fitted symmetrical Lorentzian line shape. Calculations of Campbell *et al.* [8] show a similar trend. It should be realized that the calculations concern Raman scattering on a ball shaped particle having a specific size, while a distribution of particle sizes, maybe with different shapes, contributes to the experimental data. Also calculated data of Richter *et al.* [5] are shown, but they show a large deviation from the other data in figure 7.

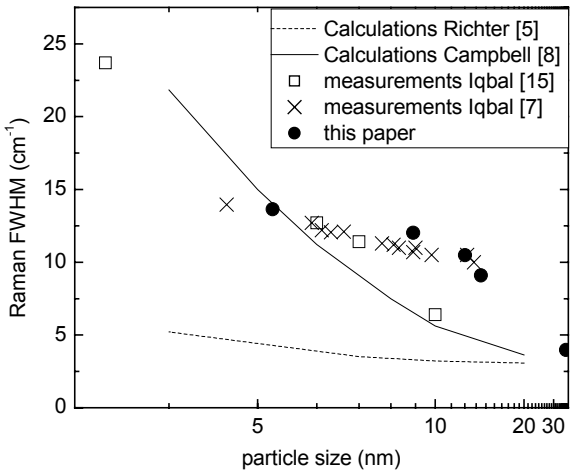

Figure 7. The FWHM of the curves in figure 6 is displayed versus the average particle size as obtained from XRD measurements. Also other reported data, experimental as well as calculated, are presented for comparison. The data point completely on the right-hand side of the reciprocal x-axis is measured on an "infinitely" large c-Si wafer.

4.3. Determining the crystalline fraction

The peak areas of the crystalline and the amorphous parts of the Raman spectra correlate to the amount of *c*-Si and *a*-Si:H in the film. It is not possible to obtain absolute values because the detection efficiency is usually not known. The ratio of the two peak areas, however, corresponds to the ratio of the amount of crystalline to the amount of amorphous silicon. This ratio needs to be corrected for the difference in the cross-sections for phonon excitation of *c*-Si compared to that of *a*-Si:H. For the TO phonon the ratio of these two cross-sections ($\sigma_{c\text{-}Si}/\sigma_{a\text{-}Si:H}$) is usually set at 0.8 [16,17]. It

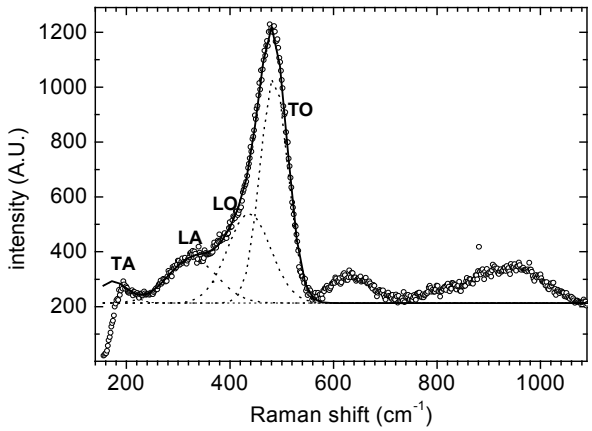

Figure 8. Four Gaussian line profiles (dashed lines) are fitted to a Raman spectrum of *a*-Si:H to obtain the contribution of the TA, LA, LO, and TO phonon modes. The peak area of the TO phonon is used in the calculation of the fraction in the microcrystalline films.

should be noted that this cross-section ratio is reported to depend on the crystallite size, and varies from about 0.9 to about 0.7 as the crystallite size ranges from 5 to 15 nm [18], which are typical sizes for our samples. Now we have to determine which part of the amorphous spectrum that is subtracted is due to the TO phonon excitation. In figure 8 the contributions of the four phonon modes are fitted to the amorphous spectrum using four Gaussian line profiles and the peak area of the TO phonon Raman scattering is determined. This number is multiplied by 0.8 to account for the cross-section ratio and then multiplied by the scaling factor that is found from the least-squares procedure described herein to account for the amount of amorphous silicon in the microcrystalline film. The crystalline contribution is obtained by integrating the crystalline peak from 440 cm^{-1} to 560 cm^{-1}. Following this procedure the crystalline fractions were extracted from the Raman spectra of the samples of the second sample series. The result is shown in figure 9. At a SiH_4 dilution in H_2 of about 1% the material changes from

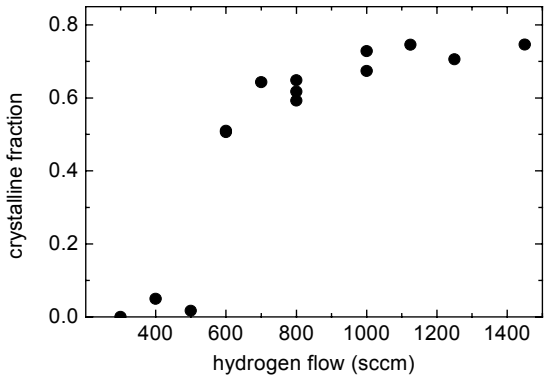

Figure 9. The crystalline fraction versus the hydrogen flow used during deposition.

amorphous to microcrystalline. It can be noticed that the crystalline fraction saturates at a value a little below 0.8. This might be due to the grain boundaries, which can be considered as disordered material. However, it is reported that in fully nanocrystallised (free of amorphous material) silicon films (crystallite size around 5 nm) the amorphous Raman signal relative to the integral Raman signal from 440 cm^{-1} to 550 cm^{-1} amounts less than 0.1 [19]. This indicates that grain boundaries not necessarily result in a saturation of the crystalline fraction at 0.8. It is therefore very well possible that a minimum of 10 to 20% of amorphous material is characteristic for the deposition conditions used in this article.

4.4. Comparison with other techniques

Table 1. Crystalline fraction (%) determined from XRD and from Raman spectra using different techniques. The crystalline fractions determined from the Raman spectra are calculated using [cryst]/([cryst] + 0.8*[am]). First column: Silane flow. Second column: Crystalline fractions from XRD. Third column: Crystalline fraction determined as described in this article. Fourth column: For [cryst] and [am], the Raman intensities at 520 cm^{-1} and 480 cm^{-1}, respectively, are taken. Fifth column: Fitting of three Gaussian line profiles as described in Refs. 2 and 20. Sixth column: Fitting of five Gaussian line profiles as described in Refs. 10 and 21. From a sample deposited with a silane flow of 18 sccm, no crystalline fraction was detected with all techniques.

SiH_4 flow (sccm)	XRD[a]	Raman this paper	Raman [520] versus [480][b]	Raman 3 Gauss	Raman 5 Gauss
10	58±9	52±4	72±4	46±10	38±6
14	50±6	46±4	69±3	40±17	31±6
16	12±2	11±4	46±2	3±1.5	5.3±2.5

Note: cryst indicates crystalline and am indicates amorphous
[a]see reference 3.
[b]see reference 6.

To validate the method described herein to obtain crystalline fractions the crystalline fractions of the third series of samples (see Sec. **3**) are determined from XRD measurements, using the method described by Williamson [3]. Furthermore, to compare our method with methods based on peak fitting we also determined the crystalline fractions of these samples from the Raman spectra using techniques that are presented in literature. The results are shown in table 1. In the second column the crystalline fractions calculated from XRD measurements are shown. The third column contains the crystalline fractions determined from Raman spectra using the method presented in this article. In the fourth column only the signal intensities at 480 cm^{-1} and 520 cm^{-1} are taken for the amorphous and the crystalline fraction respectively; a method used for example in reference 6. In the following column the result from fitting three Gaussian line profiles is shown (fitting procedure is copied from reference 2) [20], followed by a fit procedure (copied from reference 10) using five Gaussian line profiles [21]. In figure 10 some of the fits are shown. figure 10(a) and 10(b) show fits of three and five Gaussian line profiles respectively. The asymmetrical peak of the

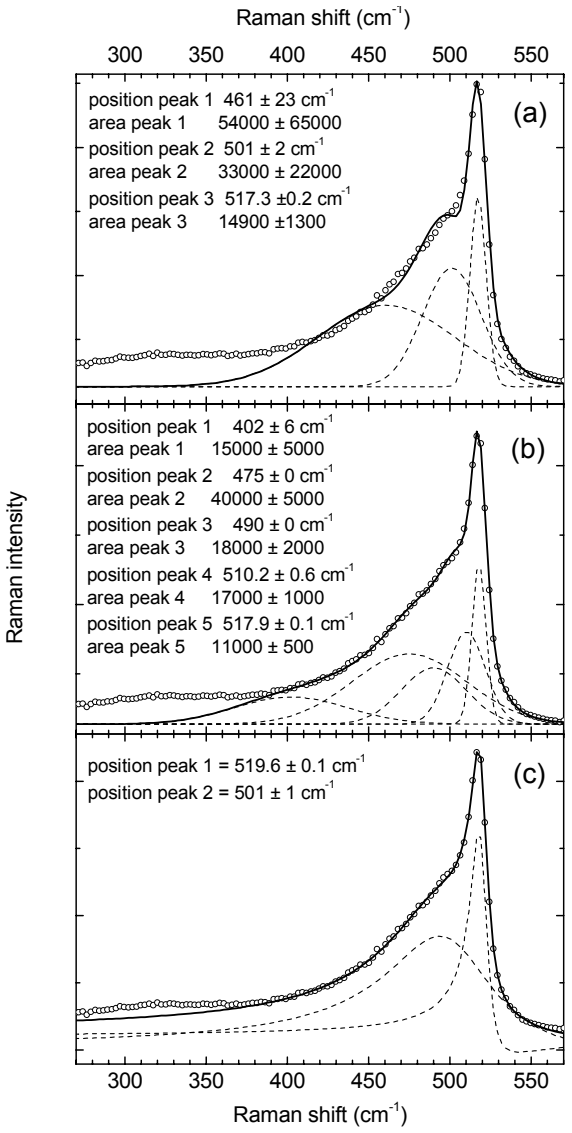

Figure 10. Several fitting techniques that are described in literature, applied to a typical Raman spectrum of microcrystalline silicon. (a) Three Gaussian line profiles (see Refs. 2 and 20), (b) Five Gaussian line profiles (see Refs. 10 and 21), and (c) Two asymmetrical Lorentzian line profiles (see reference 9).

crystalline fraction is approximated by two Gaussian line profiles on the high-energy side of the spectrum. At the lower energies, peaks are fitted that represent the amorphous fraction. In figure 10(c) two asymmetrical Lorentzian line profiles are fitted to the spectrum, as reported by Touir et al. [9]. A good fit to the data is obtained, but no amorphous peak is fitted and therefore the crystalline fraction cannot be calculated.

It should be mentioned that the calculated crystalline fractions are sensitive to the range of data that is fitted. For example, when the Raman spectrum deposited using 10 sccm of SiH_4 is fitted with 3 Gaussian line profiles (column 5, first row in table 1) in the data range from 450 cm^{-1} to 550 cm^{-1} in stead of 400 cm^{-1} to 550 cm^{-1} the crystalline fraction changes from 0.46 to 0.40. The errors in the crystalline fractions that are obtained by fitting Gaussian line profiles are calculated from the inaccuracies in the peak areas that originate from the fitting procedure. The errors in column 4 correspond to the error in the number of counts. The errors in the fractions that are obtained with the method presented in this article (column 3) are estimated from the noise in the background after the subtraction of the amorphous signal. As stated in Sec. **4.3** the ratio of the Raman scattering cross-sections in *a*-Si:H and *c*-Si is set at 0.8 throughout this article, but can vary from 0.7 to 0.9 for the crystallite sizes in our samples [18]. This uncertainty results in an error of about 10% in the lower crystalline fractions and about 5% in the higher crystalline fractions. This error is neglected because it is smaller than the error induced by the noise in the measurements.

The crystalline fractions obtained by the method presented in this article are in good agreement with XRD results. Crystalline fractions obtained with peak fitting techniques that are presented in literature do not agree as well with the XRD results. The method presented here is not sensitive to the range of data points that is included. Furthermore, it is straightforward what part should be attributed to the crystalline, and what part to the amorphous part of the spectrum. And finally, there is no discussion about peak positions that should be fixed or not to obtain realistic results. These are clear advantages above peak fitting methods. The earlier reported discrepancy (Refs. 2 and 22) in the crystalline fractions obtained from XRD and Raman spectroscopy is not observed in our samples when the subtraction method described in this article is applied to the Raman spectra.

5. Conclusion

We have demonstrated an alternative technique to extract the structural composition of μc-Si:H from Raman spectroscopy. Crystalline fractions obtained using this technique show good agreement with fractions obtained from XRD analysis, in contrast to crystalline fractions obtained by frequently used fitting procedures in literature. Furthermore, the subtraction of the amorphous part of the spectrum (taken from a Raman spectrum of an *a*-Si:H film) clearly reveals the asymmetrical peak shape of the Raman spectrum of the crystalline fraction as calculated in literature. Interpretation difficulties arising from peak fitting are resolved in a natural way.

Acknowledgements

Prof. Dr. D.L. Williamson (Colorado school of Mines) is gratefully acknowledged for the XRD analyses and the extraction of the crystalline fractions from the XRD data. The Department of Chemical Technology, section R&CE, of the Delft University of Technology is acknowledged for the use of their Raman microscope. We thank Niek

van de Pers for the XRD analysis (figure 5). NOVEM is acknowledged for the financial support.

References

[1] R.E.I. Schropp and M. Zeman, Amorphous and microcrystalline silicon solar cells (1998, Kluwer academic publishers, Dordrecht, the Netherlands).

[2] L. Houben, M. Luysberg, P. Hapke, R. Carius, F. Finger , and H. Wagner, Phil. Mag. A **77**, 1447 (1998).

[3] D.L. Williamson, Mater. Res. Soc. Symp. Proc. **557**, 251 (1999).

[4] P. Roca i Cabarrocas and S. Hamma, Thin Solid Films **337**, 23 (1999).

[5] H. Richter, Z.P. Wang, and L. Ley, Solid State Commun. **39**, 625 (1981).

[6] R. Rizzoli, C. Summonte, J. Plá, E. Centurioni, G. Ruani, A. Desalvo, and F. Zignani, Thin Solid Films **383**, 7 (2001).

[7] Z. Iqbal, S. Vepřek, A.P. Webb, and P. Capezzuto, Solid State Commun. **37**, 993 (1981).

[8] I. H. Campbell and P. M. Fauchet, Solid State Commun. **58**, 739 (1986).

[9] H. Touir, J. Dixmier, K. Zellama, J.F. Morhange, and P. Elkaim, J. Non-Cryst. Solids **227-230**, 906 (1998).

[10] D.V. Tsu, B.S. Chao and S.R. Ovshinski, Appl. Phys. Lett. **71**, 1317 (1997).

[11] T. Ishidate, K. Inoue, K. Tsuji, and S. Minomura, Solid State Commun. **42**, 197 (1982).

[12] W.M.M. Kessels, R.J. Severens, A.H.M. Smets, B.A. Korevaar, G.J. Adriaenssens, D.C. Schram, and M.C.M. van de Sanden, J. Appl. Phys. **89**, 2404 (2001).

[13] B.A. Korevaar, C. Smit, R.A.C.M.M. van Swaaij, A.H.M. Smets, W.M.M. Kessels, J.W. Metselaar, D.C. Schram, and M.C.M. van de Sanden, Proc. of the 16th European Photovoltaic Solar Energy Conference, **B119** (2000).

[14] H.P. Klug and L.E. Alexander, X-ray diffraction procedures, 2nd ed. (New York: Wiley, 1974).

[15] Z. Iqbal and S. Vepřek, J. Phys. C **15**, 377 (1982).

[16] R. Tsu, J. Gonzalez-Hernandez, S.S. Chao, S.C. Lee, and K. Tanaka, Appl. Phys. Lett. **40**, 534 (1982).

[17] A.T. Voutsas, M.K. Hatalis, J. Boyce, and A. Chiang, J. Appl. Phys. **78**, 6999 (1995).

[18] E. Bustarret, M.A. Hachicha, and M. Brunel, Appl. Phys. Lett. **52**, 1675 (1988).

[19] S. Vepřek, F.A. Sarot, and Z. Iqbal, Phys. Rev. B **36**, 3344 (1987).

[20] Fit procedure is copied from [2], but since not all information is available, all Gaussian line profile parameters were free to vary and we included the data in the range 400 cm^{-1} to 550 cm^{-1} in the fitting procedure.

[21] Fit procedure is copied from [10], but since not all information is available, we included the data in the range 400 cm^{-1} to 550 cm^{-1} in the fitting procedure.

[22] Ch. Ossadnik, S. Vepřek, and I. Gregora, Thin Solid Films **337**, 148 (1999).

Chapter 5

Minimizing the incubation layer thickness of micro-crystalline silicon films by adjusting the processing pressure to the electrode separation in RF PECVD

C. Smit[1,2], M. C. M. van de Sanden[2], and R. A. C. M. M. van Swaaij[1]

[1] *Delft University of Technology, DIMES-ECTM, P. O. Box 5053, NL-2600 GB Delft, the Netherlands*
[2] *Eindhoven University of Technology, Dept. of Applied Physics, P.O. Box 513, 5600 MB Eindhoven, the Netherlands*

Abstract

The thickness of the amorphous incubation layer commonly found in microcrystalline silicon films is known to depend strongly on the deposition parameters. We deposited a series of films of varying thickness at different process gas pressures and electrode separations with RF PECVD. The crystalline fraction in the films is analysed using Raman spectroscopy. The results lead to the conclusion that there is an optimum combination of pressure and electrode separation to minimise the thickness of the incubation layer. Hence, for systems with a fixed electrode separation, it is important to determine the optimum pressure if thin microcrystalline films must be prepared. We propose a general rule for the optimum deposition pressure. It is shown that a small incubation layer is accompanied by a slow starting growth. Application as the window layer in p-i-n deposited solar cells confirms the quality of the films.

1. Introduction

Boron doped, microcrystalline thin silicon films are of interest to thin-film solar cell technology because they can be used as the top contact "window" layer [1,2]. These films are more transparent and electrically more conductive than amorphous silicon (carbide) doped layers. Moreover, the microcrystalline p-type layer could serve as a nucleation or "seed" layer for the subsequently deposited intrinsic microcrystalline silicon (μc-Si:H) layer in solar cells deposited in p-i-n sequence.

In order to minimize light absorption, the films must be as thin as possible (preferably 10-20 nm). This is a technological challenge, because the growth of μc-Si:H tends to start with an amorphous layer [3], mostly referred to as the incubation layer. Such an incubation layer is shown in figure 1, which is a high-resolution transmission electron microscope (HRTEM) image of μc-Si:H on Asahi U-type SnO_2:F. In the middle of the picture a silicon crystal is visible, but it is separated from the SnO_2:F by a thin amorphous layer of about 3 nm. Averaged over the entire sample, this amorphous film is probably a bit thicker. This amorphous incubation phase is thought to be disadvantageous for solar cell performance, because of the relatively high light absorption and low electrical conductivity.

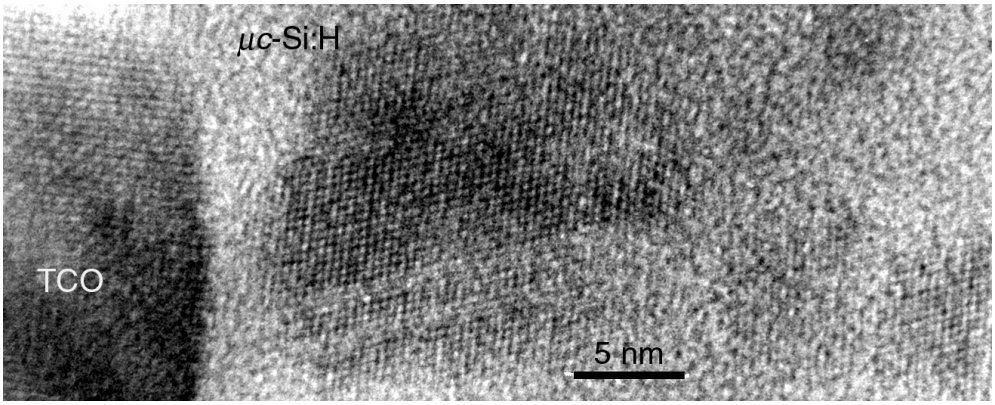

Figure 1. HRTEM picture of a part of a p-i-n deposited solar cell. On the left side the TCO is indicated (crystals of SnO_2:F), then a μc-Si:H p-layer of about 20 nm is deposited (deposition conditions are: $H_2/SiH_4/B_2H_6$ = 100/1/0.2 sccm, deposition pressure of 0.15 mbar, power of 40 W, and electrode separation of 35 mm). On the μc-Si:H p-layer an intrinsic μc-Si:H layer is deposited. The transition from p-type to intrinsic film is not visible. There is an *a*-Si:H incubation layer between the TCO and the crystals of the μc-Si:H. Only crystals with a 100, 110 or 111 orientation to the picture plane will show up, because of the limited resolution of the microscope.

The most widely used technique for the deposition of thin (doped) silicon films, amorphous (*a*-Si:H) as well as microcrystalline, is Radio Frequency Plasma Enhanced Chemical Vapour Deposition (RF PECVD). However, it is suggested that other deposition techniques are better suited to minimise the thickness of the incubation layer in μc-Si:H films. Miyajima et al.[4] obtained a 30% crystalline fraction in a 20-nm thin

film using hot-wire CVD. Hamma et al.[5] obtained a crystalline fraction of 30% in a film with a thickness of 12 nm on an *a*-Si:H substrate and of 19 nm on a Cr substrate with the layer-by-layer (LBL) technique, in which alternating cycles of deposition and etching are applied. Finger et al. [6] reported an improved and faster nucleation during the deposition of μc-Si:H on *a*-Si:H when the conventional RF PECVD excitation frequency of 13.56 MHz is increased to 95 MHz (VHF PECVD) and a decrease in the amorphous fraction in the initial stages of growth on glass and SiO_2:F.

Using conventional RF PECVD also small incubation layers can be obtained in μc-Si:H films. It is generally accepted that a high excitation power (0.1 – 1 W/cm^2) and a high dilution (~1%) of the silicon precursor gas SiH_4 in hydrogen (or sometimes helium) are key process parameters. In contrast to this, there is no consensus about the optimum process gas pressure. Roschek et al. [1] found 3 mbar as the optimum processing pressure for the conductivity and the uniformity of the films. The thickness of the incubation layer was not determined. Lihui et al. [7] show a clear crystalline fingerprint in the Raman spectrum of a 10-nm thick film deposited at a pressure of 4 mbar while only a small crystalline peak is visible for a 100-nm thick film deposited at the same growth rate at a pressure of 0.4 mbar. Sasaki et al. [8] obtain an incubation layer smaller than 10 nm at a pressure of 1.1 mbar. Rath et al. [9] found no crystalline fraction for a 25 nm thick film deposited at a pressure of 1.5 mbar, but when the pressure was decreased to 1 mbar a clear crystalline fraction could be observed from Raman spectroscopy even in a 15 nm thick film. In contrast to the previous reports, the research presented in reference 7 indicates that a lower pressure is favourable for a thin incubation layer. At very low pressures (0.07 mbar) Zhou et al. [10] claim to deposit amorphous free intrinsic films, but this is achieved in a triode PECVD system.

In this paper we show that the thickness of the incubation layer depends on the electrode separation and the pressure. In *a*-Si:H research there have been a few reports on the influence of the electrode separation on the material quality: the electrode separation is used to influence the type of radical (SiH_3 vs. SiH_2) that is responsible for the growth of the film [11] and it is also used to diminish the dust formation in the plasma during high pressure and high growth rate conditions [12, 13]. To determine the electrode separation that gives the smallest incubation layer in microcrystalline silicon the self-bias voltage of the plasma turns out to be a useful parameter. We noticed that the growth of some of the films is delayed with respect to the ignition of the plasma, or that the initial growth is very slow. This delay is shown to correlate with the thickness of the incubation layer. Finally the thickness of the incubation layer for the deposition of μc-Si:H on Asahi U-type SnO_2:F is addressed and we apply these films in p-i-n deposited solar cells. We conclude that the pressure should be adjusted correctly to the electrode-substrate separation and other geometrical influences in order to obtain good, doped microcrystalline films for application in solar cells.

2. Experiment

The deposition set-up is a homemade parallel plate 13.56 MHz RF PECVD reactor [14]. The substrate holder (grounded electrode) is about 13 cm × 13 cm and can hold substrates up to 10 cm × 10 cm. The powered electrode is circular with a diameter of

16 cm and the separation of the electrode and the substrate can be adjusted over a range from about 1 to 4 cm without breaking the vacuum. As substrates we used Corning 7031 glass, (111) *c*-Si, and for some depositions we used Asahi U-type SnO_2:F coated glass simultaneously. The following process conditions are used throughout this paper: the power is 40 W, the substrate temperature is 200°C, and the B_2H_6 flow (2% in H_2) is 0.2 sccm, which is about the lowest possible flow that can be set with the flow controller available.

We deposited a number of films with varying thickness at deposition pressures ranging from 0.07 to 1.0 mbar. At some pressures a thickness series was deposited at varying electrode separations. The dilution of SiH_4 in hydrogen is 1%, giving a growth rate in the order of 0.02 nm/s. For the higher pressures larger dilutions were chosen in order to maintain comparable low growth rates (0.67% and 0.33% for the depositions at 0.64 and 1.0 mbar, respectively). Even higher dilutions generally show no deposition after 15 minutes. The hydrogen flow is set at 150 sccm, except for the lower pressures (100 sccm and 70 sccm at 0.15 and 0.07 mbar, respectively) because the pumping capacity is limited.

The thickness of the films is determined by reflection-transmission spectroscopy. For films thinner than about 30 nm it is difficult to determine the thickness because there are not enough fringes to extract the refractive index as well as the thickness simultaneously. For these films the wavelength dependent complex refractive index from a 40-nm thick film with a crystalline fraction of 30% was used to fit the thickness. To validate this method, the thickness was also determined for some films using spectroscopic ellipsometry (SE). From the comparison of the SE and reflection-transmission results we estimate the error in the film thickness to be 50% for a film thickness up to 30 nm and of about 10% for films of 30 nm and thicker. Raman spectra

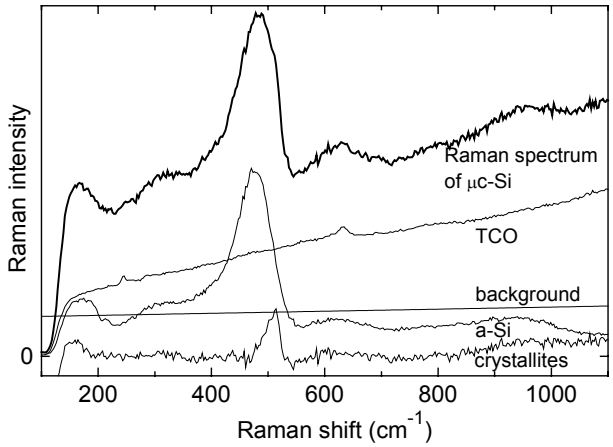

Figure 2. Raman spectrum of a μc-Si:H film of 15 nm on Asahi U-type TCO. The thick line is the measured spectrum itself; the thin lines are the constituents of the spectrum. The splitting of the spectrum is achieved by subtraction of a background, a spectrum of *a*-Si:H, and a spectrum of blank TCO, with scaling factors that are obtained in a root-mean-squares routine designed to minimize the background in the crystalline contribution (see reference 15).

were measured using a Renishaw Ramascope system 2000 in a backscattering geometry with a grating of 1800 lines/mm and a 2-mW Ar laser at a wavelength of 514.5 nm focused in a spot of about 1 μm. From these spectra we determined the crystalline fraction by subtraction of the Raman signal of an amorphous sample using a root mean square technique (see Chapter 4 or reference 15). This technique is very advantageous for the subtraction of the SnO_2:F component in the Raman spectra of the thin μc-Si:H films on the SnO_2:F coated substrates as well. Because the μc-Si:H films are thin, also background signal from the SnO_2:F appears in the spectra. This is shown in figure 2, where the Raman spectrum of a 15 nm thick μc-Si:H film on TCO is split into its crystalline silicon, amorphous silicon, and SnO_2:F components.

Some p-layers were tested in p-i-n solar cells. The cells are prepared on Asahi U-type TCO. Some of these substrates are covered by 40-nm thick ZnO layer, in order to prevent reduction of the SnO_2:F during the preparation of the solar cells. Then the p, i, and n layer are deposited followed by a back contact consisting of a 100-nm thick Ag layer and a 200-nm thick Al layer. The intrinsic *a*-Si:H layer is 450 nm thick. The microcrystalline n-type layer was deposited using similar conditions as for the p-type layer, except that 1.0 sccm PH_3 was used instead of B_2H_6. The cells are rectangular and have a surface area of 0.1 cm2. The external parameters of the cells are calculated from the J-V curve measured under AM 1.5 illumination from an Oriel solar simulator.

3. Results and discussion

3.1. Electrode separation

In figure 3 the crystalline fraction versus film thickness is shown for a deposition pressure of 0.30 mbar, at electrode separation of 23.5 and 35 mm. For the electrode separation of 23.5 mm a film of about 20 nm already contains a large crystalline

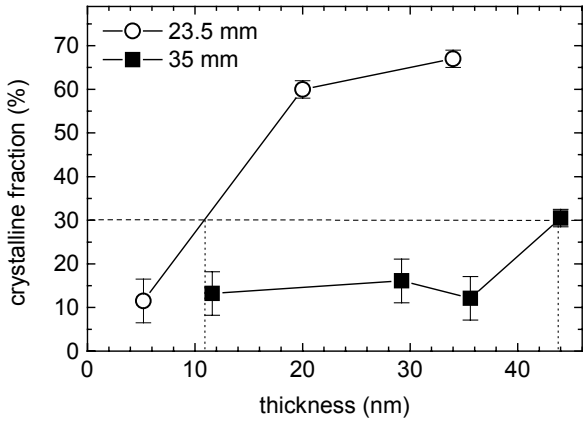

Figure 3. The thickness evolution of the crystallinity of the film for two electrode separations (shown in legend) at a deposition pressure of 0.3 mbar.

Table 1. Summary of the deposition conditions at which thickness series of microcrystalline films are deposited. The thickness of the incubation layer is indicated for the deposition on glass and for some films on Asahi U-type TCO as well. For this number we took the thickness at which the crystalline fraction reaches 30%, determined by interpolation.

Pressure (mbar)	Electrode-substrate dist. (nm)	SiH_4/H_2 flows (sccm)	Incubation layer thickness (nm)	
			on glass	on TCO
0.07	35	0.7/ 70	90	
0.15	35	1.0/100	15	12
0.15	29.5	1.0/100	8	
0.15	25	1.0/100	10	10
0.30	35	1.5/150	43	> 40
0.30	23.5	1.5/150	11	
0.64	23.5	1.0/150	11	> 80
1.00	23.5	0.5/150	55	> 40
1.00	15.5	0.5/150	6.3	27.3
1.00	15.5	1.5/150	40	

fraction, whereas for a 35 mm separation the film of 44 nm only contains a crystalline fraction of 30%. It is clear that the electrode separation plays an important role in the thickness of the incubation layer. This experiment is repeated for different pressures and the results are summarised in table 1. It should be noted that for these thin layers Raman spectroscopy (with an excitation wavelength of 514.5 nm) analyses the entire film. Since the film is inhomogeneous, starting amorphous, a crystalline fraction of 30% averaged over the entire film might imply a higher crystalline fraction towards the film surface.

As a figure of merit for the thickness of the incubation layer, we determined the thickness at which a crystalline fraction of 30% is reached by interpolation between the data points of the thickness series. This is shown in figure 3. We realise that this interpolation might introduce an error, but the thickness that is obtained will give a reasonable indication of the thickness of the incubation layer. From the results in table 1 it can be seen that also for pressures other than the 0.30 mbar shown in figure 3 the electrode separation has a large influence on the thickness of the incubation layer. For example, at a pressure of 1 mbar a thickness of the incubation layer of 55 nm is found for a separation of 23.5 mm, whereas the thickness of the incubation layer is reduced to 6.5 nm when the electrode separation is decreased to 15.5 mm. It is important to note that the optimum (i.e., giving the thinnest incubation layer) electrode separation is different for the two different pressures discussed above. In other words, the optimum pressure for minimising the thickness of the incubation layer depends on the reactor geometry and is different for every deposition system. This geometry dependence also explains the range of pressures that is reported in literature to obtain small incubation layers. In the following we try to find a general rule that applies to the optimum deposition pressure-electrode separation combination for any deposition system.

3.2. Bias voltage versus electrode separation

Visual inspection of the plasma showed that the light emission is not evenly distributed between the electrodes. Photographs taken of the plasma between the electrodes at a range of pressures at two different electrode separations (figure 4) show that the non-uniformity of the light emission is pressure dependent. At present we do not understand the reason for the non light-emitting region in the middle between the electrodes at higher pressures. At lower pressures the light emission becomes more homogeneous, and if the pressure is lowered even further, the plasma becomes unstable and extinguishes (e.g., 15.5 mm electrode separation, 0.50 mbar). This trend is visible at both electrode separations.

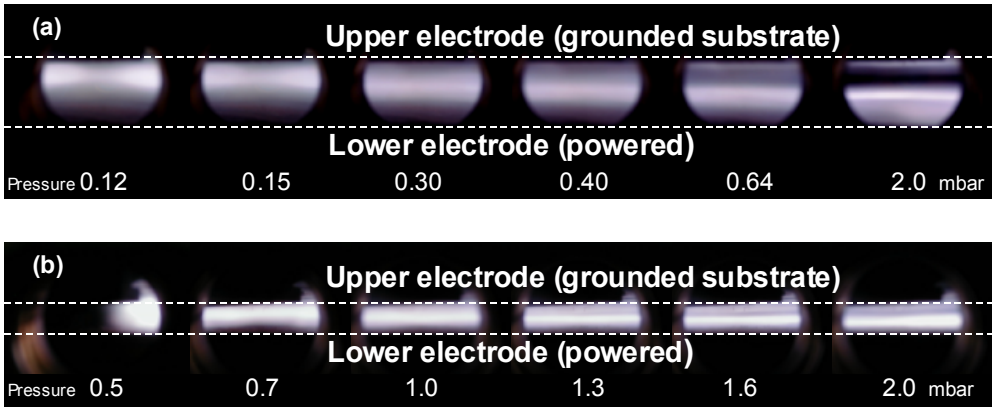

Figure 4. Photographs of the RF deposition plasma at a range of pressures and with an electrode separation of (a) 35 mm and (b) 15.5 mm. The light emission is not homogeneous and varies with pressure.

We noticed that the thinnest incubation layer was obtained as the electrode separation was decreased to the point where the glow is homogeneous. In fact, for these settings the plasma activity (light intensity) is the highest near the substrate. We measured the self-bias voltage on the powered electrode as a function of electrode separation for different pressures. The result is shown in figure 5. The measurement points of table 1 are indicated in the graph by solid symbols and the thickness of the incubation layer is indicated (black is thin, grey is thick, and the number gives the thickness in nm). If the electrode separation is decreased, the absolute value of the bias voltage decreases to a minimum at the point where the plasma becomes homogeneous. When the electrode separation is decreased even more then the bias voltage increases again. On the low-separation side of this minimum the light emission of the plasma becomes unstable, and when the electrode separation is decreased somewhat more the plasma extinguishes. However, the most important observation is that the deposition conditions that lead to a small incubation layer are all close to this minimum in the absolute value of the bias voltage. For higher pressures (1.0 mbar) the deposition

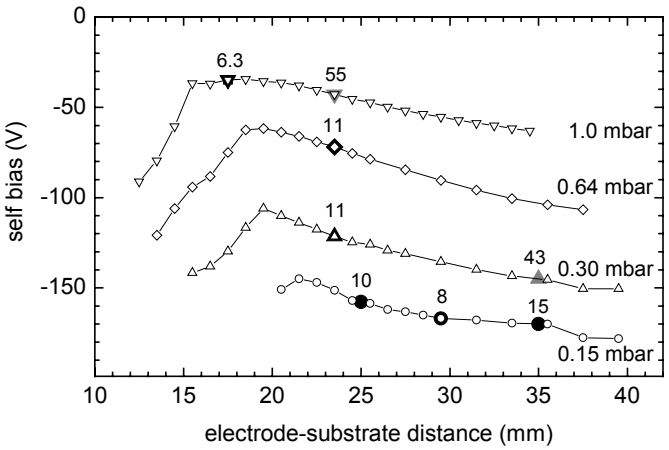

Figure 5. Measurement of the bias voltage as function of the electrode separation at the pressures that are used for the deposition of μc-Si:H films. The deposition conditions at which a thickness series is deposited are indicated, together with the 'incubation layer' thickness at which a crystalline fraction of 30% is obtained. Conditions giving small incubation layers are indicated with black markers, others with gray markers.

conditions that have only a little larger electrode separation already show a substantial thicker incubation layer. For lower pressures the range of electrode separations that lead to a thin incubation layer is somewhat larger, as can be concluded from the fact that for the pressure of 0.15 mbar the incubation layer is smaller than 15 nm for all of the electrode separations that are examined. At a pressure of 0.07 mbar no stable plasma could be obtained for the electrode separations in the range of 10 to 40 mm.

It has been argued in literature that crystallisation is influenced by ion bombardment. For example, it has been reported by Kondo [16] that the crystalline fraction in RF PECVD deposited μc-Si:H films decreases with ion energy. In order to obtain information about the influence of ion bombardment on the thickness of the incubation layer we measured the amplitude of the RF voltage, V_{RF}, on the powered electrode together with the DC self-bias voltage of the plasma, V_{DC}. The plasma potential with respect to ground, Vp, can be calculated using the relation $Vp = (V_{RF} + V_{DC})/2$. The plasma potential is plotted versus the electrode separation in figure 6 in the same manner as for the bias voltage in figure 5. A similar trend can be observed as in figure 5, where the self-bias voltage is plotted. Since the substrate is grounded, the plasma potential equals the impact energy of the ions at the substrate. In figure 7 we plotted the thickness of the incubation layer versus the plasma potential. We do not observe a correlation between the plasma potential and the thickness of the incubation layer. At present, we do not know what determines the thickness of the incubation layer. To our opinion, the most likely candidates are the atomic hydrogen flux towards the substrate and the radical composition arriving at the substrate.

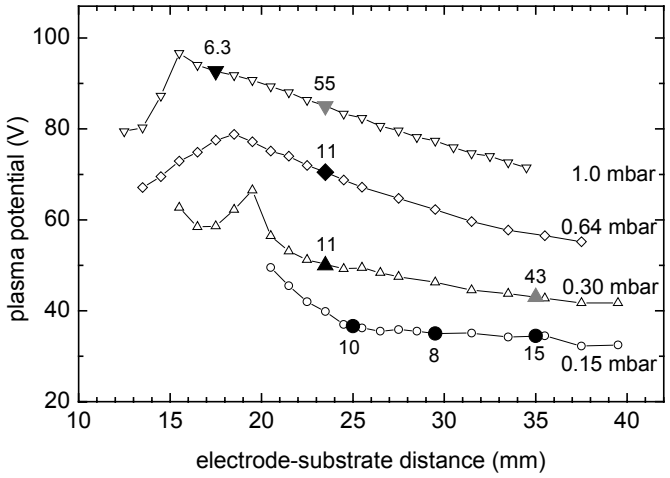

Figure 6. The plasma potential as calculated from the bias voltage and the RF amplitude as function of the electrode separation. As in figure 5, experimentally determined incubation layers are indicated.

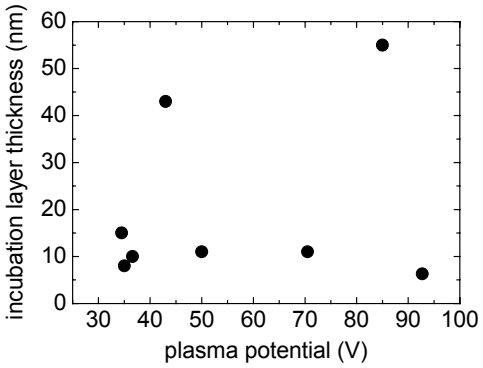

Figure 7. The incubation-layer thickness of the μc-Si:H film as a function of the plasma potential.

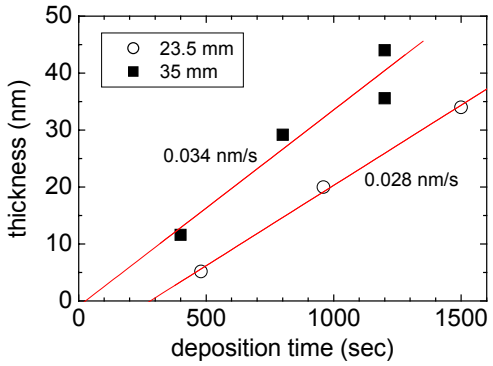

Figure 8. The film thickness versus the deposition time for two electrode separations (shown in legend) at a deposition pressure of 0.3 mbar.

3.3. Induction time versus thickness of the incubation layer

In figure 8 the film thickness is shown as a function of deposition time, again for the case of a process pressure of 0.3 mbar at the two different electrode separations of 23.5 and 35.0 mm. The variation of the growth rate (slope of the graph) is about 20%. Furthermore, the start of the growth of the film deposited at the smaller electrode separation (with a small incubation layer) is strongly affected by the electrode separation. It seems that it takes some time for the deposition to start, especially for the deposition that is carried out using an electrode separation of 23.5 mm. This time is referred to as induction time by Rovira et al. [3] who discuss the relation with the SiH_4

dilution. By fitting a straight line through the data we can obtain values for the growth rate and for the induction time. This has been done for all deposited thickness series. In figure 9 we plot the induction time versus the thickness of the incubation layer. We observe a clear correlation: the thinner the incubation layer, the longer it takes before the growth starts after the plasma is turned on. For comparison, for the deposition of device grade *a*-Si:H with RF PECVD (deposited with a different system) we find growth delays between –200 and +50 seconds. This indicates that in order to have nucleation either some sort of substrate modification is needed, or the first silicon atoms that attach to the substrate are easily etched away, or the effective sticking is slow on glass, so that the start of the growth is retarded.

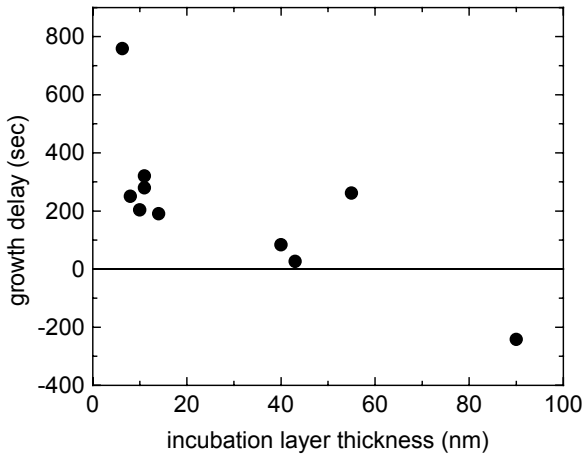

Figure 9. The delay of the start of the growth (induction time) versus the thickness of the incubation layer. The value for the delay is obtained from the intercept with the horizontal axis of the linear fit to the thickness series as shown in figure 4.

3.4. Application in solar cells

For solar cell technology it is more important to know the thickness of the incubation layer of microcrystalline silicon films on TCO. For some of the deposition settings films are deposited on Asahi U-type SnO_2:F substrates simultaneously with the depositions on glass and the crystalline fraction was determined from the Raman spectra. The thickness of the incubation layer of the depositions on TCO is also displayed in table 1. For the pressure of 0.15 mbar the thickness of the incubation layer is equal to that on glass, but for higher pressures the thickness of the incubation layer for deposition on TCO increases compared to deposition on glass. We conclude that the electrode separations of 25, 29.5, or even 35.5 mm at a pressure of 0.15 mbar are the most favourable of the conditions used here for the deposition of a microcrystalline p-type layer for application in p-i-n deposited solar cells. We used a microcrystalline p-type layer of 20 nm deposited with a electrode separation of 29.5 mm and a pressure of 0.15 mbar in an *a*-Si:H solar cell to compare its performance to that of a standard 12-

Table 2. External parameters of two solar cells: one with a standard 12-nm thick *a*-SiC:H p-type layer, one with a 20-nm thick *μc*-Si:H p-layer deposited with an electrode separation of 35 mm and at a pressure of 0.15 mbar.

Substrate	P-type layer	T_{depo} i-layer (ºC)	Voc (V)	Jsc (A/m^2)	FF	Efficiency (%)
Asahi TCO	*a*-SiC:H	200	0.84	138	0.69	8.0
Asahi TCO + ZnO	*a*-SiC:H	200	0.83	143	0.70	8.3
Asahi TCO	*μc*-Si:H	200	0.71	114	0.70	5.7
Asahi TCO + ZnO	*μc*-Si:H	200	0.79	136	0.72	7.7
Asahi TCO + ZnO	*μc*-Si:H	250	0.74	138	0.68	7.0
Asahi TCO + ZnO	*μc*-Si:H	300	0.75	102	0.46	3.5

nm thick *a*-SiC:H p-type layer. The results are shown in table 2. The cell with the microcrystalline p-type layer has a lower efficiency than the cell with the amorphous p-type layer (5.7% and 8.0%, respectively). The same cells have been prepared on Asahi TCO substrates covered with 40 nm ZnO. In the case of the amorphous p-type layer there is no significant difference, but the performance of the cell with the microcrystalline p-type layer is now comparable to the cell with the amorphous p-type layer. The J-V curves of these cells are shown in figure 10. The results indicate that the microcrystalline p-type layer is good, but does not perform well in combination with the Asahi TCO, probably due to the reduction of the SnO_2:F. Also the temperature stability is tested. Identical solar cells are prepared on Asahi TCO substrates covered with 40 nm ZnO, but the amorphous intrinsic layer is deposited at 250ºC and 300ºC. Clearly the efficiency decreases with temperature, especially at 300ºC, mainly due to a drop in fill factor and short-circuit current density, J_{sc}, indicating that the p-type layer is destroyed.

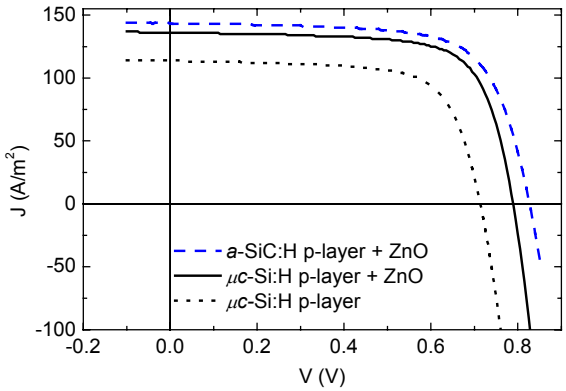

Figure 10. J-V curves of solar cells with a microcrystalline p-type window layer directly on Asahi U-type SnO_2:F and on ZnO covered SnO_2:F. For comparison, also a cell with an *a*-SiC:H p-type layer on ZnO covered SnO_2:F is shown.

4. Conclusions

We demonstrated that the separation of the electrode and the substrate in RF PECVD has an important influence on the thickness of the incubation layer of p-type microcrystalline silicon, in combination with the process pressure. The minimum thickness of the incubation layer is achieved when the electrode separation is lowered until the plasma becomes unstable and extinguishes. This point coincides with a minimum in the absolute value of the bias voltage. Since not many deposition set-ups can vary the electrode separation easily, it is important to optimise the pressure to the electrode separation. Therefore, an alternative way of achieving thin incubation layers is to lower the pressure until the plasma becomes unstable and extinguishes. However, for deposition on SnO_2:F instead of glass, lower pressures of around 0.15 mbar are more suitable. On TCO as well as on glass we achieved a crystalline fraction of 30% in microcrystalline films of 10 nm thick at a pressure of 0.15 nm and an electrode separation of 25 mm. In our deposition system, we did not obtain good results for a pressure of 0.07 mbar. Furthermore, a small incubation layer is shown to correlate with a slow or delayed start of the growth. Delays in excess of 10 minutes have been observed. The microcrystalline p-type layers deposited with a thin incubation layer have successfully been applied in p-i-n deposited solar cells that show comparable performance to solar cells with an *a*-SiC p-type window layer. The microcrystalline p-type layers do not very well resist temperatures of above 250°C.

Acknowledgements

The Department of Chemical Technology, section R&CE, of the Delft University of Technology is acknowledged for the use of their Raman microscope. Erik Buiskool of Akzo Nobel is acknowledged for the deposition of the ZnO. We thank Ries van de Sande and Jo Jansen for the design and the construction of the deposition set-up "Cascade", and for their technical support. We also thank Arjan Driessen and Martijn Tijssen for their technical support. Novem is acknowledged for the financial support.

References

[1] T. Roschek, J. Müller, S. Wieder, B. Rech, H. Wagner, Proceedings of the 16th European Photovoltaic Solar Energy Conference, Glasgow, UK (2000), VB.1.39.

[2] J.K. Rath, C.H.M. van der Werf, F.A. Rubinelli, R.E.I. Schropp, Proceedings of the 25th IEEE Photovoltaic Specialist Conference, Washington D.C. (1996), 1101.

[3] P.I. Rovira, A.S. Ferlauto, R.J. Koval, C.R. Wronski, R.W. Collins, G. Ganguly, Mater. Res. Soc. Symp. Proc. **609,** A19.6.1 (2000).

[4] S. Miyajima, M. Kim, M. Konagai, A. Yamada, Proceedings of the 17th European Photovoltaic Solar Energy Conference, Munich, Germany (2001), 2861.

[5] S. Hamma, P. Roca i Cabarrocas, Mater. Res. Soc. Symp. Proc. **507,** 511 (1998).

[6] F. Finger, R. Carius, P. Hapke, L. Houben, M. Luysberg, M. Tzolov, Mater. Res. Soc. Symp. Proc. **452**, 725 (1997).

[7] G. Lihui, L. Rongming, Thin Solid Films **376**, 249 (2000).

[8] T. Sasaki, S. Fujikake, Y. Ichikawa, Jpn. J. of Appl. Phys. **39**, 4707 (2000).

[9] J.K. Rath, R.E.I. Schrop, Solar Energy Mater. and Solar Cells **53**, 189 (1998).

[10] J-H. Zhou, K. Ikuta, T. Yasuda, T. Umeda, S. Yamasaki, K. Tanaka, J. of Non-Cryst. Solids **227-230**, 857 (1998).

[11] P. Kounavis, D. Mataras, N. Spiliopoulos, E. Mytilineou, D. Rapakoulias, J. of Appl. Phys. **75**, 1599 (1994).

[12] M. Isomura, M. Kondo, A. Matsuda, Sol. Energy Mat. and Sol. Cells **66**, 375 (2001).

[13] D. Das, S. Chattopadhyay, A.K. Barua, R. Banerjee, J. of Appl. Phys. **78**, 3193 (1995).

[14] B.A. Korevaar, C. Smit, R.A.C.M.M. van Swaaij, A.H.M. Smets, W.M.M. Kessels, J.W. Metselaar, D.C. Schram, M.C.M. van de Sanden, Proceedings of the 16th European Photovoltaic Solar Energy Conference, Glasgow, UK (2000), B119.

[15] C. Smit, R.A.C.M.M. van Swaaij, H. Donker, A.M.H.N. Petit, W.M.M. Kessels, M.C.M. van de Sanden, J. of Appl. Phys. **94**, 3582 (2003).

[16] M. Kondo, Solar Energy Mater. and Solar Cells **78**), 543 (2003).

Chapter 6

High-rate deposition of microcrystalline silicon with an expanding thermal plasma

C. Smit[1,2], A. Klaver[1], B.A. Korevaar[1,2], A.M.H.N. Petit[2], D.L. Williamson[3], R.A.C.M.M. van Swaaij[2], and M.C.M. van de Sanden[1]

[1] *Eindhoven University of Technology, Department of Applied Physics, P.O. Box 513, 5600 MB Eindhoven, the Netherlands*
[2] *Delft University of Technology, DIMES, P.O. Box 5053, 2600 GB Delft, the Netherlands*
[3] *Colorado School of Mines, Department of Physics, Golden, CO 80401, U. S. A.*

Submitted to Thin Solid Films

Abstract

Hydrogenated microcrystalline silicon has been deposited at elevated deposition rates using an expanding thermal plasma for the decomposition of the precursor gas silane (SiH_4). An extensive survey of the influence of the deposition parameters on the optical, electrical, and structural material properties is carried out. X-ray diffraction and Raman spectroscopy reveal the transition from amorphous to microcrystalline deposition conditions. Reflection-transmission measurements are used to determine the thickness, the refractive index, and the absorption coefficient. Scanning electron microscopy analyses shows columnar growth and infrared absorption shows varying oxygen content. It is demonstrated that the best material is obtained when a pure hydrogen plasma, instead of a mixture of Ar and H_2, is used and the precursor gas (SiH_4) is injected into the plasma at about 55 mm above the growing film. The best material properties are obtained when the SiH_4 flow is adjusted such that the material is near the transition of microcrystalline to amorphous silicon. For these conditions the dark and photoconductivities are approximately 10^{-8} S/cm and 10^{-6} S/cm, respectively. The first attempts of the incorporation of this material in solar cells are presented. It is concluded that the expanding thermal plasma is well suited for the deposition of microcrystalline silicon and growth rates up to 3.7 nm/s have been obtained. However, further optimisation of the structural and opto-electronic properties is still necessary.

1. Introduction

For thin film silicon solar cell applications much research effort is directed towards high-rate deposition of the intrinsic silicon film, because a higher growth rate increases the production throughput, which in turn can decrease the production cost. Using expanding thermal plasma chemical vapour deposition (ETP CVD) for the deposition of hydrogenated amorphous silicon (*a*-Si:H) deposition rates up to 10 nm/s have been achieved [1]. Recently, ETP CVD deposited *a*-Si:H films have been successfully incorporated in solar cells at deposition rates up to 7 nm/s [1,2].

In tandem solar cells the application of hydrogenated microcrystalline silicon (*μc*-Si:H) films is attractive, because the optical band gap of this material is ideally tuned to the solar spectrum when incorporated as the intrinsic layer in the bottom cell [3]. Furthermore, compared to *a*-Si:H this material hardly degrades when subjected to prolonged illumination. However, the light absorption of this material is much lower than that of *a*-Si:H. A film of about 2 μm is needed to absorb enough light, if efficient light trapping is realized. Therefore high deposition rates are required to have acceptable deposition times.

So far, deposition rates of about 0.1 nm/s are achieved with conventional radio-frequent plasma enhanced chemical vapour deposition (RF PECVD). Higher rates have been reported for special deposition conditions, for example by Roschek *et al.* [4], who obtained conversion efficiencies of 8.1% and 6.6% for single junction *μc*-Si:H solar cells deposited at rates of 0.5 nm/s and 1.0 nm/s, respectively. Also results have been reported with other techniques. Feitknecht *et al.* [5] reported a conversion efficiency of 7.8% for a single junction *μc*-Si:H cell deposited at a rate of 0.74 nm/s using very high frequency (VHF) PECVD. Rath *et al*. reported a conversion efficiency of 4.4% for a single junction *μc*-Si:H cell deposited at a rate of 1.3 nm/s using hot-wire (HW) CVD [6]. The most successful method for *μc*-Si:H deposition at high rates is VHF high-pressure deposition (VHF HPD) [7]. Using this deposition method an efficiency of 8.1% has been reported at a rate of 1.2 nm/s.

In this paper we use ETP CVD for the deposition of *μc*-Si:H. We varied the deposition parameters and studied the influence on the material properties. The SiH_4 and the Ar/H_2 flows are varied, covering the transition regime between amorphous and microcrystalline material. Subsequently, with a modified plasma source we were able to deposit *μc*-Si:H films using a pure hydrogen plasma for the decomposition of SiH_4. Furthermore, the position of the SiH_4 injection is varied and its effect on *μc*-Si:H is studied. The best *μc*-Si:H films are incorporated in p-i-n deposited solar cells.

2. Experiment

2.1. The deposition set-up

Film depositions were carried out in the so-called “cascaded arc solar cell apparatus Delft Eindhoven” (CASCADE) deposition set-up [8]. This set-up consists of a reactor for the deposition of the intrinsic layers using ETP CVD and a reactor for the

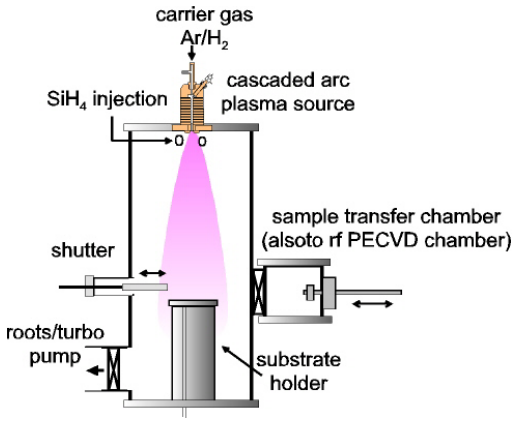

Figure 1. Schematic representation of the ETP CVD deposition set-up.

deposition of the doped layers using RF PECVD. The two chambers are connected via a load lock chamber. The ETP reaction chamber is schematically depicted in figure 1 and the deposition technique is extensively described elsewhere [9]. In the deposition process a plasma of a mixture of argon and hydrogen is created in the cascaded-arc plasma source by a DC discharge current of 50 A at a pressure of 0.1 to 1.5 bar, depending on the gas flows. This arc plasma is build up in a discharge channel between three tungsten cathodes and an anode plate and expands into the low-pressure (typically 0.2 to 0.5 mbar) reaction chamber. The precursor gas, silane (SiH_4), is fed into an "injection ring" with holes, which is situated in the reaction chamber and is concentric with the plasma expansion. The most important reactive species produced in the plasma source at these gas flows is atomic hydrogen [10]. Atomic hydrogen reacts with SiH_4 molecules forming H_2 and SiH_3. Subsequent hydrogen abstraction reactions of atomic hydrogen with SiH_3 forming SiH_2 and so on are possible, depending on the process parameters [11]. The SiH_4 consumption by the plasma, i.e., the fraction of SiH_4 that is consumed, is monitored with a mass spectrometer that is mounted on the side of the reactor at substrate level [9]. It samples the stable gases in the background of the plasma jet.

Two different geometries for the cascaded-arc plasma source have been used. The first one consists of six cascaded copper plates building up a discharge channel of 30 mm long with a diameter of 2.5 mm. The advantage of this source is that it can be operated at relatively low gas flows (typically 600 sccm Ar and 200 sccm H_2) and therefore a low pump capacity is sufficient to obtain the required process pressure of about 0.2 mbar. This source, referred to as the 2.5-mm arc, cannot be operated on hydrogen gas only, but a minimum argon flow of twice the hydrogen flow must be added for stable arc operation. In this research this source is always operated at an Ar/H_2 flow ratio of 2:1 because for the deposition of μc-Si:H the hydrogen dilution is important. In order to be able to operate a pure hydrogen plasma a source with a different geometry is installed. The discharge channel is now created by four stacked plates with holes having a diameter of 4 mm and is about 20 mm long. This source,

referred to as the 4-mm arc, is operated typically at 1500 sccm or 2000 sccm H_2. Also Ar-H_2 mixtures in a 2:1 ratio like 120 sccm Ar and 600 sccm H_2 have been investigated in order to compare its behaviour with the 2.5-mm arc. The substrate is positioned 41 cm below the plasma source exit. The substrate temperature is 300ºC throughout this work, unless stated otherwise.

2.2. Film analysis

The films (thickness of about 600 nm) are deposited on Corning 1737 glass and n-type <111> crystalline silicon (*c*-Si) wafer simultaneously. They are analysed using reflection-transmission spectroscopy, Raman spectroscopy (Renishaw Ramascope system 2000, grating 1800 lines/mm, in a backscattering geometry with a 2 mW Ar laser at a wavelength of 514.5 nm focused in a spot of about 1 μm), Fourier transform infrared spectroscopy (FTIR, Bruker Vector II), and dark and photoconductivity measurements. The latter was measured using an Oriel AM1.5 solar simulator. The conductivities are measured using co-planar electrode geometry. The crystalline fractions are obtained from the Raman spectra by the subtraction of a Raman spectrum of an amorphous sample (Chapter 4 or Ref. 12). It should be realized that all crystalline fractions are calculated assuming material without voids. In other words, they are not crystalline volume fractions, but crystalline mass fractions. Some films were additionally investigated with x-ray diffraction (XRD) (Bruker-Nonius D5005 θ/θ diffractometer with diffracted beam graphite monochromator, wavelength Cu-α), some with scanning electron microscopy (SEM, Philips XL30SFEG). For FTIR, XRD and SEM analysis the samples deposited on *c*-Si are used. The SEM samples are cut and the image is taken from the cutting edge (20º angle) to get a cross-sectional view. Furthermore, a small set of samples has been analysed with small angle x-ray scattering (SAXS) and flotation density measurements to obtain information about the

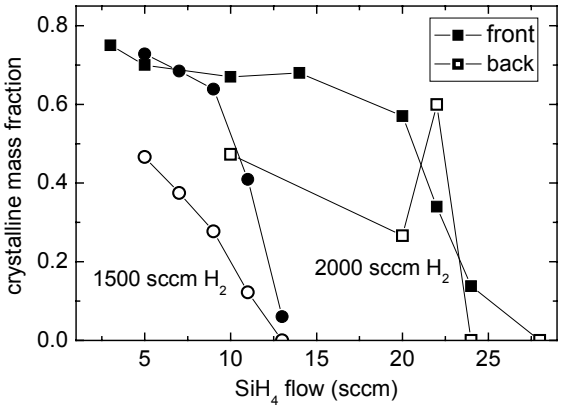

Figure 2. Crystalline fraction of two sample series deposited using 1500 (circles) and 2000 sccm (squares) of H_2 with the optimised injection position. The crystalline mass fraction is calculated from the Raman signal taken from the backside of samples on glass (open symbols) and are compared with the fractions at the front side of the samples (closed symbols).

porosity. For these measurements samples have been prepared of 5-μm thick *μc*-Si:H films on 10-μm-thick, high-purity (99.999%) Al foil.

In this work the crystalline mass fraction and the refractive index at 2 eV will be used as a first indication for the quality of the *μc*-Si:H films. Concerning the crystalline mass fraction, it should be realised that *μc*-Si:H films in general are not uniform throughout the film. This is revealed by Raman analysis from the front side and from the backside (through the glass substrate) of *μc*-Si:H samples (figure 2). Due to the short penetration depth of the laser light of 514 nm that is used in the analysis only the upper ~ 50 nm of the film is analysed. From figure 2 it can be observed that the substrate side of the films shows a lower crystalline fraction than the upper side. This indicates that the *μc*-Si:H growth exhibits an amorphous incubation layer. The Raman analyses used in this research are taken from the front side of the samples.

Furthermore, concerning the refractive index the following should be taken into account. Although the refractive index at 2 eV is more sensitive to electronic excitations than the infrared refractive index, the two correlate quite well, as can be observed from figure 3. This indicates that both are well suited for the optimisation of the material quality. Furthermore, also the photoconductivity, an important material property when applied in electronic devices, positively correlates with the refractive index at 2 eV (figure 4). In this research we take the refractive index at 2 eV for a first optimisation of the deposition parameters.

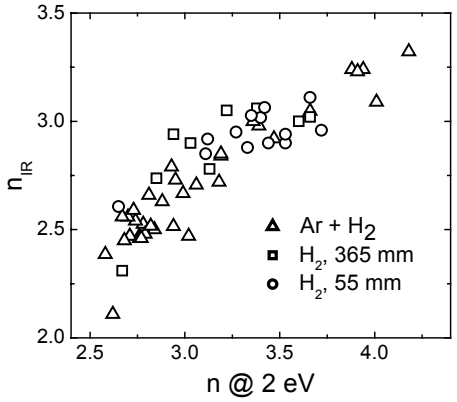

Figure 3. Measurements showing the correlation between the infrared refractive index and the refractive index at 2 eV.

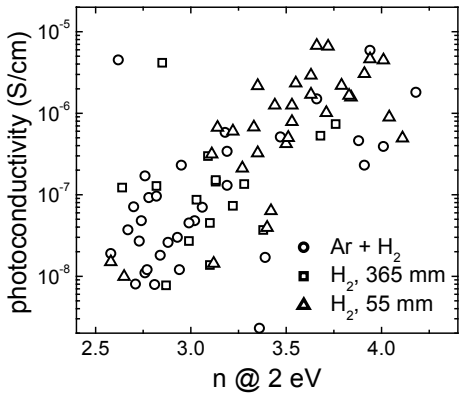

Figure 4. Measurements showing the correlation between the photoconductivity and the refractive index at 2 eV.

2.3. Solar cell preparation and analysis

Solar cells have been prepared in p-i-n deposition sequence on Asahi U-type transparent conductive oxide (TCO) covered glass. These substrates are covered by 40-nm thick ZnO layer to prevent reduction of the SnO_2 during the preparation of the solar cells. Then the p, i, and n layer are deposited followed by a back contact consisting of a 100-nm thick Ag layer and a 200-nm thick Al layer. The microcrystalline doped layers

are deposited using RF PECVD with 100 sccm H_2, 1 sccm SiH_4, 0.2 sccm B_2H_6 or 1.0 sccm PH_3 (2% in H_2), an electrode separation of 29.5 mm, a process pressure of 0.15 mbar, a power of 0.40 W/cm^2 substrate, and the thickness of the layers is 20 nm (the optimisation of these doped layers is described in Chapter 5). The cells are square and have a surface area of 0.1 cm^2.

The external parameters of the cells are calculated from the current density versus voltage (*J-V*) curve measured under AM 1.5 illumination. Furthermore, the spectral response has been measured at varying bias voltage with a bias light applied to the cell to simulate normal operation conditions during the analysis.

3. Results and discussion

3.1. Varying the deposition parameters

3.1.1. 2.5-mm arc

In most PECVD techniques there is a threshold dilution *R* ($R = H_2/(H_2 + SiH_4)$) for the deposition of *μc*-Si:H (e.g., [13]). A series of films has been deposited using a SiH_4 flow varying from 0.5 to 40 sccm. The hydrogen gas flow and the argon flow were kept constant at 600 sccm and 1200 sccm, respectively. The substrate temperature was kept constant at 300ºC. From figure 5 (XRD measurements) and figure 6 (Raman spectra) it can be concluded that the samples cover the transition from *a*-Si:H to *μc*-Si:H. Crystalline silicon (*c*-Si) shows up in the XRD graphs as a sharp peak at 28°, 47°, and 56° for the crystallites that are oriented in the (111), (220), and (311) direction

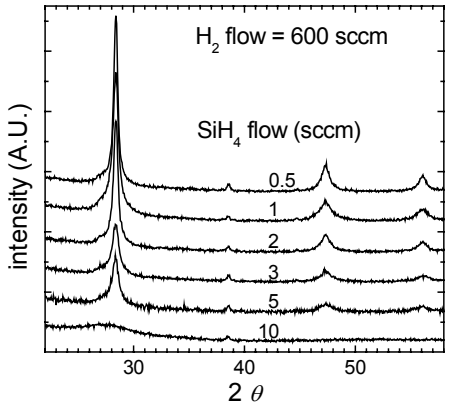

Figure 5. XRD analyses of a series of samples deposited using an Ar flow of 1200 sccm, a H2 flow of 600 sccm, and varying SiH4 flow. The film deposited using 10 sccm of SiH4 shows no crystalline fraction; decreasing the SiH4 flow results in an increasing crystal

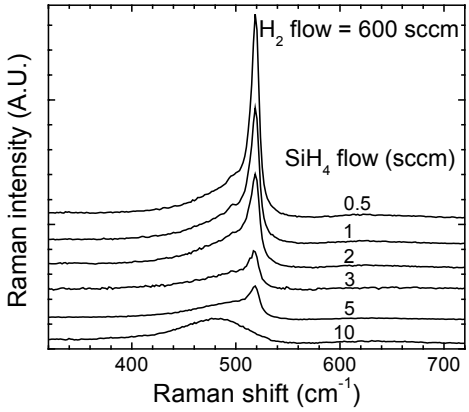

Figure 6. Raman spectra of the same set of samples as in Figure 5. From these spectra it is shown also that the transition from amorphous to microcrystalline silicon deposition is between 5 and 10 sccm SiH_4.

respectively. In the Raman spectra *c*-Si reveals itself by a sharp peak at 520 cm^{-1} and *a*-Si by a smooth feature around 480 cm^{-1}. Clearly, for higher SiH_4 flows a lower crystalline mass fraction is obtained and the film deposited using 10 sccm SiH_4 is completely amorphous.

In figure 7 the process parameter window has been extended: the hydrogen gas flow was varied from 300 to 1400 sccm for three different SiH_4 flows: 2, 5, and 10 sccm. In general, an increase of the hydrogen flow into the plasma source results in an increase of the atomic hydrogen flow at the exit of the source [9], which is used for the decomposition of the SiH_4 molecules and enhances the crystallization of the growing film. Moreover, since the pump speed is fixed, the pressure in the reaction chamber increases, which influences the plasma expansion. By visual inspection of a pure Ar plasma it can be noticed that the plasma expansion becomes narrower when the pressure is increased. Therefore, the deposition is concentrated on a smaller surface and becomes less homogeneous for higher pressures.

The influence of the hydrogen flow on the crystallinity, the SiH_4 depletion, the growth rate, and the refractive index at 2 eV is examined. In figure 7a we can see the transition occur from amorphous to microcrystalline material. Consistent with the findings described above for the SiH_4 series, at higher hydrogen dilutions atomic hydrogen reaches the growing surface and enables the formation of crystallites. Only the samples deposited using a SiH_4 flow of 2 sccm show a substantial

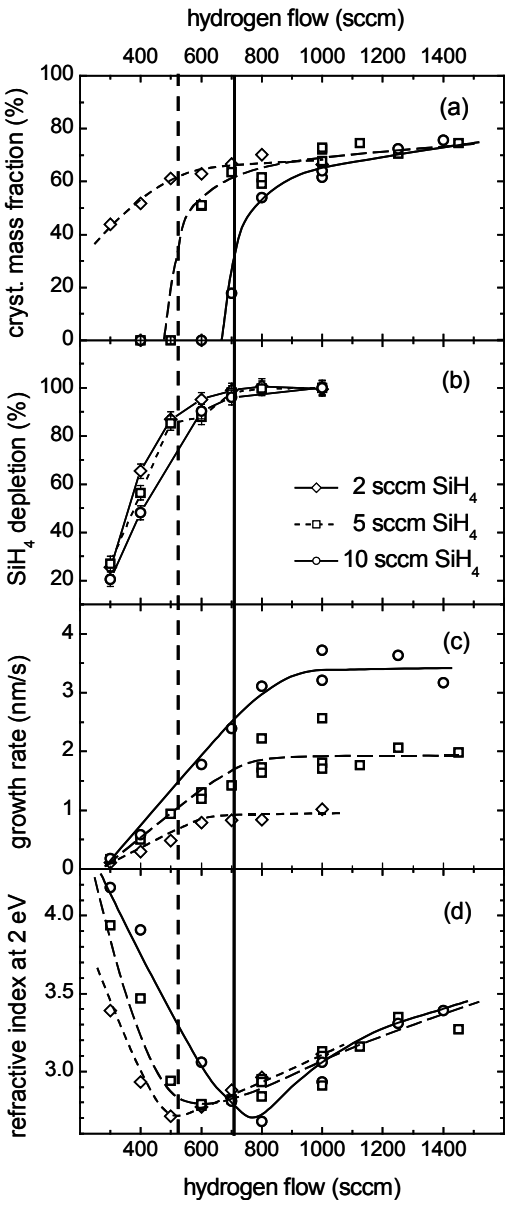

Figure 7. (a) The crystalline mass fraction, (b) the SiH_4 depletion, (c) the growth rate, and (d) the refractive index as a function of the hydrogen flow. The Ar flow is set at twice the H_2 flow; three different SiH_4 flows are used as indicated in the legend. The vertical lines indicate the transition between amorphous and microcrystalline silicon, taken at a crystalline mass fraction of 30%.

crystalline mass fraction over the entire hydrogen flow range.

In figure 7b the depletion increases as the hydrogen flow (and with it the available atomic hydrogen flux) increases until the point where all SiH_4 is dissociated and the depletion saturates at 100%. When all SiH_4 is consumed, adding even more hydrogen will not result in a higher density of depositing radicals, so at this hydrogen flow also the growth rate saturates, at about 1, 2, and 3.5 nm/s for SiH_4 flows of 2, 5, and 10 sccm, respectively (figure 7c). To be more precise, the growth rate saturates at a higher hydrogen flow, because the extra hydrogen that is added after the depletion reaches almost 100% is used for hydrogen abstraction reactions with SiH_3, leading to SiH_2, SiH, and Si, which have higher sticking probabilities. In that case it is the increase of the average sticking coefficient that leads to higher growth rates, rather than an increase in the number of depositing radicals. When most of the hydrogen is stripped from the SiH_4 molecules a further increase of the H_2 flow will not result in even higher growth rates.

The refractive index at 2 eV shows a minimum, as shown in figure 7d. The refractive index decreases with hydrogen flow for the amorphous films, and even for the μc-Si:H films that are close to the transition regime. In the microcrystalline regime the refractive index increases again to 3.4 with increasing hydrogen flow. However, for the highest hydrogen and argon flows we noticed by means of interferometry on a double polished *c*-Si wafer that the plasma heated up the substrate to 450ºC. This warming up probably causes the increase in material density, responsible for the higher refractive index. At these high gas flows the temperature is not constant and the minimum in the curve for the refractive index is a temperature effect.

It should be noticed that there is a clear difference in behaviour of the crystalline mass fraction for the 5 and 10 sccm SiH_4 flows compared to the 2 sccm flow. The crystalline mass fraction for the two higher SiH_4 flows drops to zero rapidly as the hydrogen flow is decreased to a level where most of the atomic hydrogen is consumed (compare figs. 7a and b) in hydrogen abstraction reactions with SiH_4. However, this is not the case for the 2-sccm SiH_4 flow series. Apparently, even at very low H_2 flows, at which the available atomic hydrogen density is not high enough to decompose all SiH_4, there is still atomic hydrogen arriving at the substrate surface as must be concluded from the crystalline mass fraction. This suggests that for the 2 sccm SiH_4 the reaction rate of H with SiH_4 is so low that enough atomic hydrogen survives on the way from the plasma source to the substrate to enhance the crystallization of the growing film.

3.1.2. 4-mm arc and a pure hydrogen plasma

From photoconductivity measurements and the refractive index we concluded that the material quality obtained with the 2.5-mm arc as described above is not sufficient and that the material is probably not dense enough. In order to increase the material density further we carried out ETP CVD with pure hydrogen. Without argon a lower ion density is expected in the plasma, which will influence the plasma chemistry. Therefore, we redesigned the cascaded arc plasma source: the discharge channel diameter was enlarged from 2.5 to 4 mm. This is necessary to be able to run the plasma source on pure hydrogen.

A series of samples was prepared using a pure hydrogen plasma. The silane flow was set at 10 sccm and the results are shown in figure 8. In order to be able to compare

depositions using the 2.5-mm and the 4-mm arc we also deposited a series of films with Ar and H_2 flow in a two-to-one ratio with the 4-mm arc. The same settings were used with the 2.5-mm arc, enabling a comparison of the 2.5-mm and the 4-mm arc. The results for the 2.5-mm arc are also plotted in figure 8. Note that the vertical axis now displays the total gas flow instead of the hydrogen flow. Again, the vertical dashed lines denote the transition from amorphous to microcrystalline silicon, taken at 30% crystallinity.

The films deposited using the 4-mm arc have higher refractive indices, lower crystallinity, and are deposited with a lower growth rate than the films with the 2.5-mm arc. However, the differences are small. To compare the material quality for the films deposited using pure H_2 gas and the Ar-H_2 gas mixture in the arc we examine the refractive index. In figure 8 we concentrate on the film with the highest refractive index that is still microcrystalline. This point can be found at the crossing of the vertical line and the graph of the refractive index. For the films using the Ar-H_2 mixture (both 2.5-mm and 4-mm arc) the refractive index at the amorphous-microcrystalline transition line is about 2.8. But for the case in which the plasma source is fed with only hydrogen the highest refractive index obtained for microcrystalline material is 3.3. However, it should be realized that the deposition rate for the Ar-H_2 mixtures is higher (about 2.5 nm/s) than for the pure hydrogen deposition shown here (0.6 nm/s). For the films grown at lower rates with the 2.5-mm arc and an Ar-H_2 mixture (see figure 7) the refractive index is still lower than for the films deposited using only H_2 in the arc. The only films with a higher refractive index

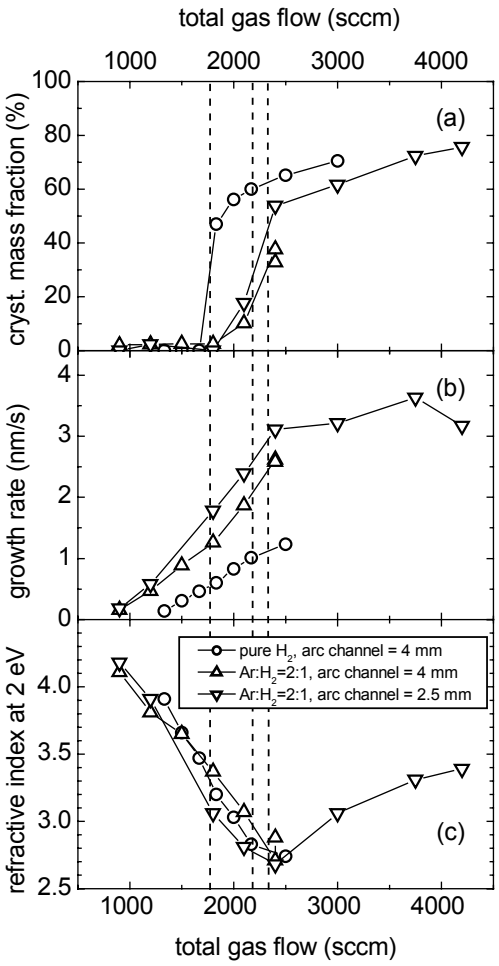

Figure 8. (a) The crystalline mass fraction, (b) growth rate, and (c) the refractive index as a function of the total gas flow (Ar + H_2). Three deposition series are shown with the SiH_4 flow set at 10 sccm. One series is deposited using the 2.5-mm arc and an Ar-H_2 plasma and is copied from Figure 7. The next series is deposited with the 4-mm arc, again using the same Ar-H_2 mixture as in the first series. The last series is deposited using the 4-mm arc and a pure hydrogen plasma. The dashed lines indicate the transition from amorphous to microcrystalline silicon, taken at a crystalline mass fraction of 30%.

in figure 7 are the ones deposited using a SiH_4 flow of 2 sccm, at low Ar and H_2 flows. But then the growth rate is very low (about 0.1 nm/s). It must be concluded that a pure hydrogen plasma results in denser microcrystalline material than a plasma of a Ar-H_2 mixture with a 2-to-1 flow ratio at comparable growth rates.

3.1.3. Variation of the position of SiH_4 injection

Although improved by switching to a pure hydrogen plasma, the material density is still not high enough. Aiming for a higher refractive index the position at which the SiH_4 is injected into the expanding plasma is varied. Three positions have been investigated: the original 365 mm above the substrate, 110 mm above the substrate and 55 mm above the substrate. In Chapter 7 (or Ref. 14) we extensively discuss the influence of the SiH_4 injection position on the material properties.

In figure 9 the SiH_4 flow is varied for a hydrogen flow of 2000 sccm in the plasma source, and the crystalline mass fraction, the growth rate, and refractive index of the films are presented, as well as the SiH_4 depletion in the plasma. As can be noticed from figure 9a the SiH_4 flow at which the transition from *μc*-Si:H to *a*-Si:H occurs shifts to higher SiH_4 flows when the injection position is lowered. The refractive index does not seem to depend much on the SiH_4 flow. However, if we examine the films containing an equal crystalline mass fraction, for example 50%, then the refractive index increases from 3.1 to 3.3 if the injection position is decreased from

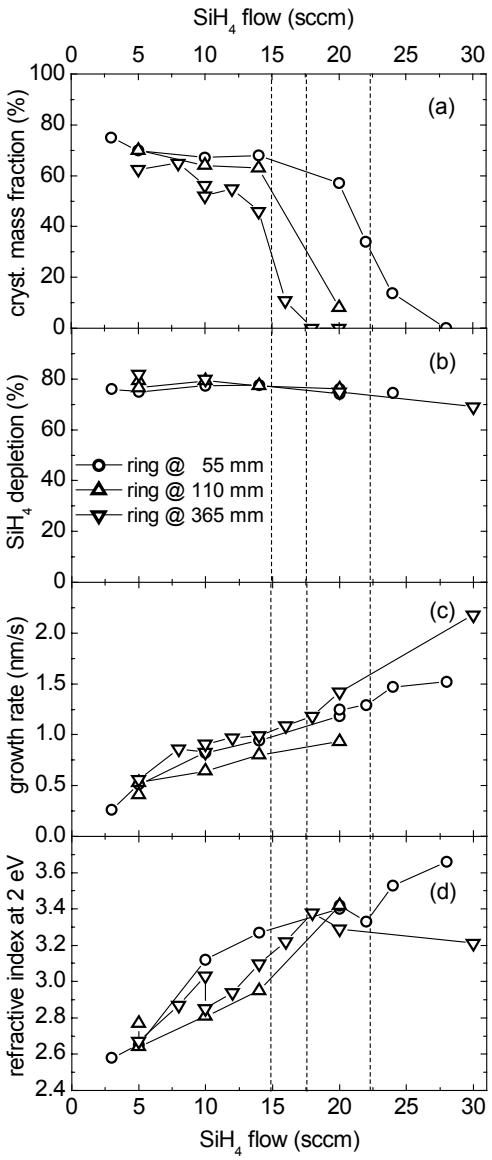

Figure 9. (a) The crystalline mass fraction, (b) SiH_4 depletion, (c) growth rate, and (d) the refractive index as a function of the SiH_4 flow. The cascaded arc plasma source is fed with a H_2 flow of 2000 sccm. Three different positions for the injection of SiH_4 into the expanding plasma are used. The numbers in the legend indicate the distance of the injection ring to the substrate. The dashed vertical lines indicate the transition between amorphous and microcrystalline silicon, taken at a crystalline mass fraction of 30%.

365 mm to 55 mm above the substrate. From these results it is concluded that lowering of the injection position improves the material density.

3.1.4. The optimum process parameters

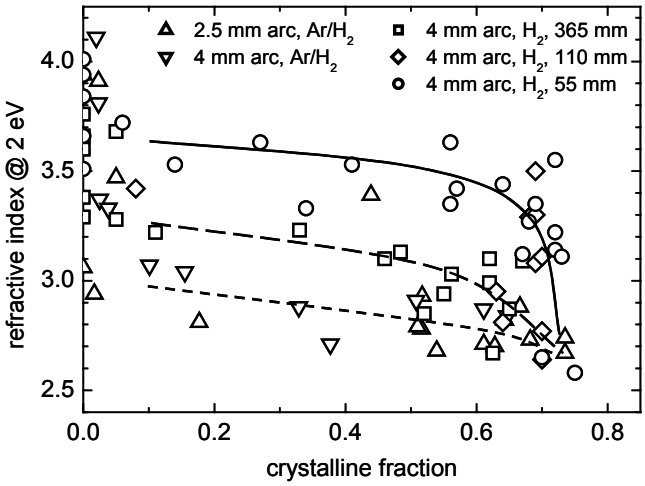

Figure 10. The refractive index at 2 eV versus the crystalline mass fraction for films deposited using a variety of process parameters, which are indicated in the legend (arc type, gas, distance SiH_4 injection point to substrate).

In figure 10 the refractive index at 2 eV is plotted versus the crystalline mass fraction for all films deposited using the 2.5-mm arc (Ar-H_2 mixture) and the 4-mm arc with an Ar-H_2 mixture, pure hydrogen, and pure hydrogen with the optimised injection position. This figure summarizes concisely the result of the process variation study described in the previous sections. The conditions with the plasma of an Ar-H_2 mixture give the lowest refractive index. Slightly higher values are obtained for the pure hydrogen plasma. The best material quality in terms of refractive index is obtained using a pure hydrogen plasma with the SiH_4 is injected closer to the substrate (at 110 mm or even at 55 mm from the substrate).

Furthermore, in this figure it can be observed that the refractive index decreases for crystalline mass fractions higher than 65%. This is particularly clear for material deposited with the pure hydrogen plasma with optimised injection position. Klein *et al.* [15] and Matsui *et al*. [16] also suggested a limited optimum crystalline mass fraction for application in solar cells. The closer the deposition conditions are chosen to the deposition regime where *a*-Si:H is obtained, the better the μc-Si:H material properties.

3.2. The material properties

3.2.1. Material structure

Having optimised the material on the refractive index, we want to know how dense the material finally has become. Moreover, since we know from FTIR experiments that the

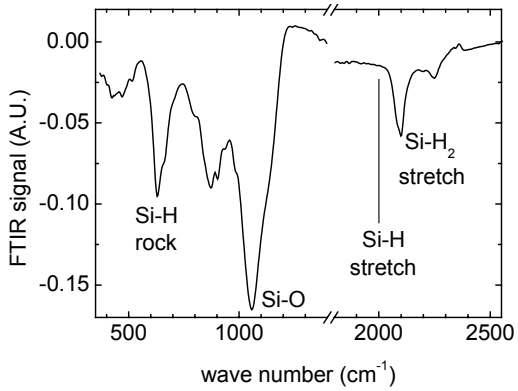

Figure 11. FTIR spectrum of a *μc*-Si:H film deposited at an optimized injection position and using 2000 sccm H_2 and 5 sccm SiH_4.

films contain a significant amount of oxygen (figure 11), the effect on the density will be quantified. We assume that this oxygen enters the film through pores in the material. These pores are indeed observed in transmission electron microscope (TEM) pictures (figure 12). The material shows a columnar structure, as can be observed in the SEM

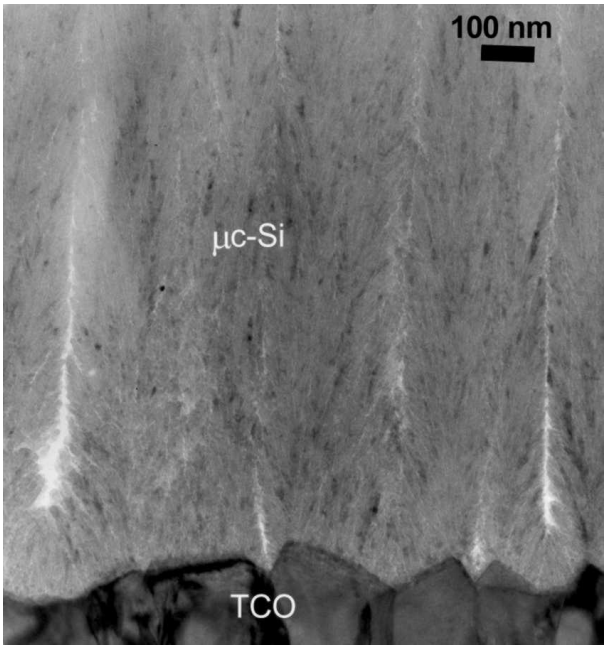

Figure 12. TEM bright field image of a p-i-n deposited solar cell on Asahi U-type TCO. The p and n doped *μc*-Si:H layers are 20 nm thick and the entire picture is about 1.2 μm high. The intrinsic layer is deposited using 2000 sccm H_2 and 10 sccm SiH_4.

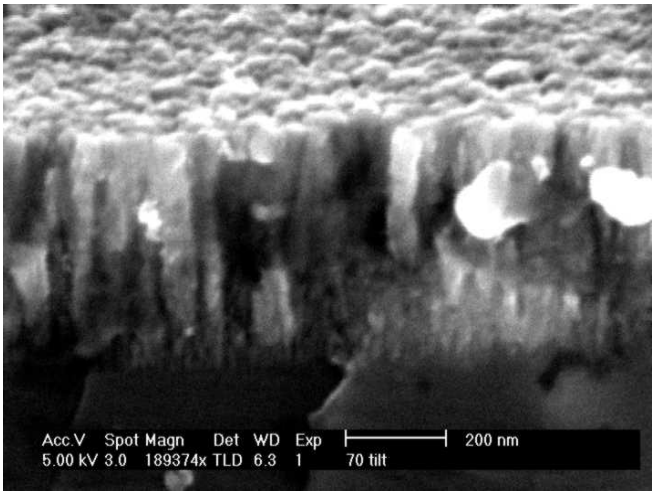

Figure 13. SEM picture of a μc-Si:H film deposited on c-Si wafer. Gas flows: 800 sccm Ar, 400 sccm H_2, and 2 sccm SiH_4. The film is cut and the picture is taken from the cutting edge at an angle of 20°.

image of figure 13. This type of structure is often observed for μc-Si:H growth with other techniques [17]. The elongated voids are probably situated between the columns.

For a more quantitative analysis of the voids in the films, we carried out an extended investigation of the material structure on two series of four films. The deposition conditions cover the transition regime between amorphous and microcrystalline silicon and a pure hydrogen plasma is used for both series. The first series is deposited using the non-optimised SiH_4 injection position (at 365 mm above the substrate) and the second series with the optimised injection position (55 mm above the substrate). Flotation density measurements [18] and SAXS measurements [19] are carried out, from which the void volume fraction is determined.

Table 1 summarizes the material structure of the films. The flotation-density measurements indicate that films deposited with the optimised SiH_4 injection-ring position generally have a slightly higher mass density, indicating a lower void fraction. Void volume fractions can be calculated from the flotation densities, the microcrystalline fractions (f_c-Raman in Table 1), and a correlation developed for the mass density of a-Si:H as a function of bonded H contents, C_H [18]: $\rho = 2.33 \cdot f_c + (2.29 - 0.0068 \cdot c_H)(1 - f_c)$. Comparison of these values with the experimental flotation densities yields the void fractions, f_v (flot.), listed in Table 1. These values do indicate slightly more compact materials for the optimised conditions. The SAXS results, however, show little difference for the optimised compared to the non-optimised injection positions, as shown in figure 14. An important single quantity extracted from the SAXS data is the integrated intensity [19], which is a good measure of the total inhomogeneity in each sample. The total scattering intensity is high compared to the device quality a-Si:H film (figure 14b) and this is known to be typical for μc-Si:H films [18]. Assuming spherical scattering objects (e.g., voids) a size

Table 1. Experimental results on the material structure. Q is the SiH_4 flow, f_c and f_v are the crystalline and void fractions, respectively, ρ is the mass density ('flot.' indicates that this is determined by flotation-density measurements), $\langle D \rangle$ is the average void size, n the refractive index, and L the average crystallite size determined by applying the Scherrer formula to the (111), (220), and (311) peak, respectively. Because a second peak was needed to fit the 220 peaks correctly for the lower sample series, two crystallite sizes are presented.

nr	Q (SiH_4) (sccm)	f_c XRD	f_c Raman	ρ (g/cm^3) flot.	f_v flot.	f_v SAXS	$\langle D \rangle$ (nm)	n at 2eV	c_H (at%)	L (111)	L (220)	L (311)	rate (nm/s)
Non-optimised injection													
#3	10	0.58	0.57	2.19	0.060	0.084	7.6	2.97	3.1	17.2	6.4	7.0	0.91
#4	14	0.50	0.46	2.20	0.056	0.071	8.1	3.10	5.9	10.1	5.5	7.0	0.99
#1	16	0.12	0.11	2.17	0.069	0.052	8.5	3.22	8.5	6.6	6.9	7.2	1.09
#2	18	0.00	0.00	2.17	0.069	0.063	8.0	3.38	7.8				1.18
Optimised injection													
#5	14	0.60	0.67	2.23	0.043	0.093	7.7	3.12	3.7	14.6	25/4.6	8.0	0.94
#6	20	0.60	0.59	2.22	0.047	0.076	7.6	3.30	4.1	12.3	20/4.7	7.5	1.18
#7	22	0.42	0.47	2.21	0.052	0.105	8.0	3.30	4.0	12.1	11/3.8	6.8	1.29
#8	28	0.00	0.00	2.18	0.064	0.062	7.8	3.65	7.6				1.52

distribution can be fitted to the data. The average object sizes obtained from the non-tilted samples are shown as $\langle D \rangle$ in Table 1. The significant drop in intensity for the tilted samples shows that oriented scattering objects that are elongated and aligned with the growth direction are found in all samples. This is confirmed by the TEM bright-field

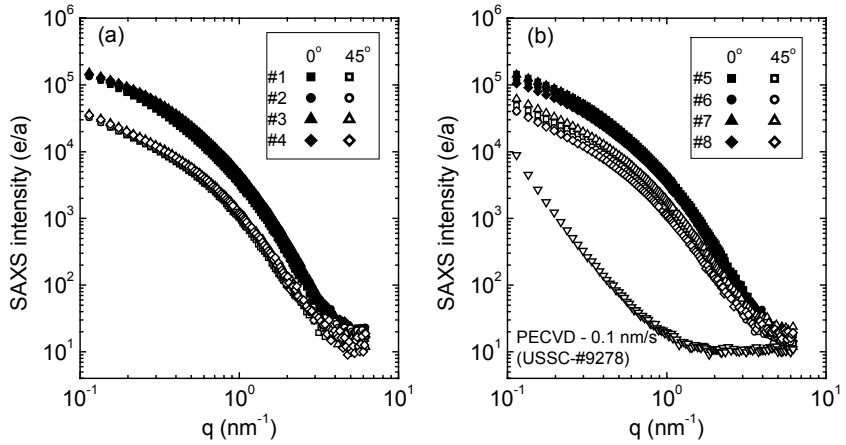

Figure 14. SAXS measurement of 5-μm thick silicon films deposited using (a) 10, 14, 16, and 18 sccm SiH_4 (nr. 3, 4, 1, and 2, respectively) injected into the reaction chamber at 365 mm above the substrate and (b) 14, 20, 22, and 28 sccm SiH_4 (nr. 5, 6, 7, and 8 respectively) injected at 55 mm above the substrate. Open symbols represent measurements with the sample tilted 45°. The momentum transfer $q = (4\pi/\lambda)\sin\theta$, where 2θ is the scattering angle and λ is the wavelength (0.154 nm). The unit for the scattering intensity is electrons/atom (e/a). For comparison in (b) the SAXS signal from a device-quality *a*-Si:H sample from USSC (now USOC, United Solar Ovonic Corporation) is shown.

image of sample #3 in figure 12. These kind of elongated, or crack-like, voids in μc-Si:H have been reported before for other deposition techniques [20]. Because of this anisotropic scattering a model based on ellipsoidal scattering objects is used to calculate the void fraction, assuming all scattering intensity is due to voids. Therefore, these values should be interpreted as an upper limit on the void fractions. Note from the table that these SAXS values of f_v are about a factor of two larger than those based on the flotation density. Other sources of inhomogeneity that could contribute to the SAXS are the μc-Si/a-Si:H density contrast and film surface roughness. The latter is known to be more significant for μc-Si:H than a-Si:H, but to increase with thickness for both types of material [21] (recall that these SAXS films were grown to 5-µm thickness). For the present films it is interesting that the fully amorphous samples (#2 and #8) show comparable SAXS to the μc-Si:H samples suggesting that the crystallites do not contribute strongly to the SAXS signals. Based on the complex shape of the voids seen in figure 12, the use of the simple ellipsoidal model may be a source of discrepancy in the void fractions determined by flotation and SAXS. Further details on the interpretation of SAXS measurements applied to these types of materials are described in Refs. 18 and 19.

From XRD measurements that were carried out on these samples we determined the crystallite size, L (see Table 1). The crystalline mass fraction is determined from these measurements using a method developed by Williamson [22]. The orientation of the crystal planes <111>, <220>, and <311> seems to be distributed randomly among the crystallites, as concluded from the area of the respective peaks. The particle sizes as determined from the width of the XRD peaks using the Scherrer formula vary with the crystal orientation. The results suggest that the crystallites grown in the (111) direction are about 12 nm large, versus 7 nm for the (220) and (311) crystal orientation. However, it is possible that due to some amorphous signal around the (111) scattering peak the determination of the (111) peak width is less accurate.

The hydrogen content and the bonding configuration have been determined from FTIR analyses on a series of samples. The hydrogen content is determined from the

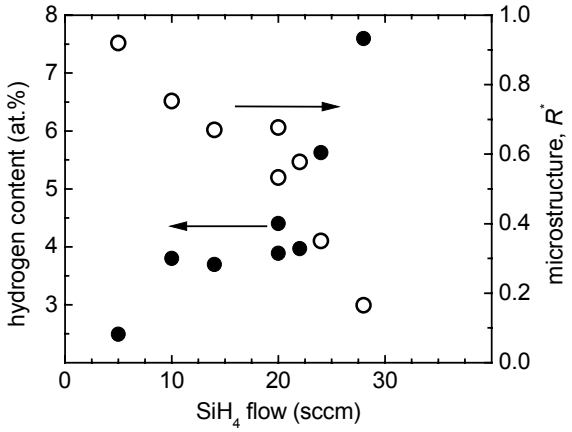

Figure 15. Hydrogen content and microstructure, R^*, for a series of samples deposited using a plasma of 2000 sccm of H_2 with optimized injection position.

area of the absorption peak at 640 cm^{-1} and the bonding configuration can be expressed in the microstructure parameter, R^* [23], which is the ratio of the integrated absorption of the stretching mode at 2100 cm^{-1} to the sum of those one at 2000 cm^{-1} and 2100 cm^{-1}. The result is shown in figure 15. When the crystalline mass fraction increases (on decreasing SiH_4 flow) the hydrogen content decreases, probably due to the simple fact that the crystalline mass fraction does not contain (much) hydrogen. The R^* for the samples with the highest crystalline mass fractions (lowest SiH_4 flows) is almost 1, indicating that the stretching mode at 2000 cm^{-1} is absent and most of the hydrogen is bonded in a SiH_2 configuration, probably on the grain boundaries. On decreasing the crystalline mass fraction R^* decreases below 0.2, which approaches the typical value of about 0.1 for high quality a-Si:H.

3.2.2. Electrical properties

The electrical properties are important for application of the films in electronic devices. In figure 16(a) and (b) the dark and the photoconductivity are shown for films deposited with an optimised injection position and with a hydrogen flow of 1500 and 2000 sccm, respectively, as a function of SiH_4 flow. The photoconductivity is rather independent (between 10^{-7} and 10^{-6} S/cm) of the SiH_4 flow, but the dark conductivity decreases with increasing SiH_4 flow to about 10^{-10} S/cm, as should be expected for *a*-Si:H. From the refractive index we know that the material becomes denser close to the transition to amorphous material and these films have a photoconductivity of 10^{-6} S/cm and 7×10^{-7} S/cm and a dark conductivity of 2×10^{-8} S/cm and 10^{-7} S/cm for a hydrogen flow of 1500 and 2000 sccm, respectively.

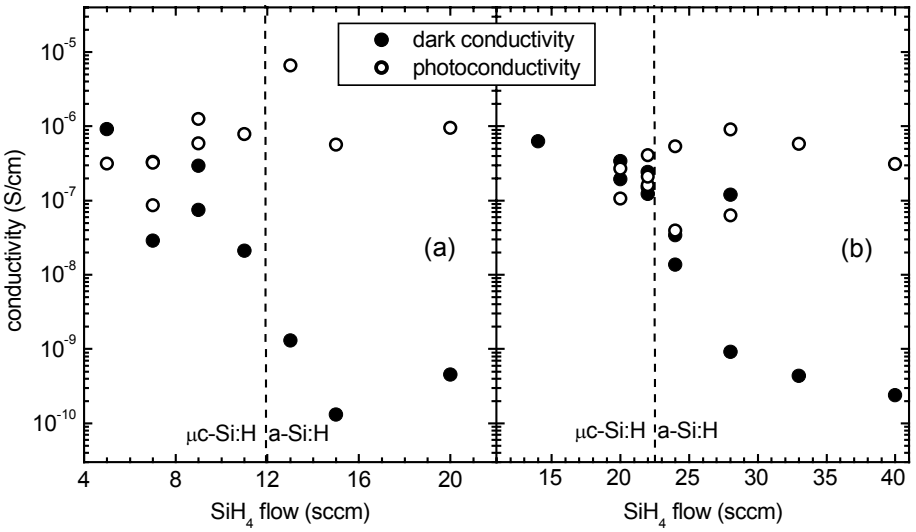

Figure 16. Photo and dark conductivity versus SiH_4 flow for a H_2 flow of (a) 1500 sccm and (b) 2000 sccm. The transition from *a*-Si:H to *μc*-Si:H occurs at (a) 11 sccm and (b) 20 sccm. A few sccm before that point the dark conductivity starts to decrease.

3.2.3. Optical properties

Light absorption spectra of *μc*-Si:H films are presented in figure 17. For comparison, the absorption curves of *a*-Si:H and *c*-Si are also shown. The curve of *c*-Si has a clear cut-off at 1.1 eV, the band gap of the material. For the *a*-Si:H film this cut-off is not so clear due to the sub-gap absorption, but the microcrystalline films do not have a real cutoff energy in the absorption at all. The absorption in the gap is significantly higher compared to high quality *a*-Si:H indicating a high defect density in the material. The sub-gap absorption seems to be the same for any of the presented films, having a range of amorphous and crystalline fractions. These defects apparently are not located in the amorphous fraction, because the sub gap absorption hardly depends on the fraction of amorphous material in the film.

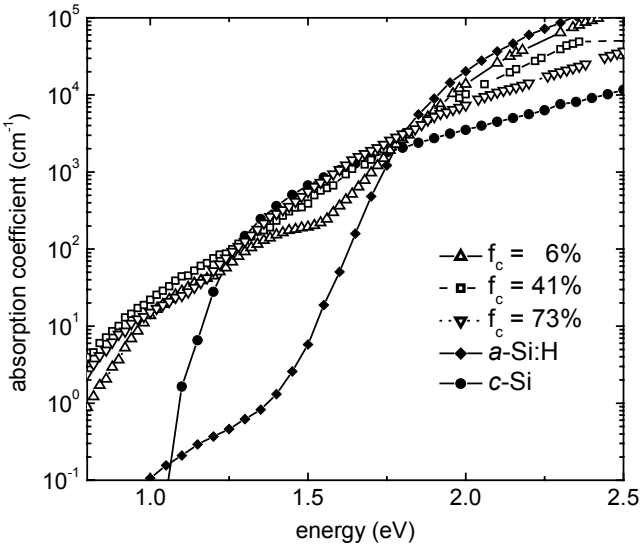

Figure 17. Absorption curves measured with reflection-transmission spectroscopy and dual-beam photoconductivity for a series of samples covering the transition from *a*-Si:H to *μc*-Si:H deposited with a plasma from 1500 sccm H_2 with optimised injection position. For comparison the absorption curves for *c*-Si and device quality *a*-Si:H are also shown.

3.3. Comparison of *μc*-Si:H deposited with ETP and with other techniques

A number of researchers report on the deposition of *μc*-Si:H at elevated growth rates and various techniques are explored. However, only a few articles report reasonable solar cell performance at growth rates of 1 nm/s and higher [e.g., 5, 7] (Table 2). One of the biggest challenges that most of the applied techniques have in common is deposit material with a compact structure [6, 24, this work]. Attempts to achieve this generally seem to converge to deposition conditions that are close to the *μc*-Si:H–to–*a*-Si:H transition regime. Material deposited in this regime mostly has moderate

Table 2. Comparison of material properties and solar cell results presented in this work with reported results obtained with other techniques: VHF (very high frequency) PECVD, HPD (high pressure depletion), and HW (hot wire) CVD. The properties that are compared are: the substrate temperature, T_s; the crystalline mass fraction, f_c; the crystallite size, D; the dominant crystal orientation, CO; the dark conductivity, σ_d; the photoconductivity, σ_{ph}; the dark-conductivity activation energy, E_{act}; the growth rate; the cell efficiency, η; and the hydrogen content, c_H. Note that in Ref. 6, 7, and 25 f_c is determined from the ratio of the Raman scattering signal intensity of the crystalline and the amorphous phase, whereas for the ETP CVD material the method described in Ref. 12 is used.

Method	Ref.	T_s (ºC)	f_c (%)	D (nm)	CO	σ_d (S/cm)	σ_{ph} (S/cm)	E_{act} (meV)	rate (nm/s)	η (%)	c_H (at.%)
VHF HPD	[25]		66 64			5×10^{-7} 2×10^{-7}		530 520	1.4 1.7		
VHF HPD	[7]								1.2	8.1	
VHF HPD triode	[7]		65			1×10^{-7}	1×10^{-5}		5.8		
VHF PECVD	[5]								0.7 1.0	7.8 6.9	
HW CVD	[6]		60 57 53	26 46	 220 220	8×10^{-8} 2×10^{-9}	2×10^{-5} 2×10^{-6}	530	1.4 0.44 1.3	 4.4	3.1 3.6
HW CVD	[25]	355 350			220 random				0.8 0.5	5.6 6.6	
HW CVD	[24]	185	55			10^{-6}	10^{-4}		0.09	9.4	
microwave	[27]	200			220				1.3	4.5	
ETP CVD	This work	250	71						0.21	1.9	
ETP CVD	This work	300	59	12	random	6×10^{-8}	2×10^{-6}	494	1.21	1.5	4.1

crystalline fractions of about 70% [6, 24, 25, 26, this work]. Often a (220) crystal orientation is found to be favourable for high material quality [6, 26, 27].

These general trends can be observed in Table 2, in which we compare the results obtained in this research to a selection of results reported in literature. A good comparison is difficult, though, for several reasons. First, most articles do not contain a complete list of all material properties. Second, the analysis of some of the properties is not unambiguous, for example electrical conductivity is mostly measured perpendicular to the growth direction, whereas in a solar cell the conduction parallel to the growth direction is relevant. Moreover, the conductivity of μc-Si:H often depends on the exposure time to air because of oxidation. Third, solar-cell efficiencies are strongly influenced by the device layout, for example absorber film thickness and the application of a back reflector.

3.4 Solar cells

When choosing process parameters for application in solar cells, and in devices in general, a trade off has to be found between material quality, growth rate, and deposition temperature. The material generally becomes better if higher substrate

temperatures are used, but the underlying part of the device often deteriorates at higher temperatures. Deposition parameters using high Ar flows therefore should be avoided, because then the plasma will heat the substrate, as has been demonstrated in section 3.1.1. Furthermore, in general for higher growth rates higher deposition temperatures are required in order to maintain the material quality.

From the study of the deposition parameters and the material properties described above it is concluded that the best μc-Si:H for application in solar cells is prepared with the precursor injection at 55 mm above the substrate and with the SiH_4 adjusted to be close to the transition to amorphous material. However, the SiH_4 flow at which the transition from microcrystalline deposition to *a*-Si:H might shift when the substrate temperature is changed. In order to determine the deposition parameters that should be used to be close to the transition to *a*-Si:H deposition, a series of layers have been deposited using different substrate temperatures. The result is shown in figure 18a and b: the SiH_4 flow at which the transition from microcrystalline to amorphous material takes place shifts to higher flows as the substrate temperature increases.

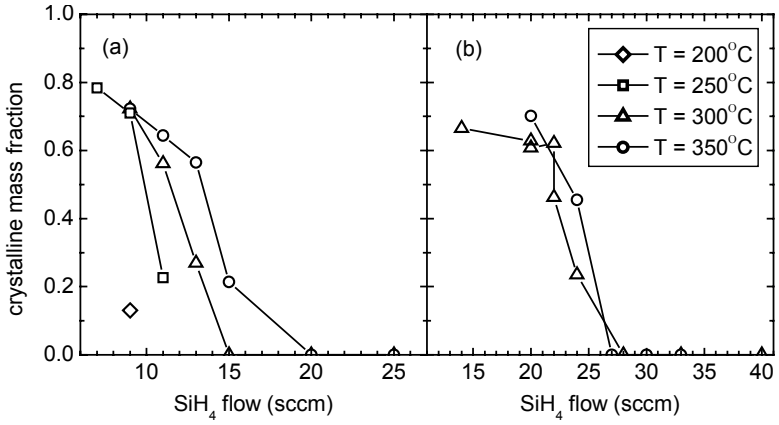

Figure 18. The SiH_4 flow at which the transition from μc-Si:H to *a*-Si:H occurs depends on the substrate temperature. The samples are deposited using a plasma of (a) 1500 sccm and (b) 2000 sccm H_2 with an optimised injection position.

Table 3. Deposition conditions and properties of films that have been incorporated in solar cells.

Film	H_2 flow (sccm)	SiH_4 flow (sccm)	Temp (°C)	Growth rate (nm/s)	Crystalline fraction	Refractive index at 2 eV
A	1500	9	250	0.21	0.71	3.41
B	1500	11	300	0.22	0.56	3.63
C	1500	13	350	0.23	0.57	3.79
D	2000	20	300	1.21	0.56	3.35
E	2000	22	300	~ 1.3	~ 0.35	~ 3.4
F	2000	22	350	~ 1.3	~ 0.58	~ 3.6

Table 4. The external solar-cell parameters of cells with a ETP CVD μc-Si:H intrinsic layer. The deposition conditions are presented in Table 3.

Intrinsic film	J_{sc} (A/m^2)	V_{oc} (V)	FF	η (%)
A, 1000 nm	66	0.41	0.51	1.4
A, 2000 nm	103	0.39	0.46	1.9
A, 3000 nm	63	0.42	0.32	0.8
B, 1000 nm	65	0.43	0.46	1.3
D, 1000 nm	69	0.36	0.50	1.3
D, 2270 nm	80	0.38	0.50	1.5
E, 1800 nm	79	0.40	0.34	1.1

In Table 3 the films are shown that have been incorporated in solar cells. The cells that have been prepared are deposited in a p-i-n sequence. We started using a deposition temperature of 250°C for the intrinsic layer. Because at these relatively low temperatures the material quality is expected to be the limiting factor, only a low deposition rate of about 0.2 nm/s is used. Three different intrinsic film thicknesses are used. The results of the external solar-cell parameters (short-circuit current density, J_{sc}, open-circuit voltage, V_{oc}, fill factor, FF, and conversion efficiency, η) are shown in Table 4. When the thickness is increased the fill factor decreases, because it is more difficult to collect the charge that is generated by the light absorption. However, if the cell is thicker, more light is absorbed. This is demonstrated by the increase in the short-circuit current density when the thickness is increases from 1000 to 2000 nm. When the thickness is increased even more, the current density decreases because of insufficient collection. At the optimum thickness of 2000 nm the efficiency is 1.86%, which is the highest efficiency that we have obtained so far with ETP deposited μc-Si:H solar cells.

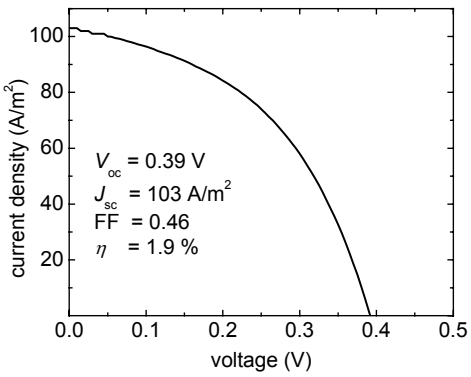

Figure 19. *J-V*-curve of a solar cell with a 2000 nm intrinsic film deposited with a plasma of 1500 sccm H_2 and 9 sccm SiH_4 using a substrate temperature of 250°C. The efficiency is 1.9%.

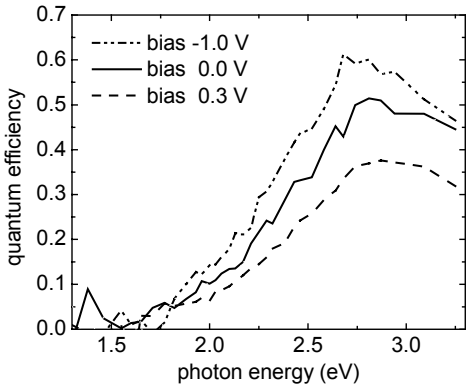

Figure 20. Spectral response measurement of the same solar cell as in Figure 19.

The *J-V* curve of the cell is shown in figure 19. In figure 20 the spectral response of this cell is shown for a number of bias voltages. The shape of the curve is typical for all the solar cells that are presented here. Especially photons in the low-energy range show a low quantum efficiency. This can partly be due to the fact that no high-reflective back contact is used and partly because there is still oxygen in the films, so that the charge is trapped before it is collected. Torres *et al*. [28] related the oxygen content in the intrinsic layer, due to a relatively high impurity concentration in the precursor gases, to a strongly reduced low-energy response.

Because the material properties are better if higher deposition temperatures are used, we tried to prepare p-i-n deposited cells in which the intrinsic film is deposited at 300°C. The result is shown again in Table 4. First, a cell with the intrinsic layer deposited at a relatively low deposition rate of 0.22 nm/s (material B) has been prepared, giving a conversion efficiency of 1.3%, then a higher deposition rate of 1.2 nm/s (material D) has been used, giving 1.3% and 1.5% efficiency for an intrinsic layer thickness of 1000 nm and 2270 nm respectively. For the growth rate of 1.2 nm/s a film with a lower crystalline fraction of 0.35 (material E) has been applied in a solar cell. The open-circuit voltage is higher, which is a known effect when the crystalline fraction is decreased [29]. The fill factor, however, decreases. Probably, the current conduction is not good enough at these low amounts of crystalline material in the film, which results in an insufficient charge carrier collection. Apparently the crystalline mass fraction is too low in this cell. It should be realized that the crystalline mass fraction of the intrinsic film in the cells does not necessarily equal the crystalline mass fraction in the individual film deposited on glass.

Future work should reveal whether ETP CVD of μc-Si:H deposited at rates in excess of 1-2 nm/s can be achieved. It should be realized that the solar cells presented here are first trials and no optimisation of film thickness or crystalline mass fraction has been attempted. Actually, there is a lot of room for further improvement of the film quality. For example, optimising the position of SiH_4 injection could improve the material quality even more, although it is required to get a better fundamental understanding of this effect [14]. We already observed that the solar cell efficiency increased after we switched the H_2 gas purity from 4.5 to 5.6. A H_2 gas purifier should be installed to reduce the oxygen contamination. It is necessary to pay more attention to the material properties of the absorber layer in the cells, e.g., the charge carrier diffusion lengths and defect density [30]. The preliminary solar-cell results described in this paper, however, show that ETP CVD is a promising technique for the deposition of μc-Si:H for solar cells at high rates, but more research is needed to address the potential fully.

4. Conclusions

ETP CVD is used to deposit μc-Si:H films. Deposition parameters like the gas flows, the substrate temperature, the precursor injection position, and even the plasma source are varied to optimize the material properties for application in solar cells. A pure hydrogen plasma is found to be advantageous for the material quality compared to a mixture of argon and hydrogen. The injection of the precursor SiH_4 into the expanding

plasma should be preferably located at about 55 mm above the substrate for the deposition conditions used in this work. Furthermore, deposition conditions that result in microcrystalline material close to the transition to amorphous material seem to be favourable, in agreement with other studies.
A refractive index at 2 eV of 3.4 to 3.8 is obtained for a substrate temperature varying from 250°C to 350°C at a growth rate of 0.2 nm/s. For an increased growth rate of 1.2 nm/s the refractive index varies from 3.3 to 3.6 for the given temperature range. Still, the films show some porosity. The photo and the dark conductivity under optimised conditions is about 10^{-6} S/cm and 5×10^{-8} S/cm, respectively. These materials are incorporated in solar cells giving conversion efficiencies of 1.9% and 1.5% at a growth rate of 0.2 nm/s and 1.2 nm/s, respectively. These preliminary results indicate that ETP CVD is a promising technique for the deposition of μc-Si:H for solar cells at elevated deposition rates, although further research remains necessary.

Acknowledgements

The Department of Chemical Technology, section R&CE, of the Delft University of Technology is acknowledged for the use of their Raman microscope. We thank Niek van de Pers for the XRD analysis (figure 5). Thanks to Ries van de Sande and Jo Jansen for the design and the construction of the laboratory set-up. Thanks to Martijn Tijssen for the technical support and Arjan Driessen for the support on the sample analysis. Dr. W. M. M. Kessels is thanked for scientific discussions. The research at Colorado School of Mines was supported by the National Renewable Energy Laboratory, USA. Novem is acknowledged for the financial support.

References

[1] W. M. M. Kessels, R. J. Severens, A. H. M. Smets, B. A. Korevaar, G. J. Adriaenssens, D. C. Schram, M. C. M. van de Sanden, J. Appl. Phys. **89**, 2404 (2001).

[2] B. A. Korevaar, A. M. H. N. Petit, C. Smit, R. A. C. M. M. van Swaaij, M. C. M. van de Sanden, in: Proceedings of the 29th IEEE Photovoltaic Specialists Conference, New Orleans, U. S. A., May 20-24, 2002, p. 1230.

[3] J. Meier, S. Dubail, D. Fischer, J. A. Anna Selvan, N. Pellaton Vaucher, R. Platz, Ch. Hof, R. Flückiger, U. Kroll, N. Wyrch, P. Torres, H. Kepner, A. Shah, K.-D. Ufert, in: W. Freiesleben, W. Palz, H. A. Ossenbrink, P. Helm (Eds.), Proceedings of the 13th European Photovoltaic Solar Energy Conference, Nice, France, October 23-27, 1995, p. 1445.

[4] T. Roschek, T. Repmann, J. Müller, B. Rech, H. Wagner, in: Proceeding of the 28th IEEE Photovoltaic Specialists Conference, Anchorage, U. S. A., September 18-22, 2000, p. 150.

[5] L. Feitknecht, O. Kluth, Y. Ziegler, X. Niquille, P. Torres, J. Meier, N. Wyrsch, A. Shah, Sol. Energy Mater. Sol. Cells **66**, 397 (2001).

[6] J. K. Rath, A. J. Hardeman, C. H. M. van der Werf, P. A. T. T. van Veenendaal, M. Y. S. Rusche, R. E. I. Schropp, Thin Solid Films **430**, 67(2003).

[7] M. Kondo, Sol. Energy Mater. Sol. Cells **78**, 543 (2003).

[8] B. A. Korevaar, C. Smit, R. A. C. M. M. van Swaaij, A. H. M. Smets, W. M. M. Kessels, J. W. Metselaar, D. C. Schram, M. C. M. van de Sanden, in: H. Scheer, B. McNelis, W. Palz, H. A. Ossenbrink, E. Dunlop, P. Helm (Eds.), Proceedings of the 16th European Photovoltaic Solar Energy Conference, Glasgow, U. K., May 1-5, 2000, p. B119.

[9] M. C. M. van de Sanden, R. J. Severens, W. M. M. Kessels, R. F. G. Meulenbroeks, D. C. Schram, J. Appl. Phys. **84**, 2426(1998).

[10] S. Mazouffre, M. G. H. Boogaarts, I. S. J. Bakker, P. Vankan, R. Engeln, D. C. Schram, Phys. Rev. E **64**, 016411 (2001).

[11] E. A. G. Hamers, A. H. M. Smets, C. Smit, J. P. M. Hoefnagels, W. M. M. Kessels, M. C. M. van de Sanden, in: M. Stutzmann, J. B. Boyce, J. D. Cohen, R. W. Collins, J. Hanna (Eds.), Amorphous and Heterogeneous Silicon-based Films, San Francisco, U. S. A., April 16-20, 2001, Materials Research Society Symposium Proceeding 664 (2001) A4.2.1.

[12] C. Smit, R. A. C. M. M. van Swaaij, H. Donker, A. M. H. N. Petit, W. M. M. Kessels, M. C. M. van de Sanden, J. Appl. Phys. **94**, 3582 (2003).

[13] R. E. I. Schropp, M. Zeman, Amorphous and microcrystalline silicon solar cells, Kluwer Academic Publishers, Dordrecht, the Netherlands, 1998.

[14] C. Smit, R. A. C. M. M. van Swaaij, E. A. G. Hamers, M. C. M. van de Sanden, J. Appl. Phys. **96**, 4076 (2004).

[15] S. Klein, J. Wolff, F. Finger, R. Carius, H. Wagner, M. Stutzmann, Jpn. J. Appl. Phys. **41**, L10 (2002).

[16] T. Matsui, M. Tsukiji, H. Saika, T. Toyama, H. Okamoto, Jpn. J. Appl. Phys. **41**, 20 (2002).

[17] L. Houben, M. Luysberg, P. Hapke, R. Carius, F. Finger, H. Wagner, Phil. Mag. A **77**, 1447 (1998).

[18] D. L. Williamson, Sol. Energy Mater. Sol. Cells **78**, 41 (2003).

[19] D. L. Williamson, in: M. Hack, E. A. Schiff, A. Madan, M. Powell, A. Matsuda (Eds.), Amorphous Silicon Technology, San Francisco, U. S. A., April 18-21, 1995, Materials Research Society Symposium Proceeding 377 (1995) 251.

[20] J. Meier, S. Dubail, U. Kroll, S. Faÿ, E. Vallat-Sauvain, L. Feitknecht, J. Dubail, A. Shah, Sol. Energy Mater. Sol. Cells **74**, 457 (2002).

[21] R. W. Collins, A. S. Ferlauto, G. M. Ferreira, C. Chen, J. Koh, R. J. Koval, Y. Lee, J. M. Pearce, C. R. Wronski, Sol. Energy Mater. Sol. Cells **78**, 143 (2003).

[22] D. L. Williamson, in: H. M. Branz, R. W. Collins, H. Okamoto, S. Guha, R. Schropp (Eds.), Amorphous and Heterogeneous Silicon Thin Films: Fundamentals to Devices, San Francisco, U. S. A., April 5-9, 1999, Materials Research Society Symposium Proceeding 557 (1999) 251.

[23] A. H. Mahan, P. Raboisson, R. Tsu, Appl. Phys. Lett. **50**, 335 (1987).

[24] S. Klein, F. Finger, R. Carius, T. Dylla, B. Rech, M. Grimm, L. Houben, M. Stutzmann, Thin Solid Films **430**, 202 (2003).

[25] U. Graf, J. Meier, U. Kroll, J. Bailat, C. Droz, E. Vallat-Sauvain, A. Shah, Thin Solid Films **427**, 37 (2003).

[26] E. Iwaniczko, Y. Xu, R. E. I. Schropp, A. H. Mahan, Thin Solid Films **430**, 212 (2003).

[27] G. Ohkawara, M. Nakajima, H. Uejama, H. Shirai, Thin Solid Films **427**, 27 (2003).

[28] P.Torres, J. Meier, R. Flückiger, U. Kroll, J. A. Anna Selvan, H. Keppner, A. Shah, S. D. Littlewood, I. E. Kelly, P. Giannoulès, Appl. Phys. Lett. **69**, 1373 (1996).

[29] S. Klein, F. Finger, R. Carius, B. Rech, L. Houben , M. Luysberg, M. Stutzmann, in: J. D. Cohen, J. R. Abelson, H. Matsumura, J. Robertson, Amorphous and Heterogeneous Silicon Thin Films: Fundamentals to Devices, San Francisco, U. S. A., April 2-5, 1999, Materials Research Society Symposium Proceeding **715**, A26.2.1 (2002).

[30] V. L. Dalal, J. H. Zhu, M. Welsh, M. Noack, IEE Proc.-Circuits Devices Syst. **150**, 316 (2003).

Chapter 7

The role of the silyl radical in plasma deposition of microcrystalline silicon

C. Smit[1,2], R.A.C.M.M. van Swaaij[2], E.A.G. Hamers[1], and M.C.M. van de Sanden[1]

[1] Eindhoven University of Technology, Department of Applied Physics, P. O. Box 513, 5600 MB Eindhoven, the Netherlands
[2] Delft University of Technology, DIMES-ECTM, P. O. Box 5053, 2600 GB Delft, the Netherlands

J. Appl. Phys. **96**, 4079 (2004)

Abstract

Expanding thermal plasma chemical vapor deposition (ETP CVD) has been used to deposit microcrystalline silicon films. We studied the behavior of the refractive index, crystalline fraction and growth rate as a function of the silane (SiH_4) flow close to the transition from amorphous to microcrystalline silicon. It was found that the refractive index, a measure for film density, increases when the average sticking probability of the depositing radicals decreases. Furthermore, we studied the influence of the position at which SiH_4 is injected in the expanding plasma on the film density. It was found that the film density becomes higher when the SiH_4 is injected closer to the substrate. Both findings strongly suggest that the film density benefits from a high contribution of the SiH_3 radical to the growth of microcrystalline silicon.

1. Introduction

Thin silicon films are widely applied in large area electronic devices like flat displays and solar cells. Hydrogenated amorphous silicon (*a*-Si:H) has already been studied and applied since 1965 [1]. Quite some knowledge has been gained about the deposition mechanisms and the optimum plasma chemistry [2,3,4,5,6]. It is now widely agreed that the SiH_3 radical plays an important role in the deposition process of high quality *a*-Si:H [4,7]. A higher surface mobility is often suggested as one of the reasons [8,9,10]. Hydrogenated microcrystalline silicon (*μc*-Si:H) has become popular for application in large area electronics about ten years ago. There is still a lot of debate about the growth mechanism and several growth mechanisms have been proposed, many of them inspired on the successful growth model of *a*-Si:H [11,12,13]. It is not yet clear what the optimum deposition plasma chemistry should look like and which radicals contribute favorably to the growth of high quality *μc*-Si:H.

The industry standard for the production of thin silicon films is radio-frequent plasma enhanced chemical vapor deposition (RF PECVD), but other techniques have been developed, mainly with the aim to increase the growth rate. Very high frequency (VHF) PECVD [14], hot wire (HW) CVD [15,16], and electron cyclotron resonance (ECR) PECVD [17] are some of the alternative techniques investigated. In this paper *μc*-Si:H films have been prepared using expanding thermal plasma (ETP) CVD [18]. ETP CVD is a remote plasma deposition technique in which the plasma generation takes place in a relatively high-pressure chamber (the cascaded arc plasma source), separate from the plasma chemistry that takes place when the precursor is injected in the low-pressure process chamber. This simplifies the chemistry to such an extent that ETP CVD is a suitable plasma deposition technique for the investigation of the influence of the plasma chemistry on the film deposition. This has been demonstrated in particular for ETP CVD of *a*-Si:H [6], *a*-C:H [19], and *a*-$SiO_xC_yH_z$ [20].

The deposition of thin silicon films with RF/VHF PECVD, HW CVD, and ETP CVD all rely on the decomposition of the precursor gas silane (SiH_4) into radicals and ions that eventually stick to the substrate surface where film growth occurs. The decomposition mechanism of SiH_4 is totally different for the three deposition techniques mentioned. In RF/VHF PECVD electrons gain kinetic energy driven by the alternating electric field that is applied between two parallel electrodes and the SiH_4 molecules are dissociated by electron impact [21] In HW CVD the SiH_4 molecules are dissociated by a catalytic reaction at hot tungsten or tantalum wires. In ETP CVD, a beam of atomic hydrogen is created that interacts with the SiH_4 molecules injected downstream. In this way hydrogen abstraction reactions dominate the dissociation of SiH_4 and it depends on the surplus of hydrogen and the path length to the substrate to what extent subsequent abstraction reactions are capable of creating the various silane radicals [5]:

$$SiH_4 + H \rightarrow SiH_3 + H_2 \quad (1)$$
$$SiH_3 + H \rightarrow SiH_2 + H_2 \quad (2)$$
$$SiH_2 + H \rightarrow SiH + H_2 \quad (3)$$
$$SiH + H \rightarrow Si + H_2 \quad (4)$$

The reaction rates of these reactions can be found in Refs. 22 and 23. Note that we neglect radical-radical as well as radical-silane reactions because we only consider here high dilution conditions to deposit *μc*-Si:H. Furthermore, radical-H_2 reactions are neglected since the reaction rate is very small. Since the H_2-dilution is high, reactions involving ions can be neglected too ($< 10^{16}$ m^{-3}) [24].

It has been demonstrated that for the deposition of high-quality *a*-Si:H it is required that the flux of SiH_3 radicals towards the substrate dominates the deposition. In the deposition of high quality *a*-Si:H with ETP CVD this is realized as follows. The SiH_4 flow is set at a higher value than the flow of atomic hydrogen from the plasma source. The atomic hydrogen created in the cascaded arc plasma source is totally consumed by the first hydrogen abstraction reaction Eq. (1) with the relatively high density of SiH_4 [5,25]. Under these conditions subsequent reactions of SiH_3 with atomic hydrogen are suppressed and a dominant SiH_3 beam is generated. The latter is confirmed by means of cavity ring down spectroscopy (CRDS) and Threshold Ionization Mass Spectrometry measurements [25].

It is generally accepted that for the deposition of *μc*-Si:H atomic hydrogen is essential at the surface of the growing film to enhance crystallization [3, 26, 27]. Therefore, commonly the gas flows are adjusted to a high (1-5%) dilution of the SiH_4 in H_2, irrespective of the deposition technology. In RF PECVD the high energy electrons also dissociate H_2. In HW CVD H_2 is catalytically dissociated at the tungsten or tantalum wire. In ETP CVD increasing the H_2 flow in the cascaded arc plasma source results in a higher atomic hydrogen flow into the reaction chamber and a simultaneous decrease in SiH_4 flow leads to a lower consumption of H by SiH_4. Both effects result in a higher H flux at the surface of the growing film. As a consequence of the high atomic hydrogen density in the reaction chamber the depletion of SiH_4 is very high and can even reach 100% [18]. Furthermore, subsequent hydrogen abstraction reactions will take place, creating SiH_x with $x < 3$. This is clearly illustrated by CRDS measurements by Hamers *et al.*, in which the SiH_4 flow is varied for constant Ar and H_2 flow [28].

In general, *μc*-Si:H, especially when deposited at higher deposition rates and at lower temperatures, is porous to some extent, decreasing the applicability in solar cells. This characteristic we have discussed in another article [29] and in Chapter 6. In principle, apart from crystallite size, there will be no difference in the quality of the crystalline silicon phase in microcrystalline silicon. It is the amorphous phase between the crystallites that contains the pores and has a varying defect density. This suggests that the quality of *μc*-Si:H can be improved when SiH_3 radicals dominate the deposition of microcrystalline silicon, because the amorphous phase between the crystallites will be of better quality, similar to the case of entirely hydrogenated amorphous silicon films. Figure 1, in which we plotted the *μc*-Si:H refractive index at a photon energy of 2 eV versus the SiH_4 depletion for various arc and reactor chamber settings, corroborates more or less this hypothesis. If the SiH_4 depletion is close to 100%, the reaction chain Eq. 1 to Eq. 4 goes to full completion leading to a distribution of high sticking radicals, and this is accompanied by a low refractive index.

In this paper we will discuss two additional observations to figure 1, which were obtained during the systematic variation of the process conditions to achieve better quality *μc*-Si:H (see Chapter 6 or reference 29). This discussion might give a leading

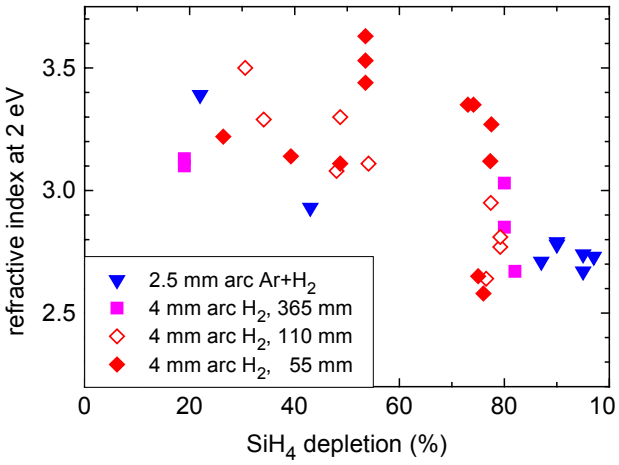

Figure 1. The refractive index at 2 eV versus the SiH4 depletion for various arc and process parameter settings. The legend indicates the type of plasma source, the applied gas mixture in the plasma source, and the distance of the SiH4 injection to the substrate (see section Experimental set-up and procedures). Only the films with a crystalline fraction of 0.4 and higher are selected.

principle in obtaining even better quality *μc*-Si:H in the near future. The first observation is related to the behavior of the refractive index, crystalline fraction and growth rate as a function of the SiH_4 flow, in particular close to the *a*-Si:H/*μc*-Si:H transition. The other observation discussed is related to the effect of varying SiH_4 injection ring position on the quality of the *μc*-Si:H.

We first describe the ETP-CVD set up and the film diagnostics employed. Subsequently the results are presented and discussed. As we will argue, the implications of the observations strongly suggest the beneficial role of the SiH_3 radical in the deposition of *μc*-Si:H. Finally the conclusions are presented.

2. Experimental set-up and procedures

The CASCADE set-up is designed to prepare thin film silicon solar cells in which the absorber layer is deposited using ETP CVD [30]. It consists of a load lock, a RF PECVD chamber for the deposition of the doped layers, and a reaction chamber for the deposition of silicon films with ETP CVD. In figure 2 a schematic representation is shown of the ETP part of the CASCADE set-up. This deposition technique has been extensively described elsewhere [31]; below we will give a brief summary and give the relevant process parameters that are varied.

On top of the ETP reaction chamber is the cascaded arc plasma source. This source generates a plasma between three cathodes and an anode plate at a DC discharge current of 50 A at a pressure of about 0.1 bar. Two different geometries for the cascaded-arc plasma source have been employed. The first one consists of six copper cascade plates building up a discharge channel of 30 mm long with a diameter of

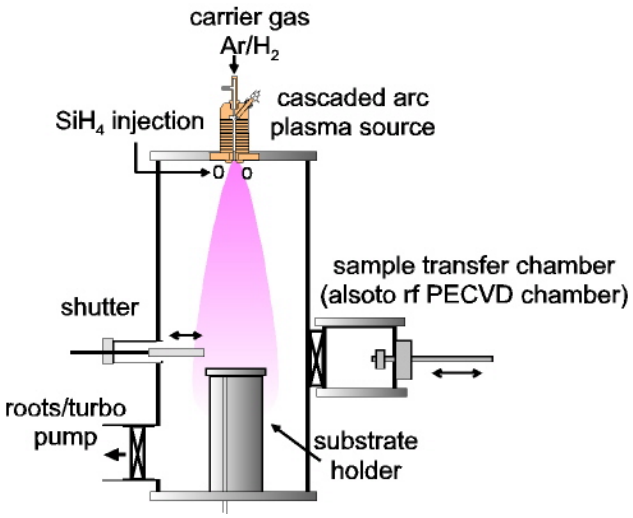

Figure 2. The ETP CVD chamber of the CASCADE set-up. On top is the cascaded arc plasma source, which can be fed with different gases. In this case H_2 or an Ar/H_2 mixture is used (100-300 mbar). The plasma expands into the reaction chamber (~ 0.2 mbar) and downstream the precursor gas SiH_4 is injected. The silicon film is deposited on the substrate, which is on a temperature-controlled holder. A shutter is used in order to start the deposition at stable plasma conditions. On the side of the reaction chamber, below the substrate, the pump line is situated. A valve on the other side of the chamber opens the way to the load lock and the RF PECVD chamber.

2.5 mm. The advantage of this source is that it can be operated at relatively low gas flows (typically 600 sccm Ar and 200 sccm H_2) and therefore a low pump capacity is sufficient to obtain the required process pressure of about 0.2 mbar. This source, referred to as the 2.5-mm arc, cannot be operated on hydrogen gas only, but a minimum argon flow of twice the hydrogen flow must be added. In this research this source is always operated at an argon-hydrogen flow ratio of 2:1 because for the deposition of microcrystalline silicon the hydrogen dilution is important. In order to be able to operate a pure hydrogen plasma a source with a different geometry is installed. The discharge channel is now created by four copper cascade plates with holes having a diameter of 4 mm forming a central channel about 20 mm long. This source, referred to as the 4-mm arc, is operated at 2000 sccm H_2. The substrate is positioned 410 mm below the plasma source exit. The substrate temperature is 300ºC throughout this work, unless stated otherwise.

After leaving the nozzle of the cascaded arc the plasma expands supersonically into the reaction chamber, which is at a pressure of about 0.25 mbar. The expanding plasma shocks when it collides with the background gas after which it flows towards the substrate with a velocity that gradually decreases to about 100 to 200 m/s right above the substrate. The precursor gas, SiH_4, is injected into the expanding plasma through a ring-shaped (80 mm diameter) gas line, which is concentric with the reaction chamber, with holes (1 mm diameter) pointing to the axis of the reaction chamber. The

atomic hydrogen in the plasma dissociates the SiH_4 molecules into radicals [5], which deposit at the substrate at 410 mm below the plasma source exit. The consumption of the SiH_4 by the hydrogen plasma is measured with a mass spectrometer that is mounted on the side of the reactor at the substrate level.

Using the 2.5-mm arc fed with 1200 sccm Ar and 600 sccm H_2 a series of samples has been prepared with varying SiH_4 flow in order to investigate the behavior of the refractive index, crystalline fraction and growth rate close to the *a*-Si:H/μc-Si:H transition. A second series of samples has been prepared using the 4-mm arc fed with 2000 sccm of H_2 to investigate the influence of the position of the injection ring. Three injection ring positions have been employed, 365 mm, 110 mm, and 55 mm above the substrate (for brevity referred to as high, middle, and low injection ring position), and for any of these positions the SiH_4 flow is varied from 5 to 25 sccm. The same deposition series is repeated using a hydrogen gas flow of 1500 sccm and the injection ring at the high and the low position. The layers are simultaneously deposited on Corning 1737 glass substrates and n-type crystalline Si wafers. Care was taken to have the thickness of all films in the range of 650 to 750 nm. The films are analyzed using reflection-transmission spectroscopy to determine the thickness and the refractive index at a photon energy of 2 eV. Raman spectroscopy was used to determine the crystalline fraction in the microcrystalline films as described previously (Chapter 4, reference 32).

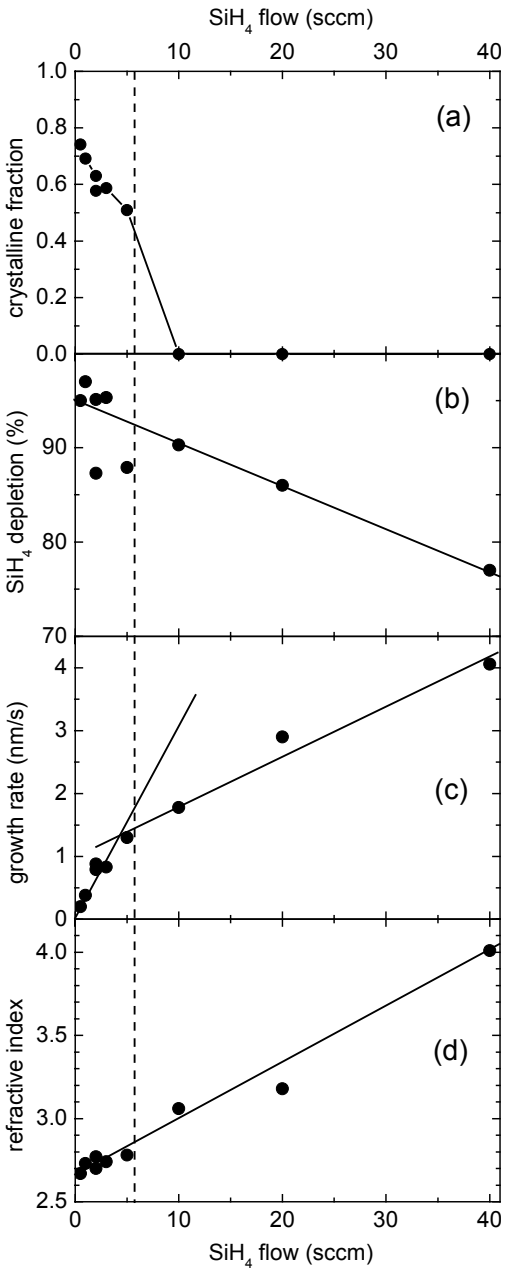

Figure 3. (a) The crystalline fraction, (b) SiH_4 depletion, (c) growth rate, and the (d) refractive index at 2 eV as a function of SiH_4 flow. The Ar and the H_2 flows are set at 1200 and 600 sccm, respectively. The vertical dashed line indicates the transition between amorphous and microcrystalline silicon.

3. Results and discussion

3.1. SiH_4 variation

In most PECVD techniques there is a threshold dilution R ($R = H_2/(H_2+SiH_4)$) for the deposition of μc-Si:H (e.g., reference 33). In figure 3 the results of the film series deposited using the 2.5-mm arc are shown. From the crystalline fraction in figure 3a the transition region between amorphous and microcrystalline material can be determined at a SiH_4 flow somewhere in between 5 and 10 sccm, as is indicated by the dashed vertical line. In figure 3b the depletion is shown as a function of SiH_4 flow. For small SiH_4 flows (< 3 sccm) the depletion is almost 100%, because there is a surplus of H available in the plasma to dissociate all the injected SiH_4 (H_2 dissociation degrees of 0.3% [34] and 4% [Chapter 3 or reference 35] have been reported for a Ar/H_2 ratio of 6/1 and for a pure H_2 plasma, respectively. For an H_2 flow of 600 sccm this corresponds to an H flow of about 1.8 sccm and 24 sccm, respectively. The H flow in this case with an Ar/H_2 ratio of 2 is expected to be in between these two flows). When the SiH_4 flow increases the depletion decreases because gradually there is not enough H to decompose all SiH_4. In figure 3c the deposition rate is shown as a function of SiH_4 flow. As the SiH_4 flow increases the growth rate increases because more depositing radicals are created. Note that there seem to be two distinct slopes in the graph: a steep slope for the data points with low SiH_4 flow (≤ 3 sccm) and a less steep slope for the higher flows.

The observation of the different slopes might be interpreted as follows. First, it could be argued that this is due to varying mass density of the films, which is suggested by the varying refractive indices in figure 3d. To exclude this, the mass density of the films is calculated using the infrared refractive index, the hydrogen content and the crystalline fractions [36]. From the mass density, the thickness and deposition time the growth flux can be estimated. Furthermore, the SiH_4 flow multiplied by the depletion (figure 3b) will give the rate at which radicals (SiH_x with $0 \leq x < 4$, we neglect the production of higher radicals Si_nH_m with $n > 1$) are produced and that is eventually deposited. These two quantities are plotted in figure 4. The slope of the line through the data points in this graph indicates the number of Si atoms incorporated in the film per created SiH_x radical ($0 \leq x < 4$). This means that the slope is proportional to an effective, or averaged, sticking probability. In figure 5 we calculated the ratio of the growth flux and the radical production rate as a function of the SiH_4 flow. The values plotted in figure 5 are proportional to the sticking probability. It is clear that the sticking probability is much higher for low SiH_4 flows than for high SiH_4 flows. This is due to the fact that for low SiH_4 flows follow-up hydrogen abstraction reactions creating SiH_x with $0 \leq x < 3$ are more likely and these radicals have sticking probabilities which are close to 1 [10, 37]. The values given in figure 5 do not directly correspond with the averaged sticking probability on the substrate. Material is also deposited on the walls of the reactor, although probably at lower rates than at the substrate. Therefore the effective deposition area is larger than the substrate size of 100 cm^2 that is used in the calculation of the growth flux. However, this geometrical factor will be constant as long as only the SiH_4 flow is varied since the plasma

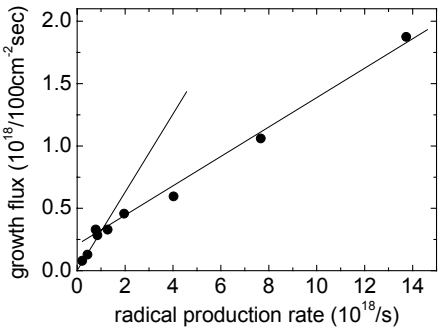

Figure 4. The growth flux, calculated from the growth rate and the mass density of the film, as the number of particles that is deposited on the 100-cm^2 substrate in a second, versus the total rate of radicals that are produced from the SiH_4 in the reaction chamber, which is equal to the product of the depletion and the SiH_4 flow. The slope of the graph is related to the sticking coefficient. Only a geometrical factor is missing, because deposition also takes place on the reactor walls.

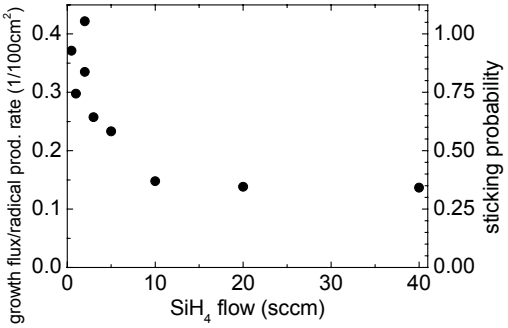

Figure 5. The growth flux divided by the radical production rate is proportional to the sticking probability. Therefore a decrease can be observed for increasing SiH_4 flow because at higher SiH_4 flows less high sticking radicals are produced. On the right axis the scale is normalized to set the sticking coefficient for low SiH_4 flows to 1.

expansion properties, and with it the spatial distribution of the radicals in the reaction chamber, remain unaltered.

We can go a step further by making an additional assumption for low SiH_4 flow. Under these conditions we assume that the SiH_4 is entirely stripped of all hydrogen, i.e., the deposition is dominated by the silicon radical, which has a measured sticking coefficient of 1 [10,37]. Since we find values of about 0.4/100 cm^2 in figure 5, a scaling factor of 2.5 should be introduced that corrects for the effective, growth-rate weighed, deposition area. This scaling factor is introduced on the right-hand axis of figure 5. Consequently, for the highest SiH_4 flows a sticking coefficient is found of $2.5 \times 0.136 = 0.34$. For comparison, the surface reaction probability of SiH_3 is reported to be 0.28 [38] and 0.30 [37]. Probably, for these high SiH_4 flows SiH_3 radicals contribute significantly to the deposition although the contribution of other radicals is not yet fully minimized.

What are the implications of this observation? The refractive index in figure 3d shows a typical value of about 4 for good quality *a*-Si:H at a SiH_4 flow of 40 sccm at a growth rate of 4 nm/s. But when the SiH_4 flow decreases the refractive index also decreases, indicating that the material becomes porous. This also holds for the microcrystalline films. At a SiH_4 flow of 5 sccm (close to the transition to *a*-Si:H) the refractive index is 2.8 (figure 3d). At this SiH_4 flow the average sticking coefficient is 0.6 (figure 5). At the lowest SiH_4 flows the refractive index is 2.7, and the average sticking coefficient is almost 1. This correlation between average sticking coefficient and refractive index strongly suggests that SiH_3 plays a role in the improvement of the

properties of the *a*-Si:H tissue in between the crystalline material. However, keeping both the dilution high (and thus a high H-flux to the substrate to obtain μc-Si:H films) and simultaneously the SiH_3 flux high relative to other silane radicals (and thus improve the quality of the *a*-Si:H fraction in μc-Si:H) is a requirement that is hard to fulfill because SiH_3 and H react which each other.

3.2. Ring position variation

How can we obtain a substantial contribution of SiH_3 radicals to the deposition of the film while having simultaneously a high flux of atomic hydrogen to the substrate? This can be achieved by decreasing the interaction time of the injected SiH_4 with the expanding hydrogen plasma. In this case only one hydrogen abstraction reaction can take place before SiH_3 is deposited at the substrate surface. With ETP CVD, this can be realized by injecting the SiH_4 into the expanding plasma close to the substrate (here we take 55 mm above the substrate). On injection, the SiH_4 molecules will be dragged along with the plasma at a velocity of 100-200 m/s. The atomic hydrogen density is in the range of 10^{19}-10^{20} m^{-3}. It can be estimated based on reaction rates for reactions (1)-(4) reported in literature that only a small fraction of the SiH_3 radicals created in reaction (1) will react with atomic hydrogen (reactions (2)-(4)) to form

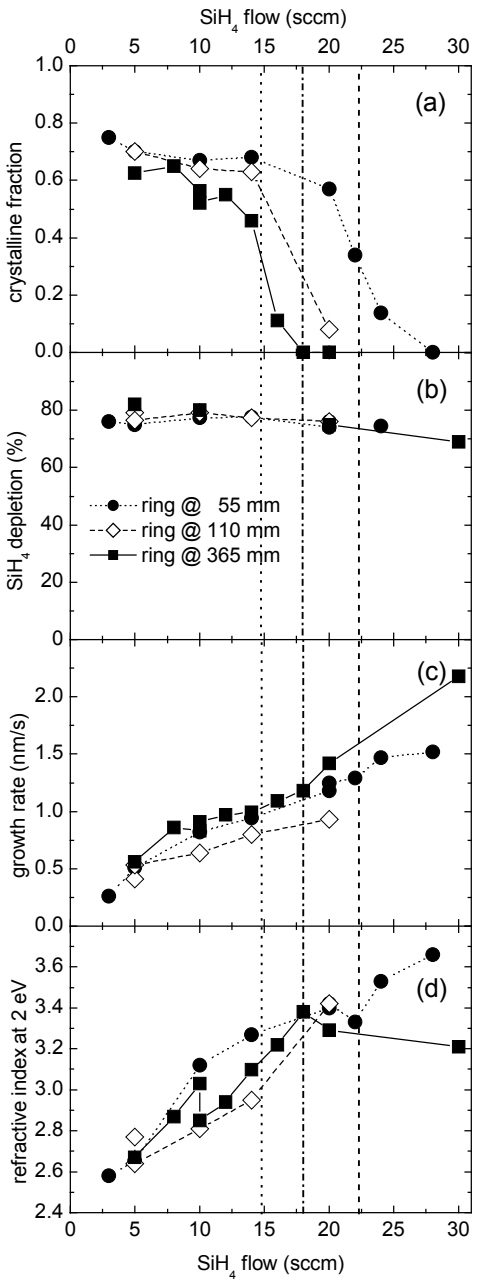

Figure 6. (a) The crystalline fraction, (b) the SiH_4 depletion, (c) the growth rate, and (d) the refractive index at 2 eV as a function of the SiH_4 flow during deposition. The plasma source is fed with 2000 sccm of H_2. Three different injection ring positions are used and in the legend the distance above the substrate is indicated. The vertical dashed lines indicate the transition from microcrystalline to amorphous material (at 30% crystalline fraction), the left-hand one is for the highest and the right-hand one for the lowest injection ring position.

SiH_x with $0 \leq x < 3$ before they reach the substrate surface.

In figure 6 the crystalline fraction, the SiH_4 depletion in the plasma, the growth rate, and the refractive index are shown for varying SiH_4 flow and for different injection ring positions. As can be seen from figure 6a the SiH_4 flow at which the transition from μc-Si:H to a-Si:H occurs shifts to higher SiH_4 flows for lower injection position. This is a first indication that the plasma chemistry is influenced as the injection position is changed, resulting in a different film deposition mechanism. On the other hand the refractive index does not seem to depend much on the SiH_4 flow. However, if we look at the films containing an equal crystalline fraction, for example 50%, then the refractive index increases from 3.1 to 3.4 if the injection position is decreased from 365 mm to 55 mm above the substrate (figure 6d). This implies that lowering of the SiH_4 injection position improves the material properties of the μc-Si:H deposited under these conditions. Similar trends are observed for a hydrogen flow of 1500 sccm and a varying injection ring position. The improvement of the μc-Si:H properties is also reflected in the opto-electronic properties: for the lowest injection ring position a photo-response of 50 at a light conductivity of 10^{-6} S/cm is obtained, whereas for the high injection ring position the photo- and dark conductivity are almost equal at about 10^{-7} S/cm [29].

These observations imply that the composition of the particle flux that arrives at the substrate surface depends on the injection position. To obtain more insight in the nature of the influence of the injection position on the mix of reactive species arriving at the substrate we describe the deposition plasma with a simple plug down model [39, 40]. In this model we apply a number of simplifications for the sake of clarity. Therefore the absolute values that result from the subsequent calculations might not be entirely correct, but the trends will provide a good illustration of the effect of the SiH_4 injection position. We consider a parallel beam of atomic hydrogen having a uniform density of 10^{20} m^{-3} (valid for a hydrogen flow of about 2000 sccm) flowing towards the substrate with a velocity of $v = 200$ m/s. The heavy particle temperature in the plasma beam at substrate level is set at 600 K. These values are obtained from two-photon absorption laser induced fluorescence [41] and electron-beam induced fluorescence [35] measurements and mass spectrometry [42] carried out on comparable plasmas. The gray column between the plasma source and the substrate in figure 7 represents this beam. In reality, the beam expands, resulting in a decreasing atomic hydrogen density going from plasma source to substrate [34]. We approximate the SiH_4 injection (with flow $Q = 5$ sccm) through the eight holes in the injection ring by a homogeneous injection in a plane with an area $A = 64$ cm^2 parallel to the substrate surface, indicated by the white arrow. Since there is no signature of the eight injection holes in the thickness variation of the deposited films, the injection can indeed be assumed to be uniform. This is explained by the fact that the thermal velocity (about 500 m/s) is higher than the drift velocity of the plasma expansion. The vertical position of the injection plane is allowed to vary. We assume that the SiH_4 molecules instantaneously pick up the drift velocity of the plasma towards the substrate. Furthermore we assume that the atomic hydrogen density is higher than the SiH_x density, so we can neglect the atomic hydrogen consumption and keep the density constant. The SiH_4 depletion depends only slightly on the SiH_4 flow (see figure 6b), which justifies this assumption. Furthermore, if the atomic hydrogen density decreases due to reactions with SiH_x, the

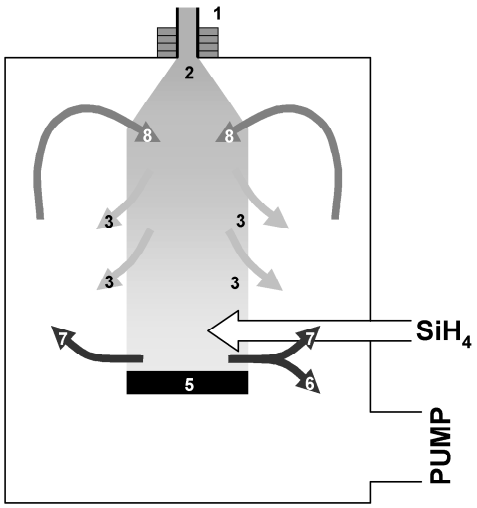

Figure 7. Schematic of the model used for calculations. From the plasma source (1) atomic hydrogen flows to the substrate (5). The SiH_4 is injected (white arrow) homogeneously in a plane (4) and reacts with the atomic hydrogen on the way towards the substrate. Deviations from the simple model are also indicated. The hydrogen plasma expands, therefore atomic hydrogen will also flow to the side of the reactor (3) where it reacts with the SiH_x that did not deposit on the substrate and was not pumped (6), but re-circulates into the reactor (7). The reaction products can enter the plasma expansion (8) and find their way to the substrate again.

reaction rates of reactions (1)-(4) will not change relative to each other and the qualitative results of the model calculations are still valid.

In order to calculate the radical densities SiH_x the following set of differential equations has to be solved:

$$v\frac{\partial n_{\mathrm{SiH}_{x-1}}}{\partial z} = k_x n_{\mathrm{H}} n_{\mathrm{SiH}_x} - k_{x-1} n_{\mathrm{H}} n_{\mathrm{SiH}_{x-1}}, \tag{5}$$

in which n is the density in m^{-3} ($n_{\mathrm{SiH}_x} = 0$ for $x < 0$ and $x > 4$), v the drift velocity, and z the distance from the injection ring towards the substrate. The following boundary condition should be satisfied:

$$n_{\mathrm{SiH}_4}(z=0) = \frac{QN_a}{V_m vA}, \tag{6}$$

in which Q is the SiH_4 mass flow (= 5 sccm), N_a is Avogadro's constant (6.022×10^{23} mol^{-1}), and V_m is the volume per mol (24.5×10^{-3} m^3).

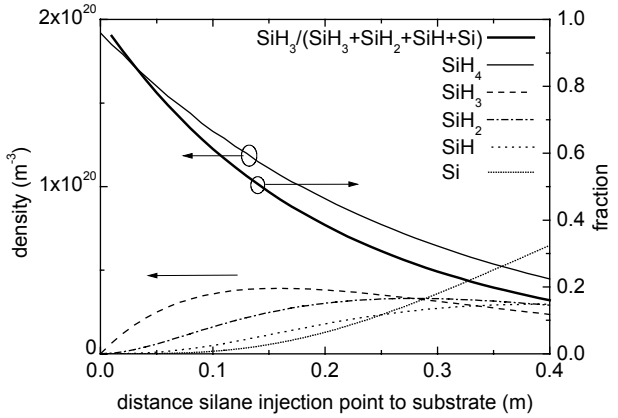

Figure 8. Calculations of the densities of SiH_4 and its related radicals for a hydrogen flow of 2000 sccm. Input: atomic hydrogen density 10^{20} m^{-3}, flow velocity 200 m/s, SiH_4 flow 5 sccm, heavy particle temperature 600 K. The atomic hydrogen density is assumed to be relatively high, so that the consumption of atomic hydrogen does not influence its density. The bold line indicates the SiH_3 radical density relative to the total radical density.

The set of differential equations with all relevant experimental parameters was solved using Maple V software. In figure 8 the results of the calculation of the radical and molecule densities at substrate level as a function of the distance of the injection ring to the substrate is shown. Clearly, the subsequent hydrogen abstraction reactions become more important as the SiH_4 is injected more remote from the substrate. The SiH_4 density at substrate level decreases as the distance from the injection ring increases, the SiH_3 density first increases, until the SiH_4 density is so low that the production rate of SiH_3 in reaction (1) is smaller than the consumption rate in reaction (2), and then decreases. Similar trends are shown for the SiH_2 and SiH densities, and the Si density only increases with the distance between injection ring and substrate because there is no significant loss mechanism in the plasma for the Si radical. Note that we do not consider surface losses. Also shown in figure 8 is the ratio of the SiH_3 radical density to the sum of the densities of the other radicals SiH_x with $0 \leq x < 3$. It is clear that the closer the injection ring to the substrate, the higher the SiH_3 density relative to the density of the other silane radicals becomes.

The model described above is a rather simple and linear model, and here we want to investigate the limitations of the model using the experimental results from figure 6. The proposed model predicts a decrease in the SiH_4 depletion as the injection position becomes lower (cf. SiH_4 density in figure 8), because the interaction time with the atomic hydrogen is shorter. The experimental results, however, show hardly any influence: the depletion is about 80% for all applied injection positions. This immediately reveals the biggest weakness of the model: re-circulation of particles in the reaction chamber is not accounted for. Re-circulating SiH_4 (and even SiH_3 which is reflected at the substrate) will have a relatively long interaction path with H in the background gas, and with the expanding plasma. This re-circulating gas will generate a

SiH_x flux ($x < 3$) at the substrate surface that partly masks the increase in the SiH_3 flux due the lowering of the injection position. Therefore the growth rate and the depletion are not significantly influenced by the injection position. Probably, a process chamber in which re-circulation plays a smaller role (e.g., larger diameter of the reaction chamber or metal plates that block re-circulating gas flows) can emphasize the influence of the injection position on the material properties and might even be the most promising way to further improve the quality of ETP CVD deposited μc-Si:H.

4. Conclusions

Two observations have been described in this paper. Firstly, investigation of the growth rate as a function of SiH_4 flow around the transition region between amorphous and microcrystalline material reveals that the average sticking coefficient of the depositing radicals decreases and the refractive index increases with increasing SiH_4 flow. Secondly, the material properties of μc-Si:H improve when SiH_4 is injected closer to the substrate, which can only be explained by a change in radical composition at the substrate. A model that we applied to describe the deposition plasma indicates that there is a relative increase in the SiH_3 radical flux when the injection position is closer to the substrate. These two observations strongly suggest that an increase in the contribution of SiH_3 to the growth of μc-Si:H improves the material quality.

Acknowledgements

Ries van de Sande and Jo Jansen are acknowledged for the design and the construction of the deposition system and for their technical assistance. Martijn Tijssen and Arjan Driessen are acknowledged for their skilful technical assistance. This research was financially supported by NOVEM.

References

[1] H.F. Sterling and R.C.G. Swann, Solid State Electron. **8**, 653 (1965).

[2] A. Matsuda, K. Nomoto, Y. Takeuchi, A. Suzuki, A. Yuuki, and J. Perrin, Surf. Sci. **22**, 50 (1990).

[3] J. Robertson, J. Appl. Phys. **87**, 2608 (2000).

[4] W.M.M. Kessels, M.G.H. Boogaarts, J.P.M. Hoefnagels, M.C.M. van de Sanden, and D.C. Schram, J. Vac. Sci. Technol. **A 19**, 1027 (2001).

[5] M.C.M. van de Sanden, R.J. Severens, W.M.M. Kessels, R.F.G. Meulenbroeks, and D.C. Schram, J. Appl. Phys **84**, 2426 (1998).

[6] W.M.M. Kessels, A.H.M. Smets, D.C. Marra, E.S. Aydil, D.C. Schram, and M.C.M. van de Sanden, Thin Solid Films **383**, 154 (2001).

[7] N. Itabashi, N. Nishiwaki, M. Magane, S. Naito, T. Goto, A. Matsuda, C. Yamada, and E. Hirota, Jpn. J. Appl. Phys. **29**, 585 (1993).

[8] A. Gallagher, Mater. Res. Soc. Symp. Proc. **70**, 3 (1986).

[9] A. Matsuda, J. Vac. Sci. Technol. **A. 16**, 365 (1998).

[10] W.M.M. Kessels, M.C.M. van de Sanden, R.J. Severens, and D.C. Schram, J. Appl. Phys. 87 (7), **3313** (2000).

[11] A. Matsuda, Thin Solid Films **337**, 1 (1999).

[12] J. Robertson, J. Appl. Phys. **93**, 731 (2003).

[13] K. Nakamura, K. Yoshino, S. Takeoka, and I. Shimizu, Jpn. J. Appl. Phys. **34**, 442 (1995).

[14] U. Graf, J. Meier, U. Kroll, J. Bailat, C. Droz, E. Vaillat-Sauvain, and A. Shah, Thin Solid Films **427**, 37 (2003).

[15] R.E.I. Schropp, Thin Solid Films **403-404**, 17 (2002).

[16] D.H. Levi, B.P. Nelson, J.D. Perkins, and H.R. Moutinho, J. Vac. Sci. Technol. **A 21**, 1545 (2003).

[17] M. Pontoh, V.L. Dalal, and H. Gandhi, Mater. Res. Soc. Symp. Proc. **71**, 521 (2002).

[18] C. Smit, E.A.G. Hamers, B.A. Korevaar, R.A.C.M.M. van Swaaij, and M.C.M. van de Sanden, J. Non-Cryst. Solids **299-302**, 98 (2002).

[19] J. Benedikt, R.V. Woen, S.L.M. van Mensfoort, V. Perina, J. Hong, and M.C.M. van de Sanden, Diamond and related materials **12**, 90 (2003).

[20] M. Creatore, M. Kilic, K. O'Brien, R. Groenen, and M.C.M. van de Sanden, Thin Solid Films **427**, 137 (2003).

[21] W. Luft and Y. Simon Tsuo, Hydrogenated amorphous silicon alloy deposition processes, Marcel Dekker Inc., 270 Madison Avenue, New York (1993).

[22] A. Goumri, W.-J. Yuan, L. Ding, Y. Shi, and P. Marshall, Chem. Phys. **177**, 233 (1993).

[23] J. Perrin, O. Leroy, and M.C. Bordage, Contrib. Plasma Phys. **36**, 1 (1996).

[24] M.J. de Graaf, R. Severens, R.P. Dahiya, M.C.M. van de Sanden, and D.C. Schram, Phys. Rev. **E 48**, 2098 (1993).

[25] W.M.M. Kessels, A. Leroux, M.G.H. Boogaarts, J.P.M. Hoefnagels, M.C.M. van de Sanden, and D.C. Schram, J. Vac. Sci. Technol. **A 19**, 467 (2001).

[26] H. Fujiwara, Y. Toyoshima, M. Kondo, and A. Matsuda, Mater. Res. Soc. Symp. Proc. **609**, A2.1.1 (2000).

[27] I. Solomon, B. Drevillon, H. Shirai, and N. Layadi, J. Non-Cryst. Solids **164**, 989 (1993).

[28] E.A.G. Hamers, A.H.M. Smets, C. Smit, J.P.M. Hoefnagels, W.M.M. Kessels, and M.C.M. van de Sanden, Mater. Res. Soc. Symp. Proc. **664**, A4.2.1 (2001).

[29] C. Smit, A. Klaver, B.A. Korevaar, A.M.H.N. Petit, R.A.C.M.M. van Swaaij, and M.C.M. van de Sanden, submitted for publication to Thin Solid Films.

[30] B.A. Korevaar, C. Smit, R.A.C.M.M. van Swaaij, A.H.M. Smets, W.M.M. Kessels, J. W. Metselaar, D. C. Schram, and M. C. M. van de Sanden, Proc. of 16th European Photovoltaic Solar Energy Conference, 2000, B119.

[31] W.M.M. Kessels, R.J. Severens, A.H.M. Smets, B.A. Korevaar, G.J. Adriaenssens, D.C. Schram, and M.C.M. van de Sanden, J. Appl. Phys. **89**, 2404 (2001).

[32] C. Smit, R.A.C.M.M. van Swaaij, H. Donker, A.M.H.N. Petit, W.M.M. Kessels, and M.C.M. van de Sanden, J. Appl. Phys. **94**, 3582 (2003).

[33] R.E.I. Schropp and M. Zeman, Amorphous and microcrystalline silicon solar cells (1998, Kluwer academic publishers, Dordrecht, the Netherlands).

[34] S. Mazouffre, M.G.H. Boogaards, J.A.M. van der Mullen, and D.C. Schram, Phys. Rev. Lett. **84**, 2622 (2000).

[35] C. Smit, G.J.H. Brussaard, E.C.M. de Beer, D.C. Schram, and M.C.M. van de Sanden, Plasma Sources Sci. Technol. **13**, 1 (2004).

[36] Z. Remeš, M. Vaněček, P. Torres, U. Kroll, A.H. Mahan, and R.S. Crandall, J. Non. Cryst. Solids **227-230**, 876 (1998).

[37] J.P. Hoefnagels, A.A.E. Stevens, M.H.G. Boogaarts, W.M.M. Kessels, and M.C.M. van de Sanden, Chem. Phys. Lett. **360**, 189 (2002).

[38] J. Perrin, M. Shiratani, P. Kae-Nune, H. Videlot, J. Jolly, and J. Guillon, J. Vac. Sci. Technol. A **16**, 278 (1998).

[39] G.M.W. Kroesen, D.C. Schram, and J.C.M. de Haas, Plasma Chem. Plasma Proc. **10**, 531 (1990).

[40] M.C.M. van de Sanden, R. Van den Bercken, and D.C. Schram, Plasma Sources Sci. Technol. **3**, 511 (1994).

[41] S. Mazouffre, M.G.H. Boogaarts, I.S.J. Bakker, P. Vankan, R. Engeln, and D.C. Schram, Phys. Rev. E **64**, 016411 (2001).

[42] W.M.M. Kessels, Ph. D. thesis, Eindhoven University of Technology (2000).

Summary

The aim of the research described in this thesis is to investigate the potential of expanding thermal plasma enhanced chemical vapour deposition (ETP CVD) for high-rate deposition of hydrogenated microcrystalline silicon (μc-Si:H) films for application in solar cells. Microcrystalline silicon films find their application in large-area electronic devices such as solar cells and active matrix flat panel displays. By decreasing the production time of the microcrystalline films the production costs of these devices can be reduced. Therefore the deposition rate should be increased. Encouraged by previously obtained results on the preparation of, for example, hydrogenated amorphous silicon films, amorphous carbon films, and silicon nitride films at elevated growth rates with ETP CVD, this technique has been applied for the deposition of hydrogenated microcrystalline silicon films in this work. The research is carried out in a joint program of the Eindhoven and Delft Universities of Technology. The majority of the work has been carried out on the CASCADE, which is a laboratory set-up for the preparation of thin-film silicon solar cells using and expanding thermal plasma.

Like other chemical vapour deposition techniques for the deposition of silicon films, in ETP CVD the μc-Si:H film is deposited using the precursor gas silane. In the reactor these molecules are dissociated into radicals by interaction with atomic hydrogen, which emanate from a cascaded arc plasma source into the reactor. Note the difference with, e.g., radio frequent plasma enhanced chemical vapour deposition, in which the precursor gas is dissociated by electron impact. The radicals are responsible for the film growth.

During this research electron beam induced fluorescence has been applied and improved in order to measure the atomic hydrogen content in the plasma, which is an important species in the deposition process. This technique is relatively easy to apply compared to laser induced fluorescence techniques, and needs no calibration. Furthermore, to determine the crystalline fraction in the silicon films Raman spectroscopy has been used frequently. Methods to interpret these Raman spectra and to extract the crystalline fraction have been reviewed and turned out to suffer from a number of inaccuracies. An alternative method has been developed, in which a scaled Raman spectrum of an amorphous silicon film is subtracted from μc-Si:H spectrum. The result is an unambiguous determination of the crystalline mass fraction in μc-Si:H films.

In the search for good quality microcrystalline silicon films, process parameters like gas flows, reactor pressure, substrate temperature, are varied. The best material properties have been achieved when using only hydrogen gas in the plasma source instead of an argon-hydrogen mixture. Furthermore, it is found that the silane-to-hydrogen gas flow ratio should be taken close to the so-called “transition regime” where the films start to become amorphous. This is also reported for other deposition techniques. Finally, the position at which the precursor gas is injected into the plasma

source is found to be of large influence on the material quality: closer to the substrate gives better material properties. These effects are ascribed to an enhanced contribution of the silyl radical to the growth of the film.

The properties of the microcrystalline films in terms of crystalline fraction (60%-80%), dark conductivity (10^{-8} S/cm), photoconductivity (10^{-6} S/cm), and refractive index (3.5 at 2 eV) are comparable to other deposition techniques, even at growth rates of about 1.2 nm/s. The material shows a columnar structure and is slightly porous. The best μc-Si:H films have been incorporated in solar cells. However, therefore good, thin, doped μc-Si:H films had to be developed in our laboratory. The challenge of this development is to bring down the thickness of the amorphous incubation layer, which is related to the initiation of the growth of μc-Si:H films. In this part of the work it is shown that for a minimum incubation layer thickness the process pressure and the electrode distance should be well matched, and it is indicated how this can be achieved. The highest conversion efficiencies with p-i-n deposited solar cells that have been obtained are 1.9% when the intrinsic microcrystalline layer is grown at 0.2 nm/s and 1.5% for a rate of 1.2 nm/s. These results show that there is room for improvement, especially in the density of the films, in the crystalline fraction, and in the thickness of the intrinsic films as well as in the doped films. Nevertheless, the results on the film quality and the growth rates indicate that expanding thermal plasma enhanced chemical vapour deposition is a suitable technique for the deposition of microcrystalline silicon and could turn out to be an attractive technology for high-rate deposition of microcrystalline silicon in large area electronics.

Samenvatting

Het onderzoek dat in dit proefschrift beschreven wordt, heeft ten doel de mogelijkheden te verkennen van het expanderende thermisch plasma (ETP) voor de plasma gestimuleerde chemische damp depositie (PECVD) met hoge groeisnelheid van waterstofhoudend microkristallijn silicium (μc-Si:H) voor toepassing in zonnecellen. Daar waar grote oppervlakken met elektronica bedekt worden, zoals zonnecellen en actieve-matrix platte beeldschermen, vinden dunne lagen van μc-Si:H hun toepassing. De kostprijs van deze producten kan omlaag als ze sneller geproduceerd kunnen worden. Om dat te bereiken moet de groeisnelheid van de dunne lagen omhoog. Met expanderend thermisch plasma gestimuleerde chemische damp depositie (ETP CVD) zijn eerder al bemoedigende resultaten gehaald bij de vervaardiging van, bijvoorbeeld, waterstofhoudend amorf silicium, amorf koolstof en silicium nitride, en hierbij zijn hoge groeisnelheden gehaald. In dit onderzoek is de techniek ETP CVD gebruikt om dunne lagen van μc-Si:H te maken. Het onderzoek is uitgevoerd in een samenwerkingsproject van de technische universiteiten van Eindhoven en Delft en het merendeel is uitgevoerd met de CASCADE, een laboratoriumopstelling voor de vervaardiging van zonnecellen van dunne silicium lagen met behulp van een expanderend thermisch plasma.

Net als bij andere plasma depositietechnieken voor dunne silicium films, wordt bij ETP CVD silaangas als precursorgas gebruikt. Uit de cascadeboog plasmabron komt onder andere atomair waterstof. De silaanmoleculen worden in de reactor door interactie met dit atomaire waterstof afgebroken, waarbij radicalen ontstaan. Dit wijkt duidelijk af van bijvoorbeeld radio frequent PECVD, waarbij de afbraak van het silaangas door botsingen met elektronen wordt gerealiseerd. De radicalen zijn verantwoordelijk voor de materiaalaangroei.

Teneinde het aantal waterstofatomen, welke een belangrijke rol vervullen in het depositieproces, in het plasma te bepalen, is in dit onderzoek elektronenbundel geïnduceerde fluorescentie toegepast en verbeterd. Deze techniek is relatief eenvoudig toe te passen vergeleken met laser geïnduceerde fluorescentietechnieken, en behoeft bovendien geen calibratie. Voor de bepaling van de kristallijne fractie in de silicium films wordt veelvuldig Raman spectroscopie gebruikt. In dit proefschrift worden verschillende interpretaties van deze spectra beschouwd, alsook methoden om de kristallijne fractie eruit te destilleren. Al deze bestaande methoden bleken een aantal onnauwkeurigheden te bevatten. Een alternatieve methode is ontwikkeld waarbij een geschaald Raman spectrum van amorf silicium afgetrokken wordt van het spectrum van microkristallijn silicium. Het resultaat is een eenduidige bepaling van de kristallijne massafractie in lagen van μc-Si:H.

Op jacht naar lagen van μc-Si:H van hoge kwaliteit zijn de procesinstellingen gevarieerd, zoals gashoeveelheden, reactordruk en substraattemperatuur. Het beste materiaal wordt verkregen wanneer alleen waterstof wordt toegevoerd in de plasmabron, en geen argon-waterstof mengsel. Bovendien moet de verhouding van de

hoeveelheid gebruikte silaan en waterstofgas dichtbij het zogenaamde "overgangsgebied" liggen waar het gedeponeerde materiaal amorf wordt. Deze trend is ook voor andere plasma depositietechnieken waargenomen. Tenslotte heeft de positie waarop het silaangas in de plasmabundel wordt geïnjecteerd een grote invloed op de materiaalkwaliteit: is de injectie dichter bij het substraat, dan is de materiaalkwaliteit hoger. Deze effecten zijn in verband gebracht met een verhoogde bijdrage van het SiH_3 radicaal tot de materiaalaangroei.

De eigenschappen van de μc-Si:H lagen, zoals de kristallijne fractie (60%-80%), de donkergeleiding (10^{-8} S/cm), de fotogeleiding (10^{-6} S/cm bij AM 1.5 belichting) en de brekingsindex (3.5 bij 2 eV) zijn vergelijkbaar met andere depositietechnieken, ook bij groeisnelheden van 1.2 nm/s. Het materiaal heeft een kolomstructuur en is enigszins poreus. Het beste materiaal dat verkregen is, is ingebouwd in zonnecellen. Daarvoor moesten echter eerst goede dunne gedoteerde μc-Si:H lagen ontwikkeld worden in ons laboratorium. De uitdaging is daarbij om de amorfe incubatielaag, waarmee de groei van μc-Si:H start, zo dun mogelijk te maken. In dit gedeelte van het werk wordt aangetoond dat het hierbij van belang is dat de procesdruk en de elektrodeafstand goed op elkaar zijn afgestemd. Ook wordt aangegeven hoe men dit kan doen. Het hoogste energieomzettingsrendement voor p-i-n gegroeide zonnecellen die in dit werk gehaald is, bedraagt 1.9% bij een groeisnelheid van de intrinsieke laag van 0.2 nm/s en 1.5% bij een groeisnelheid van 1.2 nm/s. Deze resultaten laten zien dat er nog een en ander geoptimaliseerd moet worden, met name de materiaaldichtheid, de kristallijne fractie en de dikte van zowel de intrinsieke laag als van de gedoteerde lagen. Maar de behaalde filmkwaliteit en groeisnelheid tonen aan dat ETP CVD een geschikte techniek is voor de depositie van μc-Si:H en in potentie een aantrekkelijke technologie is om elektronica met μc-Si:H met grote productiesnelheid op grote oppervlakken te realiseren.

List of Publications related to this work

High-rate Deposition of Microcrystalline Silicon with an Expanding Thermal Plasma
C. Smit, A. Klaver, B.A. Korevaar, A.M.H.N. Petit, D.L. Williamson, R.A.C.M.M. van Swaaij, and M.C.M. van de Sanden, submitted for publication to Thin Solid Films.

The role of the sylil radical in plasma deposition of microcrystalline silicon
C. Smit, R.A.C.M.M. van Swaaij, E.A.G. Hamers, and M.C.M. van de Sanden, J. Appl. Phys. **96**, 4079 (2004).

Electron beam induced fluorescence measurements of the degree of hydrogen dissociation in hydrogen plasmas
C. Smit, G.J.H. Brussaard, E.C.M. de Beer, D.C. Schram, and M.C.M. van de Sanden, Plasma Sources Sci. Technol. **13**, 1 (2004).

Material structure of microcrystalline silicon deposited by an expanding thermal plasma
C. Smit, D.L. Williamson, M.C.M. van de Sanden, and R.A.C.M.M. van Swaaij, Mater. Res. Soc. Symp. Proc. **762**, 527 (2003).

Determining the material structure of microcrystalline silicon from Raman spectra
C. Smit, R.A.C.M.M. van Swaaij, H. Donker, A.M.H.N. Petit, W.M.M. Kessels, and M.C.M. van de Sanden, J. Appl. Phys. **94**, 3582 (2003).

High-rate microcrystalline silicon for solar cells
C. Smit, B.A. Korevaar, A.M.H.N. Petit, R.A.C.M.M. van Swaaij, W.M.M. Kessels, and M.C.M. van de Sanden, Proc. of the 29th IEEE Photovoltaic Specialists Conference, 2002, p. 1170.

Fast deposition of microcrystalline silicon with an expanding thermal plasma
C. Smit, E.A.G. Hamers, B.A. Korevaar, R.A.C.M.M. van Swaaij, and M.C.M. van de Sanden, J. Non-Cryst. Solids **299-302**, part 1, 98 (2002).

Effect of buffer layers on p-i-n a-Si:H solar cells deposited at high rate utilising an expanding thermal plasma.
B.A. Korevaar, A.M.H.N. Petit, C. Smit, R.A.C.M.M. van Swaaij, and M.C.M. van de Sanden, Proc. of the 29th IEEE Photovoltaic Specialists Conference, 2002, p. 1230.

Integration of expanding thermal plasma deposited hydrogenated amorphous silicon in solar cells
B.A. Korevaar, C. Smit, A.M.H.N Petit, R.A.C.M.M. van Swaaij, M.C.M. van de Sanden, Mater. Res. Soc. Proc. **715**, 595 (2002).

Material properties and growth process of microcrystalline silicon with growth rates in excess of 1 nm/s
E.A.G. Hamers, A.H.M. Smets, C. Smit, J.P.M. Hoefnagels, W.M.M. Kessels, and M.C.M. van de Sanden, Mat. Res. Soc. Proc. **664**, A4.2.1 (2001).

Importance of defect density near the p-i interface for a-Si:H solar cell performance
B.A. Korevaar, C. Smit, R.A.C.M.M. van Swaaij, D.C. Schram, and M.C.M. van de Sanden, Mater. Res. Soc. Symp. Proc. **664**, A24.4 (2001).

Challenges in amorphous silicon solar cell technology
R.A.C.M.M. van Swaaij, M. Zeman, B.A. Korevaar, C. Smit, J.W. Metselaar, and M.C.M. van de Sanden, Acta Physica Slovaca **50**, no. 5, 559-570 (2000).

Temperature dependence at various intrinsic a-Si:H growth rates of p-i-n deposited solar cells
B.A. Korevaar, C. Smit, A.H.M. Smets, R.A.C.M.M. van Swaaij, D.C. Schram, and M.C.M. van de Sanden, Proc. of the 28th IEEE Photovoltaic Specialists Conference, 2000, p. 916.

Solar cells with intrinsic a-Si:H deposited at rates larger than 5 Å/s by the expanding thermal plasma
B.A. Korevaar, C. Smit, R.A.C.M.M. van Swaaij, A.H.M. Smets, W.M.M. Kessels, J.W. Metselaar, D.C. Schram, and M.C.M. van de Sanden, Proc. of the 16th European Photovoltaic Solar Energy Conference, 2000, B119.

Dankwoord

Het onderzoek dat ten grondslag ligt aan dit proefschrift had nooit uitgevoerd kunnen worden zonder de hulp van vele mensen. Op deze plaats wil ik graag iedereen bedanken die direct of indirect heeft bijgedragen tot dit werk.

Ten eerste wil ik Richard van de Sanden en Daan Schram bedanken voor hun vertrouwen en de mogelijkheid om in hun groep te komen werken. Vrij snel na mijn komst in hun groep opperden ze al de mogelijkheid om te promoveren, als een soort van “tweede kans”. Daar wilde ik vrij lang niets van weten, maar . . . uiteindelijk is het er toch van gekomen. Richard, jou wil ik met name bedanken voor je begeleiding. Ik keek altijd erg uit naar mijn bezoeken aan jou in Eindhoven. Onze discussies waren altijd lekker fel, en jou enthousiasme was elke keer weer erg aanstekelijk. Als ik dan uit Eindhoven vertrok was weer helemaal duidelijk wat er moest gebeuren en jeukte mijn handen om verder te gaan. In Delft was daar René van Swaaij, mijn directe begeleider. Met hem heb ik vele nuttige discussies gehad en de goede samenwerking met hem heb ik zeer op prijs gesteld. Ook was hij nooit te beroerd om een tekst nóg een keer kritisch door te lezen.

Heel belangrijk voor het plezier in je werk zijn de collega’s waar je direct mee samenwerkt. Bas en Agnès: jullie waren heel prettige collega’s. De samenwerking op één machine ging heel soepel en we konden ook wel eens over iets anders dan het werk praten. In Eindhoven heb ik de kunst van het deponeren met de boog geleerd van de Master himself. Bedankt, meneer Smets! Daarnaast ben ik veel dank verschuldigd aan Arjen Klaver voor de vele experimenten en deposities die hij voor mij heeft uitgevoerd en uitgewerkt en die een belangrijk deel van hoofdstuk 6 vormen. Verder waren ook Erwin Kessels, Arno Smets, Edward Hamers, Miro Zeman, Martin Kroon, Barry van Dijk en Paul van der Wilt regelmatig te porren voor een discussie of het beantwoorden van een vraag.

Omdat het onderzoek een samenwerkingsverband betrof tussen de groep ETP van de TU Eindhoven en de groep ECTM (DIMES) van de TU Delft heb ik vele prettige collega’s gekend. Het begon in Eindhoven waar ik relatief kort gezeten heb, maar me snel thuis voelde door de hele prettige en coöperatieve sfeer die er hing. Bedankt Ariël, Karine, Iain, Peter, Jean-Pierre, Stephane, Richard, Adriana, Maarten, Maikel en alle andere vakgroepgenoten. Daarna volgde een verhuizing samen met Bas naar Delft. Dat we daar meteen konden delen in de cafeïne infrastructruur van Barry en Martin zorgde voor een prettige start. Heren, bedankt voor die gezelligheid! Ook de verdere collega’s bij ECTM wil ik bedanken voor de goede sfeer: Leon, Paul, Wibo, Ad, Marcel, Artyom, Hoa, Joost, Amir, en alle andere collega’s aldaar.

Furthermore I want to thank Vikram Dalal for the useful discussions we had during his visits to Eindhoven and Delft. Thanks to the members of the “kerncommissie” (2de promotor Kees Beenakker, Vikram Dalal, Prof. Dr. J. Robertson) for the proofreading of the manuscript and the useful comments.

Experimenteel onderzoek staat of valt met goede technici. De geestelijk vader van de hier gebruikte laboratorium opstelling is Ries van de Sande. Zijn gedegen en nauwgezette ontwerp heeft een machine opgeleverd die niet vaak “plat lag”, makkelijk te bedienen was en inmiddels meer dan 1400 samples heeft geproduceerd. Bovendien heb ik samen met hem en Jo Jansen een behoorlijk aantal leuke en leerzame uurtjes besteed aan de assemblage van sommige van de onderdelen. Maar er zijn meer mensen onmisbaar geweest voor het succes van de laboratorium opstelling. De mensen van de centrale werkplaats van de TU Eindhoven die de machine gebouwd hebben, met name Peer Brinkgreve, Toon Gevers, Jan Ketelaars, Jovita Moerel, en vele anderen. Herbert Fiedler was altijd bereid om ook nog “remote” snelle PLC hulp te verlenen in Delft. Na de verhuizing naar DIMES te TU Delft was er ook de nodige hulp op het technische vlak. De installatie van de machine was in de kundige handen van Jos Custers en Alfred Apon. Daarna hebben Ben Girwar en Martijn Tijssen aardig wat uurtjes helpen sleutelen. Verder dank voor de ondersteuning bij de sample analyse door Erik Jan Geluk en Arjan Driessen. Er waren vele mensen bij DIMES die ervoor zorgden dat een en ander technisch goed bleef draaien: Gilles Goubréau en Alfred voor de snelle klusjes, Jan Warmerdam voor de gassen, Bert de Groot voor de SEM plaatjes, Tom Scholtes, Wim van der Vlist, en vele anderen. Ook dank aan de secretariële ondersteuning in Eindhoven en Delft voor de snelle klusjes tussendoor.

Verder wil nog een aantal mensen bedanken die een bijdrage geleverd hebben aan de analyse van de samples: Harry Donker voor Raman spectroscopie, Prof. Dr. D.L. Williamson voor SAXS/XRD/flotation density metingen, Frans Tichelaar voor het elektronenmicroscopie werk, Niek van de Pers voor XRD metingen, en de vakgroep R&CE van de faculteit Scheikundige Technologie van de Technische Universiteit Delft voor het gebruik van hun Raman microscoop waar ik altijd terecht kon. Mark de Graaf wil ik nog bedanken voor de hulp met het schrijven van het introductiehoofdstuk toen ik er even niet zo’n zin meer in had.

Als belangrijkste is er nog het thuisfront. Een promotieonderzoek trekt alle aandacht naar zich toe en combineert daardoor zeer slecht met een gezinsleven. Norma, mijn welgemeende excuses voor het feit dat jij en ons gezin erg onderbedeeld zijn geweest in de afgelopen periode. Ik weet dat je dit vaak niet leuk vond, maar ik weet zeker dat de toekomst zal uitwijzen dat je deze offers niet voor niets gelaten hebt.

Curriculum vitae

Chiel Smit was born in Vlissingen, the Netherlands, on March 10, 1967. He obtained his VWO diploma in 1985 from the Stedelijk Gymnasium in 's-Hertogenbosch. In that year he started studying applied physics at the Department of Applied Physics of the Eindhoven University of Technology, from which he graduated in 1992. His master thesis work was carried out in the semiconductor physics group.

From January 1993 until March 1994 he worked as a researcher on the photography of corona and streamer discharges at the High-Voltage Engineering group of the Department of Electrical Engineering at the Eindhoven University of Technology. Then he switched to the Charged Particle Optics group of the Department of Applied Physics of the Delft University of Technology where he spent five years on the development of surface analysis techniques with high spatial resolution in a transmission electron microscope.

In May 1999 he joined the group Equilibrium and Transport in Plasmas of the Department of Applied Physics at the Eindhoven University of Technology were he worked in a joint project in the group Electronic Components, Technology, and Materials of the Delft Institute of Microelectronics and Submicron technology (DIMES) at the Delft University of Technology. At first, he was involved in the application of expanding thermal plasma enhanced chemical vapour deposition as a novel deposition technology for amorphous silicon solar cells. Later, he concentrated on the deposition of microcrystalline silicon with the same technology for application in solar cells. The results of this research are reflected in this thesis.

In July 2003 he joined OTB Engineering were he was involved in the development of industrial PVD and CVD equipment. Since August 2004, he works at Philips Medical Systems, BiometriX, on the development of amorphous silicon based X-ray imaging arrays.